Body-Coupled Communications

Experimental characterization, channel modeling and physical layer design

Master Thesis

Nafiseh Seyed Mazloum

REF. NO. EX084/2008

Chalmers University of Technology
Department of Signals and Systems

Philips Research
Distributed Sensor Systems

December 2008

Contents

Abstract

Body-coupled communications (BCC), which uses the human body as transmission medium for electrical data signals, is considered as a key enabling technology for wireless body-area networks (WBANs). To successfully deploy these BCC-based WBANs in a wide range of consumer lifestyle and healthcare applications, it is crucial to have a good understanding of the rarely studied body channel behavior. Moreover, such a BCC solution should be based on a physical layer design, which is well suited for this channel.

To this end, this thesis first investigates the characteristics and fundamental properties of the capacitive-coupled on-body channel experienced in BCC operation. The study is based on experimental results obtained with a specifically designed measurement system. Results from extensive measurements reveal the influence of coupler design, coupler position and body movement on the signal propagation loss. Also, these provide insight into the experienced interference from other radio frequency (RF) systems and electrical equipment.

The results of the experimental study showed that by increasing the distance between the couplers on the body, the propagation loss increases. It was also shown that the maximum propagation loss for the entire body channel is below 80 dB and that the channel exhibits a high-pass frequency response. Moreover, the frequency dispersion of the BCC channel was shown to be much smaller than for RF-based WBANs. Regarding the node factor form, the results showed that increasing the coupler size reduced the propagation loss. Therefore, there is a tradeoff between the coupler size and the propagation loss. Additionally, the experimental results showed that the propagation loss variation due to the body movement is very limited and the maximum obtained standard deviation was less than 3 dB. It was also concluded from the results that BCC can be susceptible to interference from other electronic equipment, the characteristics of which largely depend on the location of the BCC.

Moreover, the experimental results are used to develop models for the BCC channel. These models improve our understanding of the on-body channel behavior. Also, they can be used for system simulation to analyze the performance of the BCC system. The first model describes the mean propagation loss as a function of frequency, the parameters of which depend on the node size and node position. The other model describes the propagation loss variation due to body movement which is shown to be well modeled by a log-normal distribution.

Finally, based on the observed BCC channel behavior, a novel BCC physical layer design is proposed. We name it adaptive code-spreading and it is based on varying the spreading code after sensing the channel and interference. The performance of this design is evaluated using Monte Carlo simulations. Walsh-Hadamard sequences are proposed to be used as spreading code. The influence of different spreading code spectral shapes and lengths was investigated. The numerical results showed that selecting the suitable codeword improves the performance of the system significantly. It was also shown that considering different code length, a longer code yields a better performance but at a cost of a lower data-rate. The simulations verify that employing this solution results in a performance gain when the communication system experiences non-white noise and interference. [1]

[1] Part of this work has been previously published in [1].

Abbreviations

A

ADC	Analog-to-Digital Convertor
AFH	Adaptive Frequency Hopping

B

BAN	Body-Area Network
BCC	Body-Coupled Communications
BER	Bit Error Rate
bps	bit per second
BPSK	Binary Phase Shift Keying

C

CDF	Cumulative Distribution Function
CSMA-CA	Carrier Sense Multiple Access-Collision Avoidance

D

DCI	Direct-Coupled Interface
DDS	Digital Direct Synthesizer
DS-SS	Direct Sequence-Spread Spectrum

E

ECDF	Empirical Cumulative Distribution Function
ECG	Electrocardiogram
EEG	Electroencephalography
EVM	Error Vector Magnitude

F

FDTD	Finite-Difference Time-Domain
FSK	Frequency Shift Keying

G

GHz	Giga Hertz

I

IBC	Intra-Body Communications

K

kbps	kilo bit per second
kHz	kilo Hertz

M

MAC	Media Access Control
Mbps	Mega bit per second
MF	Matched Filter
MHz	Mega Hertz
Msps	Mega symbol per second

N

NFC	Near Field Communication

O

OFDM	Orthogonal Frequency Division Multiplexing
OOK	On-Off Keying
OSI	Open Systems Interconnection

P

PC	Personal Computer
PCB	Printed Circuit Board
PDA	Personal Digital Assistant
PHY	Physical Layer
P-P	Probability-Probability
PSD	Power Spectral Density
PVC	Polyvinyl Chloride

R

RF	Radio Frequency
RFID	Radio Frequency Identification
RX	Receiver

S

SIR	Signal-to-Interference Ratio
SNIR	Signal-to-Noise and Interference Ratio
SPDIF	Sony/Philips Digital Interface Format

T

TCP/IP	Transmission Control Protocol/Internet Protocol
TX	Transmitter

U

UHF	Ultra High Frequency

W

WBAN	Wireless Body-Area Network

WH	Walsh-Hadamard
WiFi	Wireless Fidelity
WLS	Weighted Least Squares

Chapter 1

Introduction

1.1 Background

Portable electronic consumer devices like MP3 players, mobile phones, watches, PDAs and headsets have received an increased interest over the last years. These devices more and more need to interact with each other or with other devices like e.g. desktop computers. To avoid a clutter of wires, it will be required to set up a wireless radio frequency (RF) communication link between two or more devices, for instance using Bluetooth, ZigBee or WiFi. This typically can be a very lengthy and inconvenient procedure, as it often requires manual user invention.

Consequently, there is an increasing need to efficiently connect the electronic equipments surrounding a person's body into what we refer as a wireless body-area network (WBAN) and, subsequently, avoid the troublesome handling of individual output devices for each system. A possible application of these BANs in this area is that a head set can be wirelessly connected to both a media player and a mobile phone. Protection of the personal devices is another reason to form a WBAN. The fact that people wear more expensive mobile electronic devices increases the need for a BAN, where portable devices check the presence of each other in order to instantaneously detect the theft of one of them.

Next to these consumer lifestyle applications, WBANs are also a key enabling technology for medical patient monitoring. In the healthcare industry, medical monitoring and electronic medical records provide clinicians with advanced access to relevant patient information. Sensors on the human body measure the vital signs, e.g. the electrocardiogram (ECG), electroencephalography (EEG), body temperature, blood temperature or blood oxygen saturation and send this information to the medical monitors. So far, most of these sensors are connected by wires to the medical monitor(s) as illustrated in Fig. 1.1. To reduce the complexity of this system and to fulfill the demand for more convenient patient monitoring, there is a need to replace the data cables between the sensors and the monitor by wireless links. Such wireless medical body sensors also provide clinicians the opportunity to obtain information for more monitoring applications, e.g. during surgery, during patient's movement and home monitoring of chronically ill patients. The wireless body-worn medical sensors of each patient together with monitor basically form a WBAN [2].

In both application areas, i.e. healthcare and consumer lifestyle, the different nodes placed on and near the human body need to communicate with each other. Key design requirements for such WBANs are:

- Suitable signal transmission for the human body, e.g. not to have any negative health effects for the user;

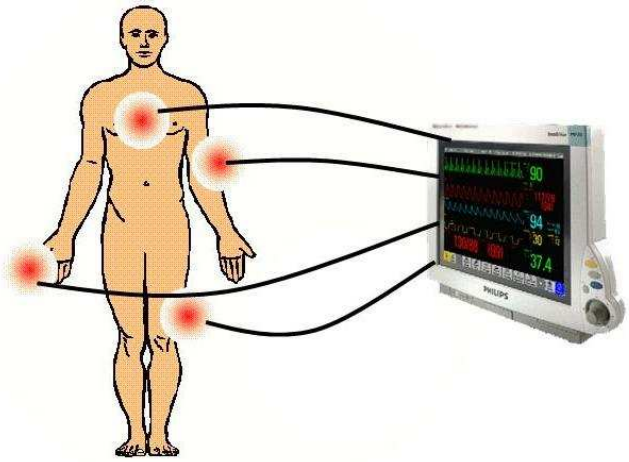

Fig. 1.1: Illustration of today's medical monitoring.

- Reliability: Reliable wireless communication between portable devices in close proximity to the human body. To this end, the influence of the body on the propagation of the communication signal should be taken into account;

- Power efficiency: Every device should be able to function for a long period with a small battery;

- Security: As every person carries his own body network, interference between BANs and security become a critical issue;

- Data rate: A rate of 1 to 10 Mbps is desired. However, choosing a suitable physical layer approach might yield a higher data rate.

Standard RF based technologies can be used as basis for WBANs. However, these solutions are only partially suited for WBANs. Table 1.1 compares the relevant parameters of Bluetooth v2.0, Zig-Bee, radio frequency identification (RFID) ultra high frequency (UHF) and near field communication (NFC).

Bluetooth is a high data rate solution, whereas ZigBee features low transmission power. Although one of the application areas of these solutions is wireless personal networks, the main challenge of employing them is the overlapping coverage areas between different BANs, see e.g. [3], [4]. Therefore, this reduces the security and throughput of these solutions for BANs especially when the devices off, but near the body, are communicating with each other or interfere with each other. Moreover, Bluetooth modules also consume relatively high power and ZigBee

Table 1.1: Comparison of the key characteristics of different RF technologies.

	Bluetooth v2.0	**Zigbee**	**RFID UHF**	**NFC**
Frequency	2.4 GHz	2.4 GHz	860-960 MHz	13.56 MHz
Range	100 m	20 m	5 m	0.1 m
Max. data rate	3 Mbps	250 kbps	160 kbps	424 kbps
Transmission power	10 mW	1 mW	<1 mW	<1 mW

offers insufficient data rate, which are in contrast to the BANs requirements listed above. Another drawback of these RF-based WBANs is their limited body coverage due to body shadowing, as e.g. reported in [5], [6]. RFID and NFC are low power, short range wireless connectivity technologies. However, they offer data rates which are not desirable for the WBANs. Also, they do not allow for networking.

Therefore, due to the sketched problems of the RF-based technologies, a novel transmission technique has been proposed in the 90s, which seems a promising approach for WBAN [7], [8]. In this solution, which we will refer to as body-coupled communications (BCC), the human body is used as the propagation medium for the data signals. As illustrated in Fig. 1.2, in this approach the devices can be placed on, or very close to, the human body and communicate with each other via the body.

1.2 Body-Coupled Communications Technology

In the BCC technology, the human body serves as a communication channel. The basic principle of BCC is that a small electric field is induced onto the human body in order to propagate a signal between devices that are in the proximity of, or in direct contact with, the human body. Two conceptually different approaches to induce the electric signal onto the body have been previously proposed: capacitive coupling and galvanic coupling. These two coupling approaches are explained further in Sections 1.2.1 and 1.2.2, respectively.

For both approaches, the BCC transceiver nodes consist of a transmitter (TX) and a receiver (RX), together connected to a coupler. Each coupler is composed of two electrodes. For galvanic coupling, these electrodes need to be placed on the skin directly. For capacitive coupling, there is no need for a direct human skin contact, however, close proximity of the coupler to the body is required. These electrodes can be structured horizontally or vertically where the spacing between them is filled by a dielectric material. These two types of electrodes structures are depicted in Fig. 1.3. The vertical structure is only used for the capacitive body coupling approach,

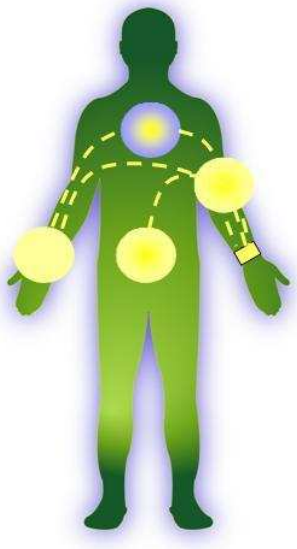

Fig. 1.2: Illustration of a body-coupled communications (BCC) network with 5 devices.

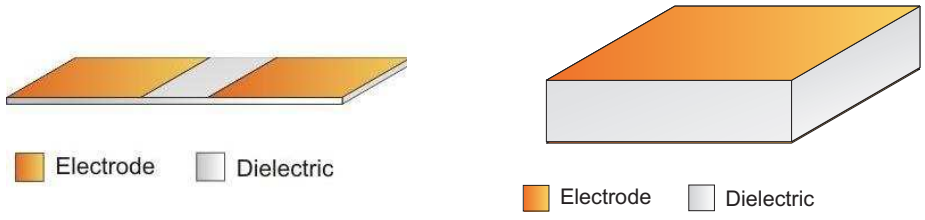

(a) Horizontal structure. (b) Vertical structure.

Fig. 1.3: Coupler structure for capacitive/galvanic body coupling.

while the horizontal structure can be applied for both approaches. It is noted that in the horizontal structure, the electrodes can be oriented on the body in a longitudinal or transversal direction as defined in Fig. 1.4.

1.2.1 Galvanic body coupling

Figure 1.5 illustrates the galvanic coupling approach. At the TX an electrical signal is applied differentially between two electrodes that are directly attached to the human body. A current results between these two electrodes. This induces a very small (secondary) electric current to propagate into the conductive body tissues. At the RX there are also two electrodes attached to the body. The induced current results in a differential signal between these two electrodes and is detected by them. This approach makes use of the dielectric characteristics of human tissue, therefore the flow of ions within the human body is the carrier of information. In this solution, the human body acts as a special kind of transmission line.

1.2.2 Capacitive body coupling

In capacitive coupling, as it is illustrated in Fig. 1.6, a differential pair of electrodes is used both for transmitting and receiving. At the TX side, a signal is applied between the electrodes and since the electrodes have a different capacitive coupling to the body, an electric field is induced to the human body and passes through the body. At the RX side, the two electrodes are at different distances from the body, so it is possible to detect a differential signal between them as a function of the varying electric potential of the person. In this approach, the human body acts as a conductor that forms a bridge between the TX and RX that are capacitively coupled to it. The environment is used as a reference to force or detect a variation of the electric potential of the human body.

(a) Longitudinal orientation. (b) Transversal orientation.

Fig. 1.4: Different orientations of the horizontal coupler structure.

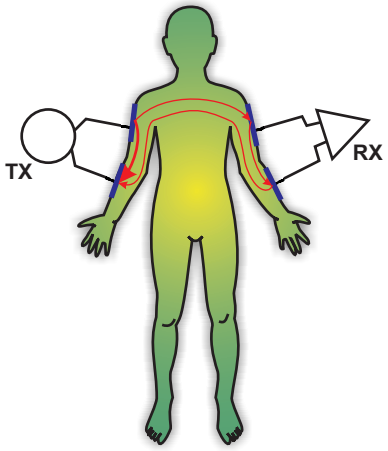

Fig. 1.5: Galvanic body coupling for data transmission between TX and RX.

1.2.3 Comparison of Coupling Approaches

Both approaches have their drawbacks and advantages from a technical and application point of view. The important difference between the two solutions is that the communication behavior in the capacitive coupling approach is strongly influenced by the environment around the body, while in the galvanic coupling approach it is more influenced by the body physical parameters.

From the application perspective, a significant difference between the two approaches is that the capacitive approach does not require a direct contact between the coupler and the human body, while for the galvanic coupling this is preferred, if not necessary. In other words, the galvanic coupling requires the transceiver devices to be fixed to the person with the electrodes in direct contact to the skin, while the capacitive devices can be just in its proximity and more loosely coupled. For that reason we consider the capacitive approach to be the most relevant and hence we focus here on this approach.

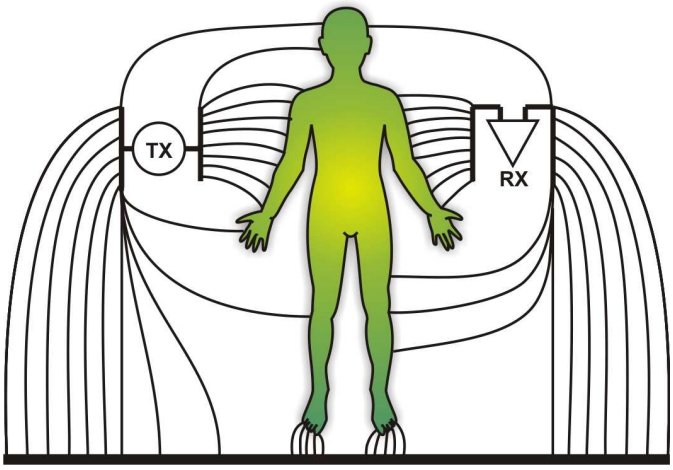

Fig. 1.6: Capacitive body coupling for data transmission between TX and RX.

1.3 Motivation of Work

In BCC, the communication channel is different from traditionally studied RF-based communication channels. Therefore, to design a suitable connectivity solution based on capacitive BCC a better understanding of the characteristics of the human body as a communication channel is required.

So far, the theoretical investigation of the BCC channel provides limited understanding of the on-body channel behavior. Moreover, as we will review in Chapter 2, there are some experimental studies on the human body channel characterization and modeling approaches presented in previous literature. However, the results of these works are limited to the "grounded case", i.e. in their system set up the channel not only contains the body channel, but also the effect of the standard measurement equipments which are strongly coupled to the earth ground.

Therefore, it is required to study the BCC channel to have a clear understanding of the on-body channel behavior. This can be fulfilled by studying the mean and variation in attenuation of a signal propagating through the body. These two parameters determine the required transmit power and receiver sensitivity for the system design. It is, moreover, beneficial to understand the variation in these parameters as function of frequency, to be able to determine the optimum communication band and the available bandwidth. To this end, the BCC channel characterization is experimentally investigated in this work.

Furthermore, to improve our understanding of the BCC channel, experimental results are used to develop a model for the on-body channel behavior. This model, then, can be used for system simulations in order to for example evaluate the multiple access scheme, physical layer and protocol layers.

Finally, a physical layer needs to be designed for BCC to be matched to the characterization of the body channel that we found by our experimental study.

1.4 Objectives

The aim of the project, the result of which are in this report, was to explore the human body as a communication medium for data transmission. For this purpose, the objectives of this study are to:

- characterize the capacitive BCC channel based on an experimental study;
- investigate the influence of the coupler design, coupler positions and body movement on the propagation loss by employing a specifically designed measurement system;
- characterize the interference and to investigate its influence on BCC;
- develop a BCC channel model based on the experimental results to be used to analyze the BCC system performance;
- design a physical layer suitable for BCC channel and to numerically evaluate the performance of the system by using the developed interference and on-body channel models.

1.5 Outline

The outline of the rest of the report is as follows. In Chapter 2, we will give an overview of previous work on BCC channel characterization and modeling by other research groups. Chapter

3 presents the measurement system, which has been designed for BCC channel characterization and the measurement setups for our experimental study. The different structures and constructions for the BCC node design are discussed. In Chapter 4, the test scenarios for the experimental study are explained. Moreover, it presents the obtained experimental results from our measurements for relevant system parameters like signal attenuation, coupler design, coupler positions on the body and interference. These are used to draw conclusions about the fundamental properties of BCC. Chapter 5 uses these experimental results to develop a model to describe the mean propagation loss behavior. Additionally, a model is developed for the variation of the propagation loss around the mean caused by body movement. Subsequently, Chapter 6 proposes a physical layer design for BCC based on the characteristics derived in the foregoing chapters. It is named adaptive code-spreading. Finally, conclusions are drawn and recommendation for further work are given in Chapter 7.

Chapter 2

Literature Review

2.1 Introduction

Several studies have been previously performed to investigate sending and receiving data through the human body using BCC. Some attempts also have been made to characterize BCC and to model the human body communication channel. The main differences between these investigations are due to different coupling schemes, signal strengths, frequency ranges, data rates, transceiver coupler sizes and structures, body channel modeling approaches and signal modulation methods. In the following, the most important studies reported in literature are introduced and their results are reviewed.

2.2 Zimmerman, MIT, 1995

The first study with respect to BCC has been performed by Zimmerman in 1995 in [7] and [8]. In his work, however, BCC is referred to as intra-body communication (IBC). In his study, the capacitive coupling approach is employed and the communication system consists of a TX and RX which are battery powered devices. The TX and RX are also electrically isolated from each other, so they do not share a common electrical ground. Both TX and RX are connected to a pair of vertically structured electrodes. The electrode size is in the order of centimeters. Data is transmitted by modulating electric fields and by capacitively coupling very small currents to the body. The body conducts the tiny signal to the RX which demodulates the signal. The environment provides the return path.

The author has developed an electrical model of the BCC system which includes the most important electric field paths in the system. In this model, the body is modeled as a perfect conductor and the electric coupling among the electrodes of the transceiver, body and environment is modeled as capacitors.

Several experiments and measurements have been performed by using different electrodes with different sizes and different positions on the body. The sizes and positions have been selected based on the possible applications grouped in commonly worn objects such as watch face, credit card, shoe insert and belt and head mounted personal area network (PAN) devices like headphones. The results show that placing a large area environment electrode close to the physical ground maximizes the magnitude of the received signal, so feet are the best location for PAN devices. Moreover, devices with larger electrode area and smaller intra-electrodes capacitance improve the communication performance.

Having established physical constraints of the system, two coding strategies and modulations, on-off keying (OOK) and direct sequence spread spectrum (DSSS) have been examined. The results showed that OOK modulation is only 60 percent as effective as spread spectrum. However, OOK modulation has been chosen since it is much simpler in implementation. In this study, a carrier frequency of 333 kHz and data rate of 2400 bps are applied.

2.3 Partridge et al., University of Washington, 2001

The original design of [7] has been extended by the authors of [9] by adding filters and amplifiers. In this study, quantitative measurements have been performed to determine the system performance under various circumstances. These includes variation in hand distances to the RX electrode and electrode locations on different positions on the body as a belt, on the wrist and in the shoes. Touch electrode sizes and shapes with different conductive materials and different subjects are also examined.

The results show that the electrode sizes and shapes have minor effects, but that the distance to the electrode and the location of the electrode significantly effect signal strength. The shoe performs better than the belt and wrist, because of its natural earth ground coupling. A larger ground electrode size results in an increased received signal strength. Similar results are obtained for experiments with different subjects. The developed prototype could achieve a data rate of 38.4 kbps and frequency shift keying (FSK) is applied to modulate the digital signal.

2.4 Fuji et al., Chiba University, Japan, 2003-2006

In the study by the authors of [10–13], the focus is on higher carrier frequencies, viz. from 10 MHz to 100 MHz. They claim that the body channel acts as waveguide for these frequencies. Capacitive coupling is used to send and receive electrical signals over the human body.

In this work, the authors have proposed calculation models of the TX and RX attached to the arm using finite-difference time-domain (FDTD). Next, they have compared the calculated received signal to the measured ones employing a tissue-equivalent phantom. In their measurement system, the signal is generated by a battery-powered TX and sent to the human body by two horizontally placed electrodes. The signal is received by two electrodes at RX side and measured by a mobile receiver.

In their experiments, the difference in the received signal level as a function of carrier frequency is investigated for different TX and RX electrode structures. The electrodes with different combination in size at the TX and RX side are also examined. Moreover, in order to find the optimal electrode orientation for the horizontal structure, two orientations —transversal and longitudinal— for TX electrodes have been investigated. In all the experiments the distance between the TX and RX is fixed.

The results show that there is a good agreement between the computed and measured signal levels. The received signal level strongly depends on the size of the transmitter; if the size of the TX is reduced by half, the signal strength is reduced by nearly fifty percent. The longitudinal direction is more effective than the transversal direction. The use of a ground electrode at the TX increases the received signal strength, hence it is advantageous to use it. The received signal level slightly decreases for higher frequencies.

2.5 Hachisuka et al., University of Tokyo, 2003-2005

In a study by the authors of [14] and [15], the characteristics of the BCC have been investigated for high frequencies from 1 MHz to 10 GHz. They claim that the human body acts as a waveguide for these frequencies.

In this work, two different electrode structures, the vertical and horizontal, have been introduced as four-terminal circuit model and two-terminal circuit model, respectively, to investigate the optimum electrode structure for BCC. Extensive measurements have been performed employing electrodes with different materials. Different body locations and different arm positions, such as arm held up, arm held horizontally and arm held down, have also been examined.

As measurement system, they developed a battery-powered TX and RX. The electrodes in the TX and RX sides are structured horizontally. The output signal is measured by connecting an oscilloscope to the RX side.

The results obtained from the measurements indicate that the vertical structure is superior to the horizontal structure in the MHz frequency range. Considering various arm positions, the arm held down had the lowest gain, which they claim to be a result of transmission direction inversion at the shoulder and interference on the surface and inside the body. It is also shown that the transmission characteristics are independent of the distance between the ground and the body. The electrode impedance is largely independent of the electrode materials, so stable communication can be achieved using different kinds of electrodes. The optimum frequency has been found to be approximately 10 to 50 MHz, as signals are gradually attenuated for frequencies above 100 MHz and exponentially above 1 GHz. Digital data transmission at 9600 bps using FSK at a carrier frequency of 10.7 MHz was reported.

2.6 Shinagawa et al., NTT laboratories, 2003-2004

A near-field-sensing transceiver for BCC has been developed by the authors of [16] and [17]. In their study, they used capacitive coupling for the data transmission.

An optical electric field sensor that exploits the electro-optic effect and laser light has been used for the receiving part of this transceiver. Since the sensor can measure electric fields independent of ground contact and has an extremely high input impedance, it is able to detect small unstable electric fields from the human body more accurately than the electrical sensors employed in previous studies.

The experiments have been performed employing a phantom body model. In the experiments the TX and RX electrodes are capacitively coupled to the phantom model. Their demonstration shows that this set up can support TCP/IP (10BASE) half-duplex communication at 10 Mbps.

They also experimentally verified that the intra-body communication and inter-body communication can be performed employing the designed transceiver. In the intra-body communication setup, the test person touches the electrodes of two transceivers by the right and left hands to confirm that the two transceivers can communicate through the human body. In the inter-body communication experiment setup, two test persons shake hands while each touches the transceiver electrode with the free hand . The result confirms that the two transceivers communicate via the bodies of the test persons.

2.7 Yanagida, Sony, 2006

A human body communication system with relatively high rate and low power consumption and without interference sensitivity using capacitive BCC is claimed in [18].

Experimental measurements have been performed to select a suitable transmission band and to obtain a proper configuration of the communication electrodes. Various electrode materials and sizes and structures have been examined in their experiments.

The results of the transmission loss measurements show that the vertical structure yields the lowest transmission loss. It is claimed that the electric capacity of capacitive coupling is proportional to the area of the electrodes, so the transmission range is expected to be improved by increasing the size of the electrodes specifically at the TX side. On the other hand, the electric capacity is inversely proportional to the distance between the electrodes. The measurement results also show that since the total distortion is small for a frequency band from 500 kHz to 3 MHz, it is optimal to use this frequency band for a good quality communication. It is claimed that this frequency band allows transmission at 48 kbps without any problem.

2.8 Hwang et al., ETRI, Korea, 2006

Signal transmission and inter-BCC network interference measurement results have been presented by the authors from Electronics and Telecommunications Research Institute (ETRI) in [19] and [20].

In this study, the interference between BCC devices of two persons has been examined experimentally. Two scenarios have been investigated; in the first, the TX and RX are on one person's body and in the second the TX is on one person's body and RX on another person's body. In their set up, the TX is fixed on the fingertips and the RX is located on two different positions on the body, 15 cm and 150 cm from the TX. Electrodes are structured horizontally and a single electrode size is employed. The interference signal propagates from one body to the other body in the second experiment.

In their measurement system, a battery-fed TX composed of a crystal oscillator is employed. The received signal at the RX side is measured by a spectrum analyzer.

The results obtained from the two scenarios allow the conclusion that the power of the interference is larger for the transmission distance equal to 15 cm than for the transmission distance equal to 150 cm in the second experiment and the signal interference increases as frequency increases. It is also concluded that the frequency band needs to be below 5 MHz to prevent a too high interference signal.

Moreover, the effect of ground electrodes on the transmission distance has been investigated. The results show that in the case of large distance between the TX and RX, the RX signal level increases when the ground electrode is attached to the body.

2.9 Wegmueller et al., ETH Zürich, 2005-2006

Galvanically coupling is presented as an approach for BCC by the authors of [21–23]. They have characterized the human body as a transmission medium for electrical current and modeled it by a simplified circuit model. The model is a four terminal circuit model with 10 impedances representing the coupling electrode impedances, the input and output impedances, as well as the longitudinal transmit impedance and a butterfly cross impedance.

In this work, the experimental study has been conducted on 20 subjects. The measurement has been performed by positioning the electrodes on a large number of different positions on the human body. These positions are classified into four groups: along the arm, on the thorax, along the leg and on the entire body. The influence of different electrode types and various sizes of TX and RX electrodes on signal attenuation have been investigated. Moreover, the level of signal attenuation for subjects with different tissue properties such as skin, fat, bone and muscles have been assessed by finite element simulation.

It is concluded from these results that high variation of the transmission attenuation at different location on the body occurs. The thorax showed excellent transmission characteristics, while the extremities and joints resulted in additional attenuation. Consequently, transmission over larger distance will result in lower RX signal levels. The size of the RX electrodes has a neglectable impact, while the attenuation decreases with an increased size of the TX electrode. Better coupling and more stability in the signal transmission were observed during body activity.

It is concluded from the tissue modeling and simulation that when a current is applied to the pair of TX electrodes, the largest voltage drop is present over the skin, compared to the other tissues such as fat, bone and muscle. Therefore, the properties of the skin are crucial with respect to the performance of the skin. Results from different skin models (wet, dry, wet and dry) showed that the attenuation is the lowest for the combined (wet and dry) approach. The reason is that because of a good contact between the electrodes and skin the current induces a smaller voltage for the coupling into the arm.

The suitable frequency range has been identified from 1 kHz to 10 MHz. Data transfers up to 255 kbps were achieved with digital modulation types, OOK, FSK and BPSK.

2.10 Ruiz et al., Waseda University Japan, 2006-2007

The propagation characteristics of the human body for higher frequency signals up to 3 GHz have been investigated in [24–27]. The variation of the BCC channel is statistically modeled in terms of the best fitting distribution function. In these works, the human body is considered as a waveguide with the RF signal propagating through the body.

Several investigations have been done considering different configurations for TX and RX. In their measurement system, a 12 dBm TX signal is generated by a signal generator and transmitted onto the body via a coupler. The power of the received signal at the RX side is measured by a spectrum analyzer. Furthermore, the ground of both TX and RX is connected to the electrical ground of the electrical devices that they are connected to. Experiments are performed exploiting vertical electrodes in different sizes and locations on the body. In these experiments, the ground electrode area is much larger than the signal electrode area and the separation between these two electrodes varies from 0.7 cm to 2.1 cm. The measurements have been performed for different scenarios, where the subject was sitting, standing and walking.

From the experimental study it is concluded that the received signal power decreases when the frequency increases. The power decreases more quickly for larger TX and RX distances. The results for sitting and standing tests were equivalent. Moreover, it has been concluded that the quality of the BCC link is higher when the test person is not moving. In their experimental study, they have also compared the human body and air channel. The results show a lower propagation loss for the intra-body channel than for the air channel. They claim that the suitable frequency range for BCC is from 200 MHz to 600 MHz where the lowest path loss is achieved based on their results.

Based on the experimental data, the normal distribution was found to be the best fit to model

the received signal power statistically. The results showed that the mean becomes smaller as the distance between the transceivers increases. Also, the standard deviation is larger for the walking test condition than for the statistic condition, as expected.

In these works, several digital modulation schemes have been evaluated by analyzing the constellation diagram, eye diagram and error vector magnitude (EVM), in order to determine the most suitable one for BCC. In these experiments, the employed frequency carriers are 200 MHz and 600 MHz and symbol rate is from 100 ksps to 5 Msps in order to analyze the maximum data rates achievable through each modulation scheme. The experimental results show that MSK and BPSK are the most suitable modulation schemes for BCC, since they meet the posed EVM requirements. However, an increase of symbol rate and distance between TX and RX yields a very high level of distortion for all modulation schemes.

2.11 Choi et al., KAIST, 2006-2008

Different aspects of BCC were investigated by the authors of [28–35]. In these works, different transceiver designs, a distributed RC-model of the human body and characterization of the human body as a new communication method have been presented.

In these works, to achieve low power consumption and a high data rate, a wide band transceiver with a direct-coupled interface (DCI) has been implemented for BCC. In their measurement system set up, a battery-fed crystal based TX is employed and only a single electrode is used to transmit the data to the body. At the RX side, a single electrode is connected to a digital oscilloscope and its ground is floated to isolate it from the signal ground of the TX. This transceiver with a fixed data rate and without any modulation is not suitable for a shared body channel. Hence, it has been modified to a scalable PHY transceiver.

The PHY transceiver adopts the DSSS for both fast code acquisition and narrow band interference rejection. On the other hand, the employed 1 bit ADC in this design cannot provide a dynamic range to cancel various interferences that attack the wideband signal. Thus, in their next study, the authors come up with a conclusion to divide the communication frequency band to 4 sub-bands and to utilize adaptive frequency hopping (AFH). Inside each sub-band, a 10 Mbps FSK signal is applied. Their results show that the AFH can improve the signal to interference ratio (SIR) performance of BCC by more than 10 dB.

Furthermore, an RC model of a T-shaped human subject has been developed to characterize the human body as a channel for BCC. This model consists of cascaded unit blocks with an RC parallel network and shunt capacitors. For their study, the TX in their experimental measurement system consists of a battery-powered signal generator with a programmable frequency synthesizer and two vertically structured electrodes. The RX consists of a single electrode in the same shape and dimension of the TX signal electrode. The received signal is measured by connecting a spectrum analyzer or a digital oscilloscope to the electrode at the RX side. With this setting the receiver shares its ground with the earth-grounded instruments which results in an increment in the strength of the return path. However, they claim that the level of increment is 6 dB and has been considered in their analysis.

Different sizes of the ground electrode at the TX side are used to investigate their effects on the received signal level. Moreover, extensive measurements have been done on various subjects with different height, different distances between TX and RX in sitting and standing situations. For these measurements, TX output power is fixed to 3 dBm and the body channel is measured up to 150 MHz.

Based on their results they claim that below 4 MHz the channel is deterministic and looks

like a high-pass filter. However, beyond 10 MHz the power loss increases when the distance between TX and RX increases. The results also show that the ground electrode size has little effect on the overall shape of the channel response. The material of the electrode has little effect on the magnitude of the received power.

2.12 Conclusions and Discussion

All the reviewed studies in this chapter present the human body as a propagation medium and propose different approaches to characterize BCC. Table 2.1 indicates the summary of these works based on their focus on the communication system, channel measurement and modeling.

In early studies by the authors of [7], [8], [9], [10–13], [14], [15], [18], [19] and [20] there was no investigation neither on the human body properties nor on the human body channel modeling. In most of these works the main focus was on the BCC characterization by developing a test module and they did not characterize the BCC channel.

In some studies, they worked on the influence of the coupler structure and size on the BCC performance. The authors of [14], [15] and [18] showed that utilizing the vertical electrode structure is superior to the horizontal structure. On the other hand, it was presented by the authors of [10–13] that employing horizontal structure, longitudinal orientation will give better results than the transversal orientation. In their work, the authors of [7], [8], [9], [10–13], [18], had a common conclusion about the electrode size. Based on their results, they showed that using an electrode with a larger area specifically at TX will result in less propagation loss. However, in the study by the authors of [9], it has been shown that the electrode size has minor effect on the transmission performance. Most of these works investigated the influence of the ground electrode. The works [7], [8], [9], [10–13], [19] and [20] reported that using a ground electrode will improve the performance of BCC effectively.

The propagation loss behavior as a function of frequency was only presented in the studies by the authors of [14], [15], [19], [20], [10–13], although the frequency band that they focused on to investigate the BCC characteristics is not the same. The achieved results reported in [14], [15], [19], [20] showed that propagation loss decreases as the frequency increases. In contrast, it was reported by the authors of [10–13] that the propagation loss increases slightly in higher frequencies. This might be because all of their experiments were performed employing a phantom model that might not follow the behavior of the human body.

It is important to note that in the measurement presented by authors of [14], [15], [19], [20] the RX is connected to the earth ground via a network analyzer or a digital oscilloscope which significantly affects the results.

In recent studies, some contributions describe a characterization effort of the BCC channel and the human body properties. Characterization of the galvanic-coupled on-body channel and the human body properties have been presented in [21–23]. Since this solution requires direct skin contact, we do not consider this approach.

The capacitive-coupled on-body channel has been characterized and modeled by the authors of [28–35] and [24–27]. However, in these works at least one of the transceivers is connected to the ground earth via a main connection making the characterized channel to be different from the channel experienced during BAN operation.

Moreover, regarding to channel frequency behavior in the study in [24–27], it is shown that the received signal power decreases as frequency increases. Since in these works the body characteristic investigation is in the frequency band of 200 MHz to 600 MHz, the human body

behaves electrically as an antenna and consequently radiates the signal into the space rather than to the coupler. The BCC frequency behavior is also characterized in the study by authors of [28–35]. In their work, it is explained that the human body behaves as a high pass filter for frequencies below 4 MHz. However, in their measurement setup the received power was measured by a digital oscilloscope, therefore, the digital oscilloscope input impedance in combination with the capacitive effect of the BCC device might provide a high pass filtering which suppresses the received power in low frequencies.

It is concluded by reviewing these works that first regarding coupler design, there is no conclusive investigation on the electrode size and specifically the spacing between the electrode pair. Second, there is no investigation for the body coverage area in capacitive coupling where the coupler can be placed on/off the body. There is not a clear understanding of the on-body communication channel behavior, since in most studies the presented channel behavior was influenced by ground connection via measurement equipment. Finally, little is known about interference behavior.

Hence, in this work, BCC characterization and on-body channel behavior will be investigated comprehensively based on an experimental study of the BCC channel.

Table 2.1: Summary of the results of the most important studies on BCC.

	Zimmerman	**Partridge**	**Fuji**	**Hachisuka**	**Shinagawa**
Model	Electrical	Not applied	Not applied	Not applied	Not applied
Coupling Scheme	Capacitive	Capacitive	Capacitive	Capacitive	Capacitive
Freq. Range	100 kHz - 500 kHz	140 kHz - 180 kHz	10 MHz - 100 MHz	10 kHz - 50 GHz	Not reported
Modulation	OOK	FSK	OOK	FSK	Not reported
Data Rate	2.4 (kbps)	38.4 (kbps)	9.6 (kbps)	9.6 (kbps)	10 (Mbps)
Location on Body	arm, foot, waist, head	waist, wrist, foot	arm	arm	hand
Electrode Size	25×25 mm^2	15×15 cm^2	2×3 cm^2	30×30 mm^2	Not reported
	30×30 mm^2	30×14 cm^2	1×3 cm^2	20×20 mm^2	
	70×20 mm^2	100×100 cm^2	0.5×3 cm^2		
	80×80 mm^2	250×250 cm^2			
	130×40 mm^2				
	900×25 mm^2				
Orientation	Vertical	Vertical	Horizonal	Horizonal	Single electrode

	Yanagida	**Hwang**	**Wegmuller**	**Ruiz**	**Choi**
Model	Not applied	Not applied	Electrical	Statistical	Electrical
Coupling Scheme	Capacitive	Capacitive	Galvanic	Capacitive	Capacitive
Freq. Range	500 kHz - 3 MHz	0 - 5 MHz	1 kHz - 10 MHz	200 MHz - 600 MHz	1 kHz - 100 MHz
Modulation	Not reported	Not reported	FSK, BPSK	BPSK,MSK	FSK
Data Rate	48 (kbps)	Not reported	128, 255 (kbps)	100-2500 (kbps)	10 Mbps
Location on Body	waist, head	arm, wrist	arm, wrist, leg	arm, waist, ear, foot	wrist, chest, waist
Electrode Size	20×20 mm^2	2×2 cm^2	880 mm^2	π/4 cm^2	Not reported
	40×40 mm^2		54 cm^2	π cm^2	
	20×80 mm^2		560 cm^2	4π cm^2	
	80×80 mm^2				
Orientation	Horizonal/vertical	Horizontal	Horizontal	-	-

Chapter 3

Measurement System

3.1 Introduction

As we have discussed in Chapter 2, the phenomena studied to characterize BCC in the literature are not comprehensive and they are not fully understood. Furthermore, the presented on-body channel behavior and models get influenced by the used measurement systems which are hence not applicable to our scenario. The goal of this study is to experimentally characterize BCC and to achieve a clear understanding of capacitive on-body channel experienced in a body-area networks (BANs) environment. Therefore, a measurement system needs to be implemented such to satisfy the requirements of our scenario.

This measurement system should provide the actual situation of BANs. So, the standard equipments as signal generator or data analyzer cannot be used here, since these earth-grounded instruments have effect on the strength of the signal being send to the human body. Moreover, the input impedance of the data analyzers such as oscilloscope or network analyzer is not high enough and might have influence on the measured data and behavior of the channel. The size of the measurement system should also be suitable for practical use. Finally, the measurement system is required to be isolated from any other devices to clarify that the measured data is not affected by any other sources. Based on our requirements, a measurement system has been developed at Philips Research for our experimental study of the BCC channel properties.

This chapter presents the developed measurement system. In Section 3.2, the measurement system architecture is introduced. In Section 3.3, the design of couplers used to transfer the signal to/from the body is introduced. The measurement system set up is explained in Section 3.4. The calibration of the measurement system is discussed in Section 3.5. Finally, Section 3.6 presents the setup used for characterization of interference.

3.2 Measurement System Architecture

The developed measurement system, as depicted in Fig. 3.1, consists of a battery-fed TX and RX pair connected by an optical cable. This cable is used to synchronize their functionality. Two differential coupler pairs are capacitively coupled to the body to transmit a signal over or receive a signal from the human body. The whole system is galvanically isolated from the earth ground. This was a key requirement of the system, as we wanted to characterize the channel experienced when BCC would be used in a body-area network environment. Moreover, due to the optical cable, the TX and RX are also galvanically isolated from each other, which assures that the measured data is just related to the characteristics of the human body and is not affected

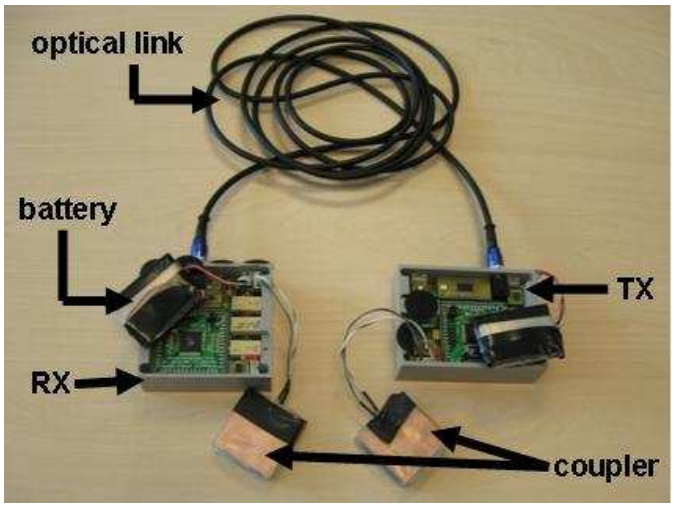

Fig. 3.1: Measurement system overview: battery-powered TX and RX are connected to each other by an optical cable.

by any other sources such as a cable or a shared earth ground.

In this study, we aim to examine the transmission characteristics of the human body for various frequencies to understand the frequency behavior of BCC and to determine the optimum frequency band for the BCC. Thus, in our measurement system TX consists of a direct-digital synthesizer (DDS) used as a tunable frequency source to sweep the frequency band of interest, i.e. 100 kHz to 60 MHz. Figure 3.2 depicts the functional block diagram and implementation unit of the TX. Control words received on an SPDIF-based (Sony/Philips Digital Interface Format) optical link, used for the TX and RX synchronization, are interpreted by the microprocessor and are used to determine the corresponding setting for the DDS. The output of the DDS is filtered and amplified before being transmitted through the body via the coupler. The TX output power is approximately 12 dBm, which is selected based on the basic limit for the safety of the human body.

The high input impedance RX basically consists of a power detector to measure power at different frequencies. In the measurement system, this input impedance of the RX has a strong

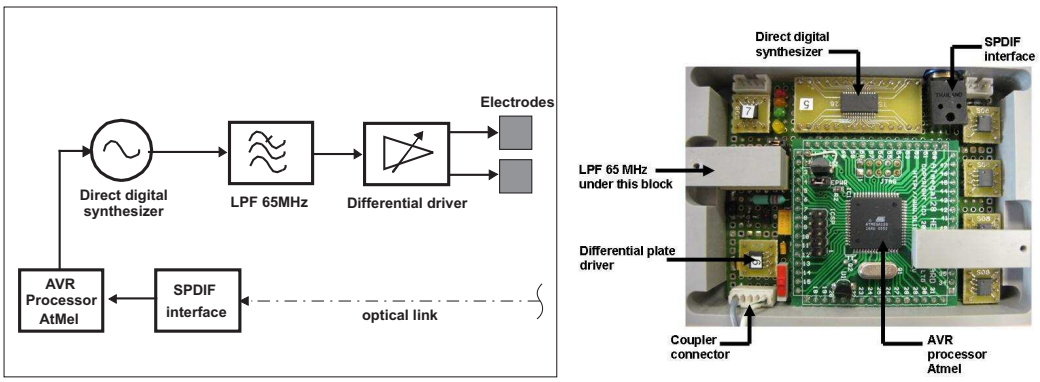

(a) Block diagram. (b) Implementation.

Fig. 3.2: Transmitter of the BCC channel characterization system.

effect on the characterization of the BCC channel. BCC devices are AC coupled to the human body. The related capacitive effect and the input impedance of the RX are in series and they might provide a high-pass filtering of the incoming signal. Therefore, the input impedance of the measurement system is chosen high enough to stop this high-pass effect at reasonably low frequency.

Figure 3.3 depicts the functional block diagram and implementation unit of the RX. The signal received by the coupler is amplified using a low noise amplifier and filtered by a band-pass filter. One of the three filters can be selected manually such to get tuned to the measurement frequency range thereby limiting the interference and noise contributions. Next, the power of the filtered signal is estimated by the power detector and then is sampled by a 12-bits analogue to digital convertor (ADC). The power detector dynamic range is 95 dB. Using a microprocessor after the convertor, the measurement results are stored in the processor's memory. Subsequently, the microprocessor requests the TX to transmit the signal with the next frequency. This process is repeated until all measurements in a set are performed. The data stored in the microprocessor memory can be written onto an SD-memory card to get analyzed off-line later or these can be processed in real time via an opto-coupled RS232 interface which is connected directly to a PC. When the first operation mode is used, the RS232 cable is not connected.

This RS232 interface is also used to configure the microprocessor at the beginning of each measurement. Using the accompanying graphical user interface (GUI), the frequency range of interest, the number of points in the frequency range and the number of measurements per experiment can be set. Moreover, since a large battery pack and a large memory are applied, long measurements (in order of hours) can be performed to acquire a large set of subsequent data.

The size of the TX and RX circuit boards are $7 \times 9.5\ \mathrm{cm}^2$ and $7.8 \times 8\ \mathrm{cm}^2$, respectively. These boards are placed in two separate plastic boxes to isolate them from influence of the equipments and the body that they are placed on. However, the measurement system with the current design can be affected by interference as the power at each frequency is integrated at the whole band of the selected filter. In our investigation in Section 3.6 and Section 4.3.7, it is verified that this does not pose a problem.

It should be noted that, since in BCC the communication range should be confined to the vicinity of the human body, the frequency range of interest is limited, i.e. 100 kHz to 100 MHz. Transmission at very high frequencies and very low frequencies is not considered. At frequencies above 100 MHz, the wavelength is 3 m, which is in the same order of magnitude as the length of a person. At such frequencies, the body behaves electrically as an antenna and radiates

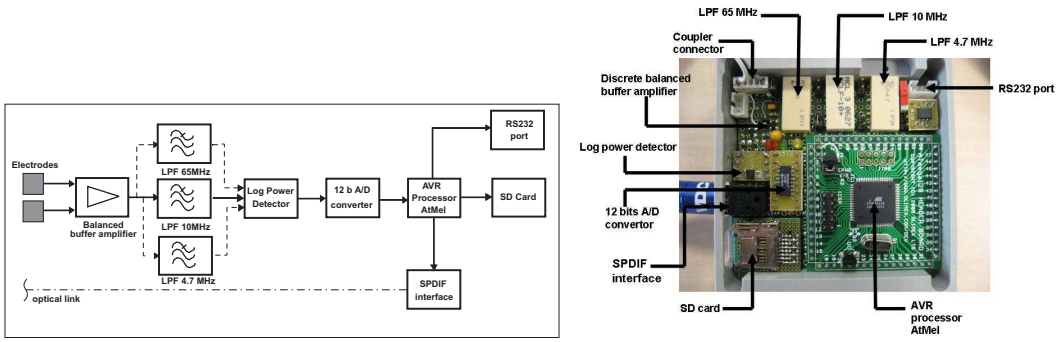

(a) Block diagram. (b) Implementation.

Fig. 3.3: Receiver of the BCC channel characterization system.

signals into its environment. Moreover, even the electrode starts acting as an antenna at higher frequencies. To avoid these two effects and to limit the communication to on, or close to, the body, the frequency range of interest is less than 100 MHz. At very low frequencies, communication might be influenced by electromagnetic interference, thus 100 kHz is selected as lower frequency of the BCC band. Measurements are consequently performed from 100 kHz to 60 MHz in all the investigations in this study to be sure that the body channel is not affected by body radiating.

3.3 Coupler design

The couplers consist of flat electrode pairs made of copper. For the experiments they are placed close to the human body to transmit signals generated by the TX over the human body and to pick up the differential signal at the RX side. In order to avoid direct contact between metal of the couplers and the human body, the metal surfaces are covered with isolation tape.

As explained earlier in Chapter 1, the couplers can be structured horizontally or vertically in the capacitive coupling approach. In horizontal structure, two parallel electrodes are placed on or close to the surface of the body where the space between them is filled with printed circuit board (PCB) material. In vertical structure, one electrode is positioned on or close to the surface of the body while the other one is opposed to it. The volume between them is filled with PCB material and/or polyvinyl chloride (PVC) foam (see Fig. 3.4(a)).

The measurement system is developed to investigate the transmission and coupling scheme characteristics, so it is built such that different couplers can be attached easily to it. To study the influence of the coupler design on the BCC channel behavior, different couplers are used that vary in electrode dimension, space between the electrode pair and the structure of the electrode pair. Figure 3.4 illustrates the different coupler configurations and electrode structures used in this investigation.

The characteristics of the different couplers with different electrode dimension and spacing between electrode pair are studied by performing measurements. The goal is to come up to the optimal size based on these experimental results. It is also examined what the best structure of the electrodes is and whether it is more efficient to couple these to the human body horizontally or vertically.

3.4 Measurement System Setup

Figure 3.5 depicts the schematic representation of a typical measurement system setup on the human body. For the experiments, both the TX and RX of the system are placed on the body. Couplers with different configurations and orientations are attached to them and capacitively coupled to the human body. The couplers are taped loosely to the body so that they cannot move while a measurement is being performed.

Most of the measurements have been performed in a conference room in Hightech Campus 37, floor 5, room 5.021A. The room is $2.70 \times 4.30\ \mathrm{m}^2$, has two glass walls and does not contain electronic equipments. Most of the experiments are performed on the same subject, female, height $= 1.54$ m.

The initial settings for each experiment are defined in the GUI. The frequency range is set to 100 kHz to 60 MHz. This frequency band is selected regarding to the BCC frequency band of interest as discussed in Section 3.2. The number of samples in the equally spaced frequency band is 255; the number of measured data per frequency sample is 255. The duration for the whole

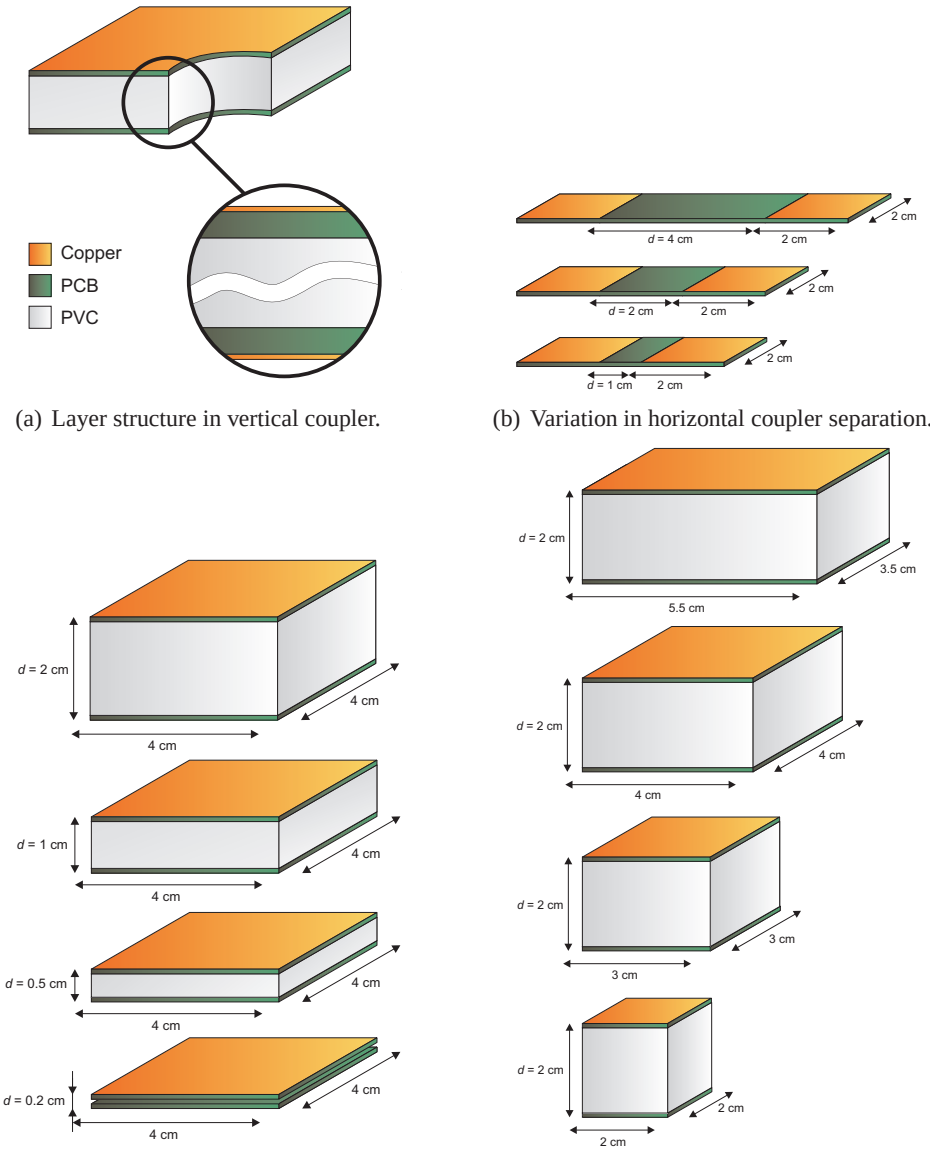

(a) Layer structure in vertical coupler.

(b) Variation in horizontal coupler separation.

(c) Variation in vertical coupler separation.

(d) Variation in vertical coupler size.

Fig. 3.4: Different coupler configurations and structures.

255 of the measurements is 2.5 minutes and consequently the duration of each measurement is less than one second.

3.5 Measurement System Calibration

Since the end goal is to characterize the human body channel, the power measurement results need to be translated into propagation loss results. To this end, a back-to-back calibration is required to measure the loss occurring due to the measurement system. Figure 3.6 depicts the TX and RX back-to-back setup. To avoid the RX to saturate, the TX and RX are connected via an attenuator, therefore, no couplers are applied. For this measurement, the attenuation between the TX and RX is constant over the frequency band and equals to 30 dB. The measured power

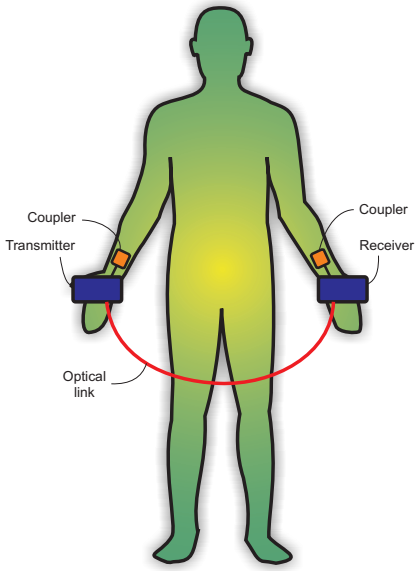

Fig. 3.5: Schematic of a typical measurement setup.

can be expressed as a function of frequency f as

$$P_{RX_{\mathrm{b2b}}}(f) = H(f)P_{\mathrm{TX}}(f)/A_{\mathrm{b2b}}(f), \tag{3.1}$$

where $H(f)$ denotes the transfer function of the system, P_{TX} denotes the output power of the TX and A_{b2b} denotes the back-to-back attenuation. Therefore,

$$H(f)P_{\mathrm{TX}}(f) = P_{\mathrm{RX}_{\mathrm{b2b}}}(f) \cdot A_{\mathrm{b2b}}(f). \tag{3.2}$$

The propagation loss level of the channel for all the experiments is obtained by using the achieved results of (3.2) and measuring the received power. Thus,

$$P_{\mathrm{RX}_{\mathrm{Meas.}}}(f) = H(f)P_{\mathrm{TX}}(f)/A(f), \tag{3.3}$$

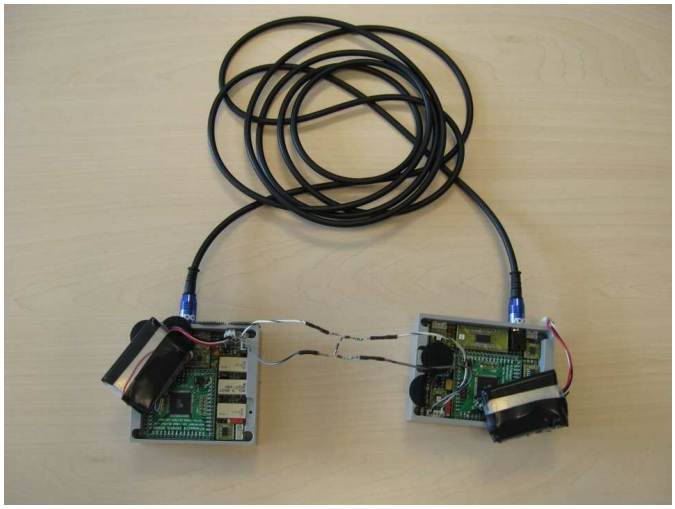

Fig. 3.6: Back-to-back measurement setup.

where $A(f)$ denotes propagation loss through the body. Using (3.3) and substituting the calibration result from (3.2), we can calculate the body attenuation, which is given by

$$A(f) = H(f)P_{\mathrm{TX}}(f)/P_{\mathrm{RX}_{\mathrm{Meas.}}}(f). \tag{3.4}$$

The calibration measurement results are depicted in Fig. 3.7. The characteristics of the TX power were achieved by adding the 30 dB back-to-back attenuation to the received power. The TX power is around 12 dBm.

3.6 Interference Measurement Setup

As explained in Section 3.2, in the designed measurement system the received power at each frequency is integrated over the whole band of the selected filter. Therefore, our measurement system is not sensitive enough to analyze signal interference characterization. Hence, the interference characterization measurements are performed using a battery-fed portable spectrum analyzer, [36], with a probe with an input impedance equal to the one used for the measurement system explained in Section 3.2. The spectrum analyzer is chosen to be portable and battery-fed to characterize the experienced interference for the body channel in a BAN environment. Moreover, since the input impedance of the spectrum is not high enough and also to be sure that the measured data are comparable to the data measured by our designed measurement system a circuit is specifically designed for the input impedance.

The measurement setup is illustrated in Fig. 3.8. All the experiments are performed employing a 4×4 cm^2 coupler with 1 cm electrodes spacing, located at the wrist of the test subject. The spectrum analyzer measurement bandwidth is 30 kHz per measurement point. The number of measurements per frequency point is 20 and the power is averaged over these points. The number of measured points in the whole frequency band from 100 kHz to 60 MHz is 301, which are equally spaced. It is noted that the low frequency behavior is mainly limited by the phase

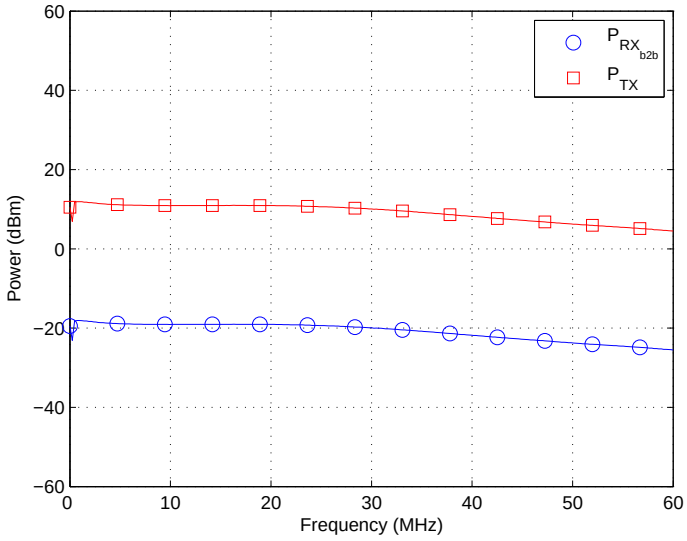

Fig. 3.7: Calibration results: measured received power and calculated transmit power from back-to-back setup.

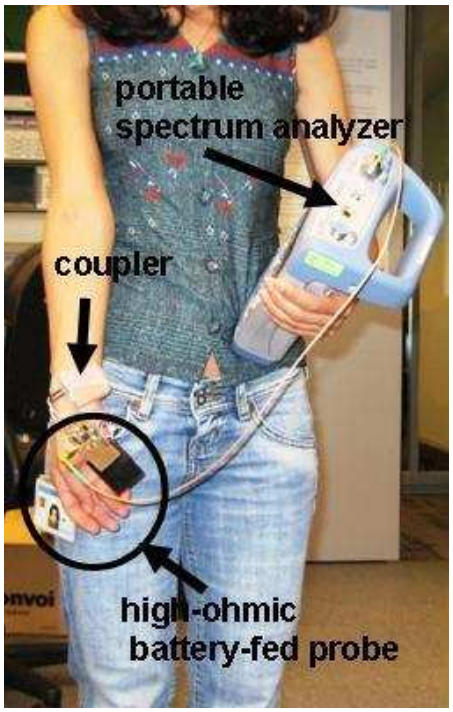

Fig. 3.8: Interference measurement setup.

noise behavior of the spectrum analyzer. Therefore, it is hard to draw conclusions about the interference for these frequencies from these measurements. In a separate session, the frequency band is set to 100 kHz to 2 MHz, with 301 equally spaced measurement points to examine the interference behavior for the low frequencies. In this setting, the spectrum analyzer measurement bandwidth is 3 kHz per measurement point. The number of measurements per frequency point is 40.

To assure that the interference induced by our designed channel characterization system, e.g. due to the 100 MHz microprocessor, does not have impact on our measured data, the following experiment has been carried out. In the measurement set up, the channel characterization system and spectrum analyzer are both placed on a table and the interference power has been measured by the spectrum analyzer. The results of this experiment have been compared to the lowest possible level of the spectrum analyzer (determined with disconnected probe). Figure 3.9 shows the achieved results. As it is depicted, the observed spectral characteristics in both situations are similar. Thus, the interference due to the receiver is minimal and does not influence the results.

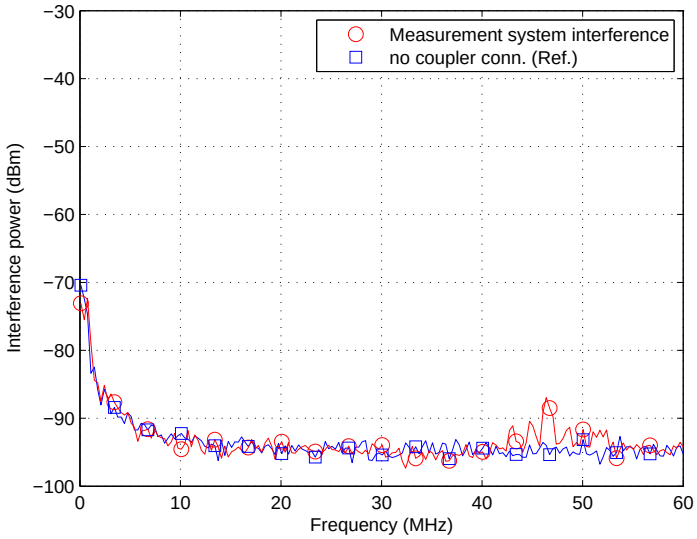

Fig. 3.9: Measured interference power of the channel characterization system together with the lowest possible level of spectrum analyzer.

Chapter 4

Experimental Results

4.1 Introduction

The BCC channel is different from that for the other RF solutions proposed to establish WBANs. Consequently, it is necessary to have a good understanding of the BCC characteristics and the on-body channel behavior in order to effectively exploit the human body as a communication medium and in order to find their impact on design parameters. As described in Chapter 2, the current experimental investigations on BCC are not exhaustive and in several cases their studies are limited to the "grounded" scenario. Consequently, in this work we try to fully characterize the capacitive BCC channel by an experimental study. From the results, conclusions for empirical and statistical BCC channel modeling can be drawn.

The developed measurement system, described in Chapter 3, is used to perform extensive experiments to reveal the influence of coupler size and structure on BCC. It is, moreover, used to understand the signal transmission characteristics in static situations and due to body movement for different node positions on the body. All of these experiments are performed focused on propagation loss and its variation in the frequency band of 100 kHz to 60 MHz. Moreover, to study the impact of interference on BCC and to characterize its properties, several measurements are carried out employing the dedicated measurement setup explained in Chapter 3 based on the portable spectrum analyzer.

The test scenarios, a dedicated test strategy and the measurement setup are discussed in Section 4.2. The achieved experimental results are presented in Section 4.3. In Section 4.4, the conclusions from the experimental results are summarized and discussed.

4.2 Test Scenarios

In this section, the tests methods used for our experimental study are introduced. First, the test parameters that play an important role to reveal the fundamental properties of BCC are presented and the test scenario for each parameter is explained. Next, the test methods performed in this thesis are presented.

4.2.1 Parameters to be investigated

Experiments are carried out to study the impact of (i) the coupling schemes (galvanic or capacitive coupling), (ii) the distance between the TX and RX and (iii) the configuration of the coupler, such as the electrode structure, the electrode dimensions and the electrode pair spacing

on BCC. Further experiments investigate (iv) the distance between the coupler and the human body, (v) static or dynamic situation of the human body, (vi) properties of the human body structures (different test persons) and (vii) impact of various environments on BCC. In all of these experiments, it is important to examine the frequency behavior of the propagation loss of the BCC channel as a function of these parameters. Furthermore, some experiments are carried out to investigate the interference characteristics.

Frequency behavior

In this study, we are interested in understanding the BCC channel frequency behavior. In RF-based solutions, the channel generally shows severe frequency selectivity due to multipath fading, see e.g. [5]. The question is whether this also occurs for BCC. Therefore, the propagation loss of the channel is studied over the frequency band of 100 kHz to 60 MHz.

Coupling schemes

As introduced in Chapter 1, the galvanic coupling and capacitive coupling are the two different coupling schemes that can be used in BCC. The galvanic coupling only permits application in which the nodes are directly coupled to the body. These are mainly in the field of medical applications, but do not cover all wearable electronic devices. This thesis focusses on the capacitive coupling, which is not only applicable for the medical application field, but is also of large interest for consumer network solutions.

Distance between TX and RX

To assess the influence of the different distances between the TX and RX coupler, experimental tests need to be performed by positioning the two couplers on different parts of the body. The locations of the coupler are selected based on the possible application of BCC systems, where two devices interact with each other. Figure 4.1 depicts possible locations of the coupler on the human body and Table A.1 indicates the possible combinations of TX and RX locations on the body.

Electrode dimensions

The characteristics of couplers with different electrode dimensions and their influence on BCC are examined. The dimensions of the electrodes vary from the size of wearable devices to the size of sensor nodes. They are also selected based on the geometry of the human body. In this study, a TX and RX pair is considered to have the same dimensions in all the experiments. This is motivated by the fact that in practical systems all nodes will be both TX and RX, therefore, making different dimensions for TX and RX is not useful. The studied electrode dimensions are $3.5 \times 5.5\ \mathrm{cm}^2$, $4 \times 4\ \mathrm{cm}^2$, $3 \times 3\ \mathrm{cm}^2$ and $2 \times 2\ \mathrm{cm}^2$.

Coupler structure

As introduced in Sections 1.2 and 3.3, coupler can have either a vertical or a horizontal structure. Experimental measurements are carried out to find out the optimal structure of the electrodes with respect to the electrode dimension and the spacing between the electrode pair. Moreover, in the horizontal structure, the longitudinal and transversal electrodes orientation is examined for different combinations at the TX and RX.

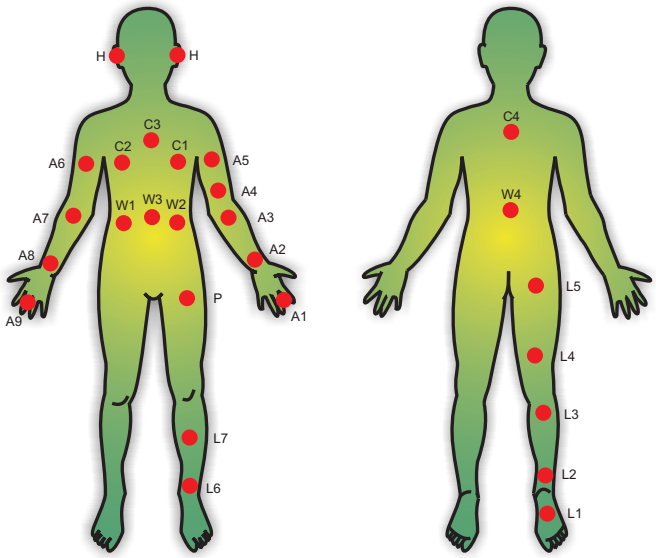

Fig. 4.1: Coupler locations on the human body.

Electrode pair spacing

The Influence of the electrode pair spacing is investigated employing couplers with different electrode pair separation. Based on the structure of the coupler, vertical or horizontal, the electrode pair spacing is filled in using different dielectrics see Fig. 3.4. In the vertical structure, the spacing between the electrode pair filled with PVC foam and/or PCB material is varied. The investigated values of this space are 2 cm, 1 cm, 0.5 cm and 0.2 cm. In the horizontal structure, the distance between the two electrodes filled with PCB material is varied from 4 cm to 2 cm and 1 cm.

Static and dynamic test conditions

Experimental tests need to be performed to examine the characteristics of BCC due to body movement —including sitting on a chair, standing, walking and moving an arm— employing couplers with various configurations and positioning them on different parts of the body. The analysis of the experimental results should provide a good understanding of how to model the variation in the BCC channel statistically.

Distance between the coupler and the human body

The BCC operation for the capacitively coupled on-body channel is based on near-field coupling. Therefore, electrodes can be placed on or close to the human body. Influence of on and off the body contact (clothes in between) of the TX and RX coupler is tested, since different applications may require on-body or off the body contact. In the off the body scenario, we test how the propagation loss varies as function of the distance of the couplers from the human body. This will enable us to understand the coupling behavior and the interference and noise influences, specifically for the application related to wearable electronic devices. Excluding this on, all other experiments are performed with couplers on the human body.

Different people with different body structure

In order to characterize the property of the body structure and to investigate its influence on BCC, similar experiments are performed with different subjects. By comparing the results from similar test scenarios with different test persons, the reproducibility of the measurements can be assessed. In this work, experiments are presented for two subjects. One test person is a female, height $= 1.54$ m and the other subject is a male, height $= 1.97$ m.

Different environments

Similar measurements are performed in various environments to examine the influence of external RF sources and devices on the main signal. For this test a conference room equipped with some chairs and a table and two glass walls, a lab room with lots of electronic equipments, a shielded (EMC) room are chosen as locations.

Interference Characteristics

As explained in Chapter 3, the frequency band of interest for BCC is from 100 kHz to 60 MHz. However, the considered frequency band is susceptible to all kinds of electromagnetic interference, as these bands can be used by different wireless systems, including AM/FM radio, TV broadcasting, amateur radio and different mobile applications, see [37]. Hence, it was considered important to obtain a better understanding of the influence of the interference, which might affect the BCC performance. To this end, experiments are performed in different environments and with different test subjects to study the influence of the interference on BCC. A conference room equipped with some chairs and a table and two glass walls, an office room equipped with some chairs and desks and PCs, a lab room with lots of electronic equipments, corridors and a pantry are the locations that have been selected to characterize the interference. In all of these locations, four different situations —above a table, near a PC monitor, near other measurement equipment and in the middle of the room— are compared to the situation where the probe is disconnected, thereby showing the lowest possible level that can be measured by the setup.

4.2.2 Performed Measurements

The possible combinations of the test parameters of the above discussed experiments are indicated in Table A.2. Only a subset of the presented measurement scenarios is studied in this work due to the limited time which was available to study the test cases. The subset is selected such that it allows conclusion about all of the parameters considered in Section 4.2.1.

To this end, the number of the coupler positions on the body is limited to seven, as shown in Fig. 4.2. All the tests have been performed in a conference room in Hightech Campus building 37, floor 5, room 5.021A. The room is 2.70×4.30 m^2, has two glass walls and does not contain electronic equipments. Most of the experiments are performed on the same subject, female, height $= 1.54$ m.

As explained before, in all the experiments the electrodes are on the body and are taped to the body in order to limit the movement during the measurements and to enable reproducibility. The influence of coupler separation from the body is tested in separate measurements.

To test the measurement reproducibility, some experiments are repeated on different days and also on another subject, male, height $= 1.97$ m. In a separate session, some experiments are performed in a shielded (EMC) room. The results obtained form these measurements are used to verify the measurement results in the conference room.

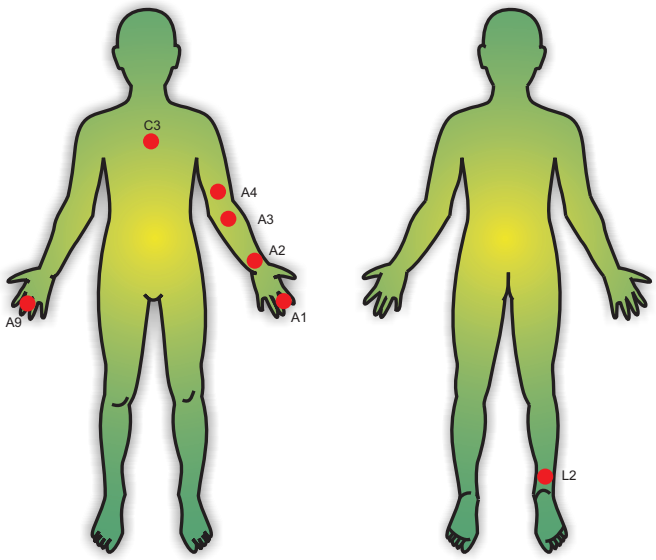

Fig. 4.2: Limited set of coupler locations on the human body, as considered in the remainder of this work.

Figure 4.3 depicts the measurement system connected to the test person for one of the test cases. It should be noted that for all the experiments the test person is standing almost in the middle of the conference room, far from all the chairs and the table. Vertical TX and RX couplers are applied in the experiments unless otherwise mentioned specifically.

To test the interference characteristics, the dedicated measurement setup explained in Section 3.6 and illustrated in Fig. 3.8 is used. All the measurements are performed employing a $4 \times 4\ \mathrm{cm}^2$ coupler with 1 cm electrode spacing. Note that the interference experiment is not indicated in

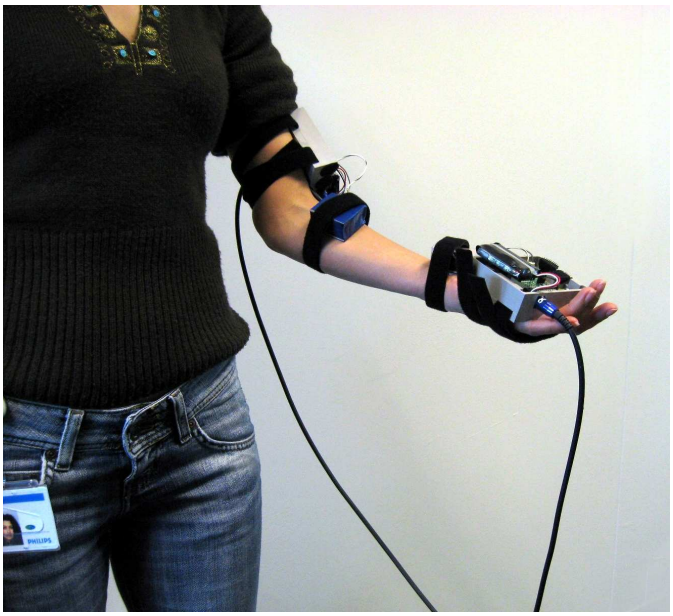

Fig. 4.3: Channel measurement system attached to the arm of the test person while standing.

table A.2. Four different test cases —above a table, near a PC monitor, near other measurements equipments and in the middle of the room— are compared to the lowest possible level that can be measured by the measurement setup.

4.3 Measurement Results

In the following, the results obtained from the measurements are presented. As described in Section 3.5, for the BCC channel characterization, the measured received power is translated into propagation loss between the TX and RX couplers using the results from the back-to-back calibration measurements. The behavior of the average signal attenuation for the frequency range of 100 kHz to 60 MHz is assessed to characterize the BCC transmission.

4.3.1 Measurement reproducibility

Maximum measurable level of signal attenuation

If the transmitted signal falls below the noise level in the system, data can no longer be detected at the RX. Therefore, it is required to measure the level of the noise in our measurement system. As explained in Section 3.5, since the measured RX signal is translated into propagation loss, we are interested in finding the maximum propagation loss that can occur. The maximum channel attenuation that the measurement system can characterize is measured by placing the TX and RX on the table in the conference room without attaching any coupler to them. So, the RX can receive only noise. This setup is depicted in Fig. 4.4. From this experiment it follows that the maximum level of propagation loss that can be measured by the measurement system equals 80 dB.

Experiments on different days

Experiments to examine the reproducibility of the measured data have been carried out by performing the same experiments on different days. The results for this test are depicted in Fig. 4.5 where both couplers are on the arm and a $4 \times 4\ \mathrm{cm}^2$ electrode size with 1 cm electrode separation is applied. The results show a typical deviation of less than 5 dB in the propagation

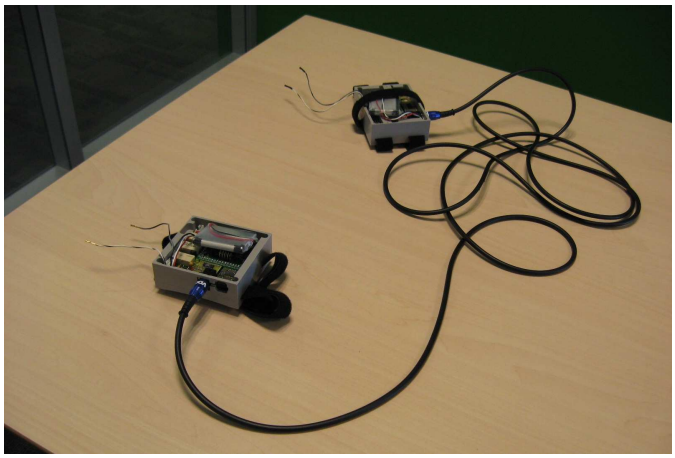

Fig. 4.4: Setup to measure the maximum level of signal attenuation of the measurement system.

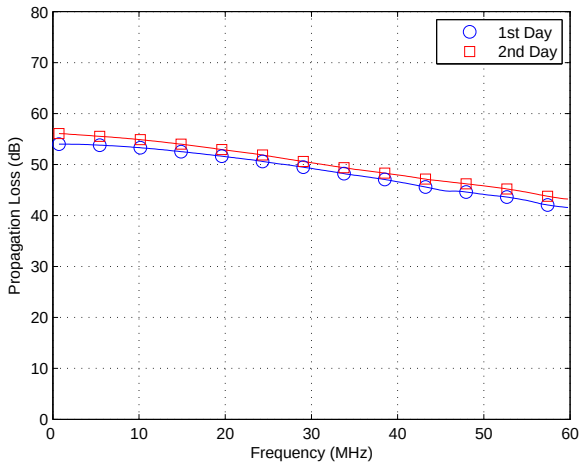

Fig. 4.5: Propagation loss as function of frequency on different days, for 4×4 cm^2 electrodes and 1 cm electrode spacing and the arm channel (A2A3).

loss, which verifies the reproducibility of the measurements. The results for other coupler sizes and configurations were similar.

4.3.2 Influence of the TX and RX coupler locations

This subsection studies the results of the experiments that have been performed to characterize the influence of the transceiver locations. Figure 4.6(a) depicts the characteristics of the propagation loss for combinations of different coupler locations on the body as illustrated in Fig. 4.2. For these measurements, 4×4 cm^2 couplers are applied with a electrodes spacing of 1 cm. As observed, for the couplers on the arm, the attenuation varies from 60 to 45 dB from lower to higher frequencies. For couplers on leg-arm (L2A2) or chest-leg (C3L2) channels there is an extra loss of 10 to 15 dB. However, the frequency behavior is similar.

It is concluded that the signal attenuation increases by increasing the distance between the locations of the TX and RX couplers on the body. However, the maximum observed propagation

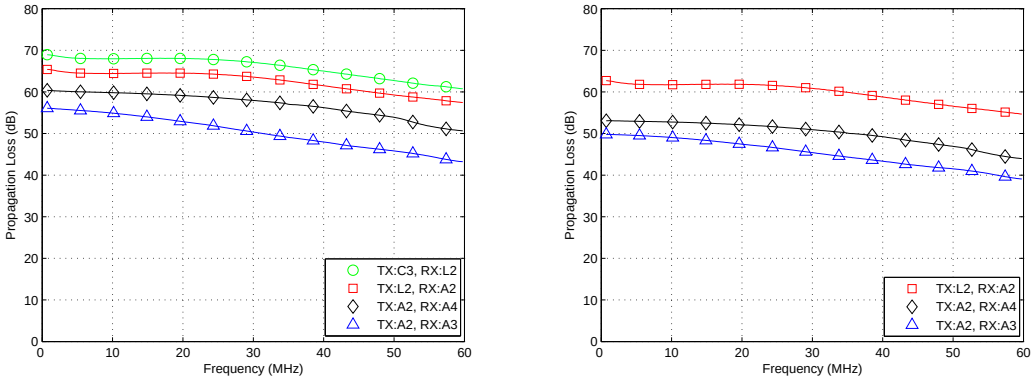

(a) 4×4 cm^2 and 1 cm electrode pair spacing.

(b) 3.5×5.5 cm^2 and 2 cm electrode pair spacing.

Fig. 4.6: Influence of transceiver locations on the propagation loss as function of frequency.

loss level for almost all the coupler locations is less than 80 dB. This verifies that even for large distances on the body a reasonable signal attenuation is achieved. Moreover, the results of chest-leg and leg-arm channels show that the couplers in the front and back of the body can communicate with each other with a reasonable propagation loss. Thus, this shows that the full body coverage is obtained in BCC.

The frequency behavior of the propagation loss can be explained as follows. The combination of the capacitors formed between the electrode pair and between the coupler and the human body determine the frequency behavior of the propagation loss. The values of these capacitors depend on the electrode dimensions, electrode pair spacing and the permittivity and conductivity of the dielectric materials between the electrode pair. They also highly depend on the permittivity and conductivity of human body tissues.

The permittivity and conductivity of a dielectric can be frequency dependent. This also applies to the human body tissues. The dielectric properties of various human tissues have been studied by authors of [38] for the frequency band of 10 Hz to 20 GHz. Their results show that the permittivity of the human body tissues reduces by increasing the frequency. Moreover, the conductivity of the human tissues increases by increasing the frequency. Consequently, the values of the mentioned capacitors will change by increasing frequency and their combined influence shows a high-pass like signal transfer for the whole body channel.

Similar results are obtained by applying the other couplers with different structures. Figure 4.6(b) shows the results for the coupler of $3.5 \times 5.5\ \mathrm{cm}^2$ with 2 cm electrode spacing, which verifies that the propagation loss increases by increasing the distance between the TX and RX (see also Appendix B.1).

As it can be observed from the results there is a little variation in mean propagation loss over frequency. Fig. 4.7 depicts the 255 measured data of the propagation loss and their mean for $4 \times 4\ \mathrm{cm}^2$ couplers with 1 cm electrode spacing and arm channel (A2A3). The results show that none of the 255 realizations of the propagation loss reveals frequency selectivity. Similar results are obtained for other locations and using other couplers. Hence, it can be concluded from the measured data that the BCC channel is essentially flat.

We observed that the frequency dispersion of the BCC channel is very limited. Hence, it

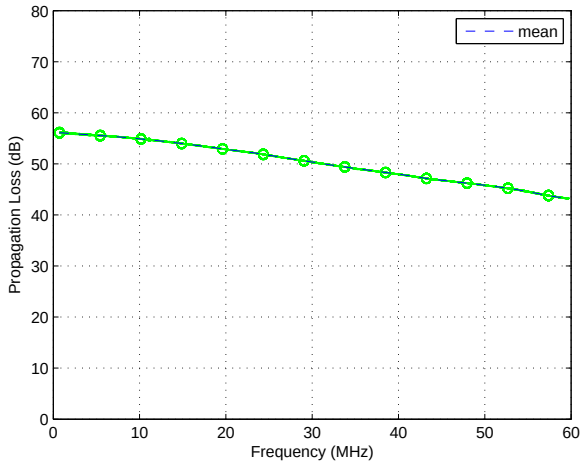

Fig. 4.7: Propagation loss as function of frequency, for 255 realizations together with their mean for $4 \times 4\ \mathrm{cm}^2$ electrodes and 1 cm electrode spacing and the arm channel (A2A3).

is not very beneficial to apply multi-carrier techniques such as orthogonal frequency division multiplexing (OFDM). Also the signal detection can be relatively simple, as the low frequency dispersion will allow for a very simple equalizer, even for large signal bandwidth of several tens of MHz. Consequently, BCC can result in a very simple communication solution and with a low power consumption, due to the much lower carrier frequency, compared to those of wireless (GHz) RF solutions.

As discussed in Chapter 2, similar results for the frequency behavior of the BCC channel have been reported in [14], [19], [20] and [35]. However, due to their proposed measurement systems, the channel behavior at low frequencies was influenced by the input impedance of the measurement equipment. Consequently, their final results are different from these reported here.

4.3.3 Influence of coupler configuration

The node form factor is an important factor in BCC system design. The size of the coupler will largely govern the size of the BCC node. This size is determined by the electrode dimensions and the spacing between the electrode pair forming a coupler. Knowledge of the influence of the coupler size on BCC gives information about the required transmit power and sensitivity of the receiver.

The following results show the measured propagation loss for the arm channel for different coupler configurations, including electrode dimension, electrode pair spacing and coupler structure. Similar results are obtained for other coupler location pairs (see Appendix B.1).

Influence of the electrode dimension

In this subsection, couplers with different dimensions are compared to find out how they affect the BCC propagation loss. Figure 4.8 depicts the propagation loss results. For the coupler of 3.5×5.5 cm^2, the attenuation varies from 50 to 40 dB from lower to higher frequencies. However, for the coupler of 2×2 cm^2, an extra loss of 10 dB is observed. We can conclude that the larger the dimensions of the electrode is, the lower the signal attenuation is achieved. In this test the experienced channel is the same for all the cases and the spacing of the electrode

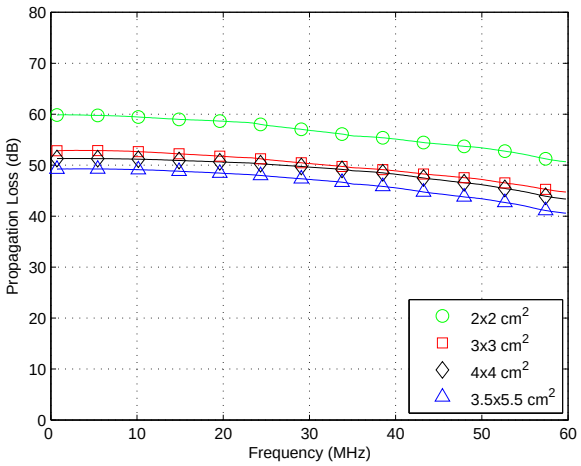

Fig. 4.8: Influence of electrode dimensions on the propagation loss as function of frequency, for 2 cm electrode spacing and the arm channel (A2A3).

pair in each coupler equals 2 cm, consequently, the only factor that has an influence on the propagation loss level is the electrode dimensions. The reduction in the propagation loss level can be explained by the fact that the capacitive coupling between the coupler and body is larger when the electrode dimensions are larger. Therefore, more electric field can be induced to the body.

Although the $3.5 \times 5.5\ \mathrm{cm}^2$ electrodes show superior performance, the size might be prohibitive for WBAN implementation. Thus, one needs to make a trade-off between the BCC envisioned application and performance. In this study, the $3 \times 3\ \mathrm{cm}^2$ electrode size forms a nice compromise between size and the resulting propagation loss. As seen in Chapter 2, concerning the influence of electrode size the same conclusions were reported in [7], [8], [10, 11], [18] reached the same conclusions .

Influence of electrode pair spacing

The influence of the electrode pair spacing has been studied by performing experiments with four different electrode pair spacings. Figure 4.9 depicts the results for these four separations applying $4 \times 4\ \mathrm{cm}^2$ electrodes. Overall, it is observed that a higher separation yields a lower attenuation, however, not over the whole frequency range. In this test, the experienced channel for all the cases is the arm channel and all the couplers have the same dimensions. Therefore, the results can only be influenced by the electrode spacing.

By increasing the electrode spacing, the impedance of the capacitor between electrode pair increases. Subsequently, it is expected that at TX a higher electric field is coupled to the body and at the RX a larger differential signal can be detected. However, as observed, the propagation loss at higher frequencies decreases more quickly for the 0.2 cm spacing than for the others. The results might get influenced by the differences in couplers construction. For the 0.2 cm separations only PCB material was present and for the other couplers the volume is filled in by PVC foam and PCB material, as illustrated in Fig. 3.4. These materials have different conductivity and permittivity at different frequencies thus the frequency behavior of the different coupler constructions is not the same.

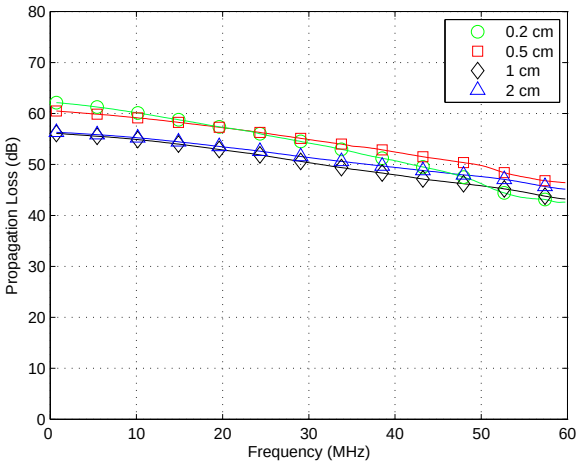

Fig. 4.9: Influence of electrode spacing on the propagation loss as function of frequency, for $4 \times 4\ \mathrm{cm}^2$ electrodes and the arm channel (A2A3).

Overall, in this study, the 2 cm separation yields less propagation loss and the best performance. Regarding the constraint in node size for WBAN applications, too high separation between electrode pair is impractical to choose. Thus, a 1 cm electrode separation is selected which yields a suitable tradeoff between the achieved propagation loss and coupler size. It is noted that in practical BCC nodes, the space between electrodes will be used to place the node electronics and one of the electrode will serve as the PCB ground plane. Consequently, 1 cm seems also reasonable in this view.

In a separate session, the spacing between the electrodes of two couplers of the same size is filled with different combinations of materials to investigate their impact on the propagation loss. For this test $3\times3\,\mathrm{cm}^2$ electrodes are selected. In one set, the space between the electrodes of both TX and RX is fully filled with PCB material and PVC foam. In the other set, the space is not fully filled: at two sides it is empty, so there is only air. These two electrode construction approaches and achieved results are shown in Figs. 4.10(a) and 4.10(b), left and right, respectively. As was expected, the average propagation loss for the fully filled case is 10 dB higher.

This can be explained as follows. Each coupler can be considered as three parallel capacitors, C_1, C_2 and C_3 as depicted in Fig. 4.11; in the fully filled case, these capacitors are equal ($C_1 = C_2 = C_3$). On the other hand, in the not fully filled case there are two equal capacitors with the permittivity of air as dielectric ($C_1 = C_3$) and one capacitor (C_2) with the PCB material and PVC foam permittivity. Since the air permittivity is less than the permittivity of the other materials, the equivalent capacitor between the electrode pair in the fully filled case is larger than in the not fully filled case. This property results in smaller impedance between electrode pair of fully filled case and thus results in a higher propagation loss. Therefore, this can be considered as an important factor in construction of couplers.

In all of the studies reported in this thesis, the electrode spacing for the vertical structure is fully filled with PVC foam and/or PCB material. So, in practical cases, where the room between the electrodes will be used to place the electronics and the rest is air, the level of propagation loss will be even lower than what is reported in this work. Therefore, this will have impact on the transmit power and the sensitivity of the receiver that the system designer should be aware of. The considered scenario in this work can consequently be a worst case scenario.

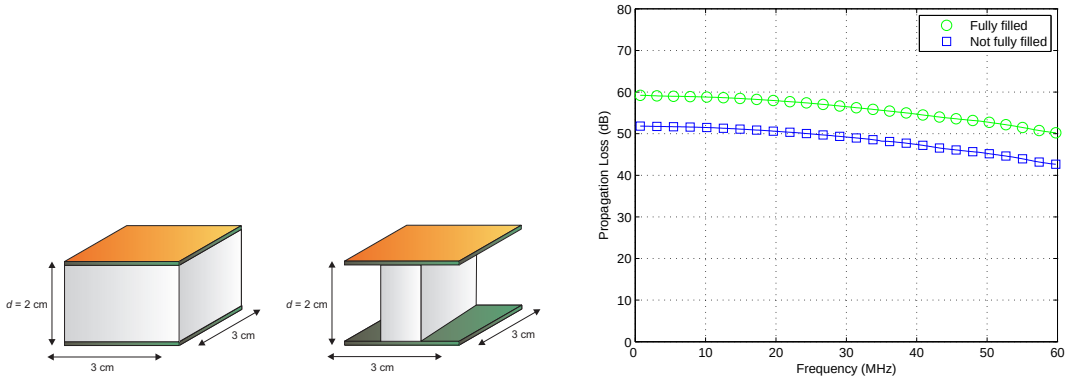

(a) Coupler constructions.

(b) Propagation loss as function of frequency.

Fig. 4.10: Influence of coupler construction on the propagation loss as function of frequency for $3 \times 3\ \mathrm{cm}^2$ electrodes and 2 cm electrode spacing.

(a) Spacing between electrode pair is fully filled. (b) Spacing between electrode pair is not fully filled.

Fig. 4.11: Schematic of the capacitors formed between the electrode pair for the couplers with two different constructions.

Comparison of combinations of couplers with different structures

In order to compare the performance of the vertical structure to that of the horizontal structure, first the transversal and longitudinal orientation of the horizontal structure are examined. Then the one with the best performance, i.e. the lowest propagation loss, is compared to the vertical structure.

Figure 4.12 depicts the propagation loss results for different combinations of horizontal orientations for the 2×2 cm^2 electrodes with 1 cm electrode separation. We recall that there are two orientations, i.e. the longitudinal and the transversal introduced in Section 1.2. It can be concluded that the lowest propagation loss is achieved by applying a longitudinal orientation for both the TX and RX side. Moreover, the propagation loss is almost equal to the noise level of the measurement system for this electrode dimension and separation when the RX has transversal orientation. The reason is that for longitudinal orientation, the direction of the electric field between the electrode pair is along the arm channel, which is most effective for the transmission from TX to RX. For the transversal orientation, the electric field direction is formed on the upper side of the arm and is not along the arm channel.

As we discussed in Chapter 2, this experiment was also carried out by the authors of [10, 12]. They also reported that the longitudinal orientation gives a better results.

Exploiting the results obtained from the previous experiments, the performance of different

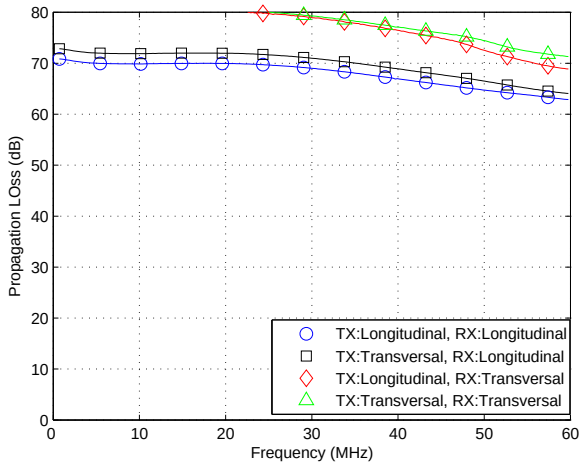

Fig. 4.12: Influence of orientation of the horizontal coupler on propagation loss as function of frequency for 2×2 cm^2 electrodes and 1 cm electrode pair on the arm channel (A2A3).

combinations of TX and RX electrodes structures are compared. The comparison result is shown in Fig. 4.13. For these measurements, the vertical coupler is 4×4 cm^2 with 1 cm electrode spacing and the horizontal coupler is 2×2 cm^2 electrode pair with 4 cm separation and longitudinal orientation. Both TX and RX are positioned on the arm channel (A2A3). The lowest propagation loss results are obtained when vertical coupler are used at the RX. The difference in frequency behavior is due to the different dielectric materials used between the electrode pairs. PCB material is used between the electrode pair in the horizontal structure, while the spacing of the electrode pair in the vertical structure is filled with a combination of PCB material and PVC foam, as explained in Section 3.3. The RX, which shows the lowest propagation loss for a vertical coupler, plays an important role in signal reception. Since each node in BCC can act as both TX and RX, it is reasonable to use the vertical coupler as the coupler structure for BCC transceivers.

In the study by authors of [14], [15] and [18], discussed in Chapter 2, it was also shown that the vertical electrode structure yields a superior performance compared to using the horizontal structure.

4.3.4 Influence of body motion

Tests are performed to assess the influence of the orientation and movement of the human body on the propagation loss. The body movement study, as shown in Fig. 4.14, is limited to two different movements: (i) walking in the room and (ii) standing in the middle of the room while moving the arm. Figure 4.15 depicts the measurements results for the test cases when the test person was sitting on a chair, standing, walking and moving the arm. The applied coupler size was 4×4 cm^2 and the electrode separation was 1 cm. Overall, the average signal attenuation in the dynamic scenarios is in the same level as static-standing scenarios. However, for the sitting scenario, an extra 10-12 dB channel attenuation is observed compared to the standing case. This is most likely due to coupling interaction with the chair. Other couplers with different configuration yield similar results for the same location on the body (see Appendix B.1).

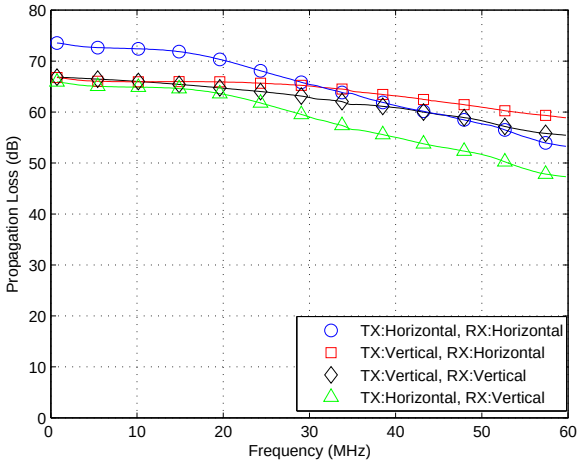

Fig. 4.13: Influence of coupler structure on propagation loss as function of frequency, for 4×4 cm^2 with 1 cm electrode pair spacing and vertically structured and 2×2 cm^2 electrode pair with 4 cm separation horizontally structured and the arm channel (A2A3).

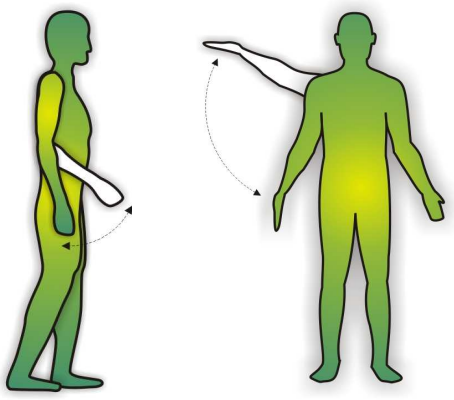

(a) Walking (b) Moving arm

Fig. 4.14: Schematic illustration of the two studied body movement.

The deviation from the mean propagation loss, as depicted in Fig. 4.16, is higher for a moving arm and walking than for sitting on a chair and standing. This variation occurs due to different coupling between the couplers and the body during movement. For instance, in the moving arm scenario, first the couplers interact with each other via the arm and the side of the body. By moving the arm, the coupling through the side of the body gets weaker, up to the point that the couplers interact only via the arm. This results in a higher propagation loss. This variation in coupling between coupler and different parts of the body occurs more frequently for the walking scenario. Therefore, as observed, the standard deviation of the walking scenario is 1 dB higher than for moving the arm. The achieved standard deviation for similar movement and on other positions on the body is less than 3 dB (see Appendix B.1).

Thus, from the body movement results, it is concluded that the signal level variability due to the body movement is very limited for BCC. Compared to similar studies for RF-based WBANs,

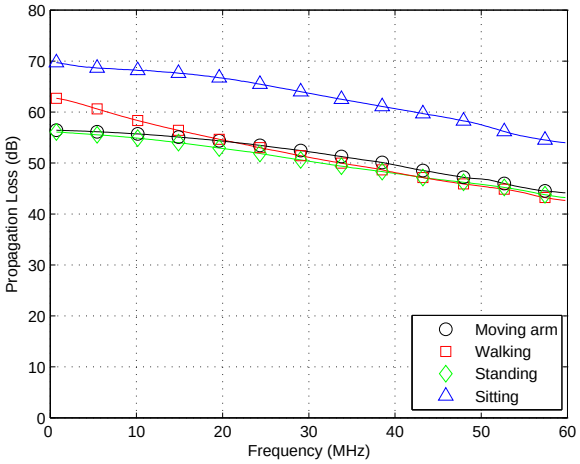

Fig. 4.15: Influence of body movement on propagation loss as function of frequency: sitting on a chair, standing, walking, moving arm for 4×4 cm^2 electrode dimension and 1 cm electrode pair spacing and arm channel (A2A3).

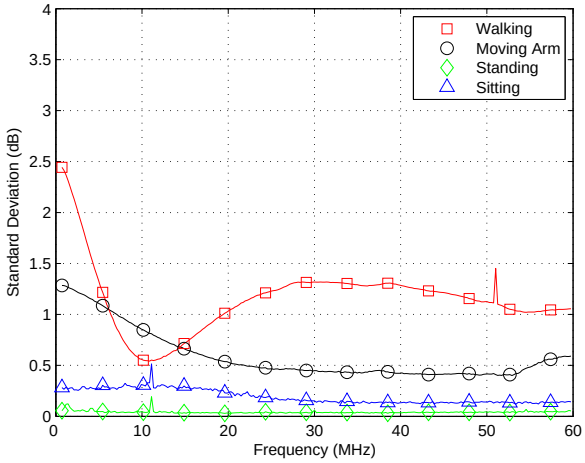

Fig. 4.16: Influence of body movement on the standard deviation of propagation loss as function of frequency: sitting on a chair, standing, walking, moving arm for 4×4 cm^2 electrodes and 1 cm electrode spacing on the arm channel (A2A3).

see e.g. [5], the standard deviation obtained by BCC approach is relatively low. For the RF-based WBANs systems, the body shadowing does create a large channel variability due to the body movement, i.e. in the range of 30 to 40 dB. This poses a serious challenge for RF transceivers design, but not for BCC receivers.

As reported by the authors of [24–27], in Chapter 2, the standard deviation of the signal is higher due to the body movement. However, their results were limited by the "ground scenario".

The distribution of the variation in propagation due to the body movement is studied further in Section 5.3.

4.3.5 Influence of arm channel orientation and coupler placing

Some experiments have been performed to investigate the influence of body channel orientation on the propagation loss. It is also investigated how the couplers interact with each other for practical situations in which a person might touch the coupler. The results of these measurements are presented in the following.

Arm orientation

The results depicted in Fig. 4.17 are for three different arm orientations where the TX and RX couplers are located on the subject's arm, the electrode dimensions are 4×4 cm^2 and the electrode separation is 1 cm. These three arm orientations —under arm pointing forward, arm oriented towards the body and arm oriented away from the body— are shown in Fig. 4.18 and named ArmOrn-I, ArmOrn-II and ArmOrn-III, respectively.

Overall, the average propagation loss is the lowest for the case that the arm is oriented towards the body. This can be explained by the fact that increased coupling occurs both through the arm and through the body. For the other two cases couplers mainly interact with each other via the arm.

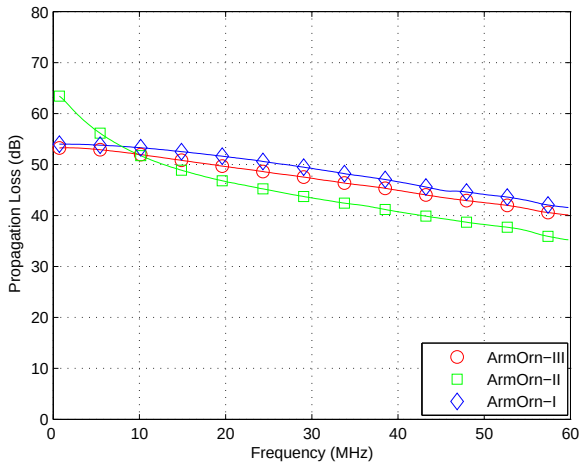

Fig. 4.17: Influence of arm orientation on propagation loss as function of frequency for $4 \times 4\ \mathrm{cm}^2$ electrodes and 1 cm electrode spacing on the arm channel (A2A4).

Coupler placing

Three different placing for the TX and RX couplers are considered to assess the impact of the couplers' placing on the BCC transmission behavior. The main goal for this experiment is to understand how propagation loss is affected by touching the couplers in these three different locations. The locations are depicted in Fig. 4.19, where in the first case the couplers are on the table and are touched by subject two hands, in the second case the subject holds the couplers above the table while standing near the table. In the third case, the subject is far from the table while holding the couplers. These measurements are compared to the case where the TX and RX are on the table without being touched.

The results obtained from these experiments are shown in Fig. 4.20 for the $3.5 \times 5.5\ \mathrm{cm}^2$ electrodes, where the electrode pair separation equals 2 cm and the TX and RX are located on A1 and A9 on the body, respectively. The propagation loss behavior in the case that the couplers are on or above the table differs from the case that the couplers are on the body and far from

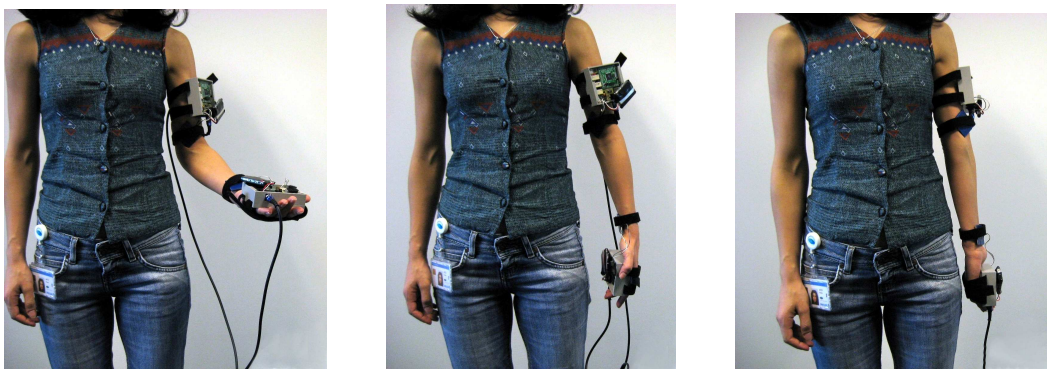

(a) Under arm sticking forward, ArmOrn-I.

(b) Arm oriented towards the body, ArmOrn-II.

(c) Arm oriented away from the body, ArmOrn-III.

Fig. 4.18: Measurement setup to test the influence of arm orientation on the propagation loss.

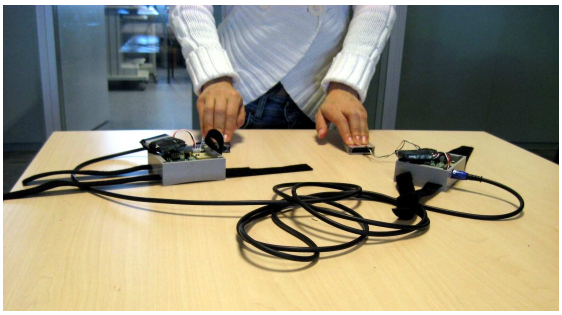

(a) Couplers are on the table and are touched by subject's two hands.

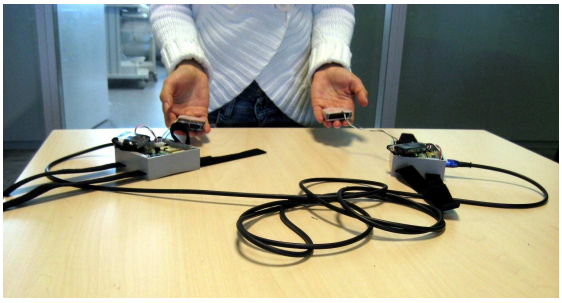

(b) Couplers are held above a table by subject.

(c) Couplers are held far from furniture by subject.

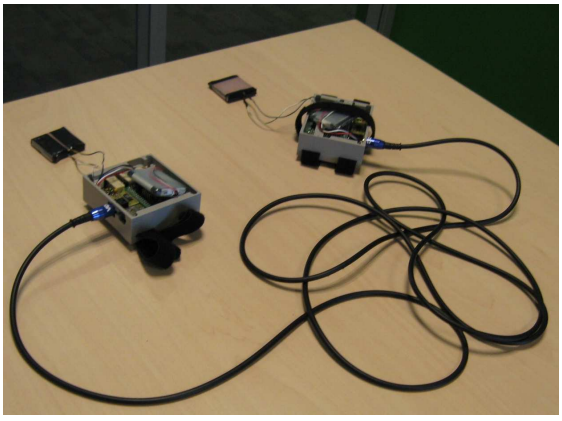

(d) Couplers are on a table without body contact.

Fig. 4.19: Measurement setup to test the influence of coupler placing on propagation loss.

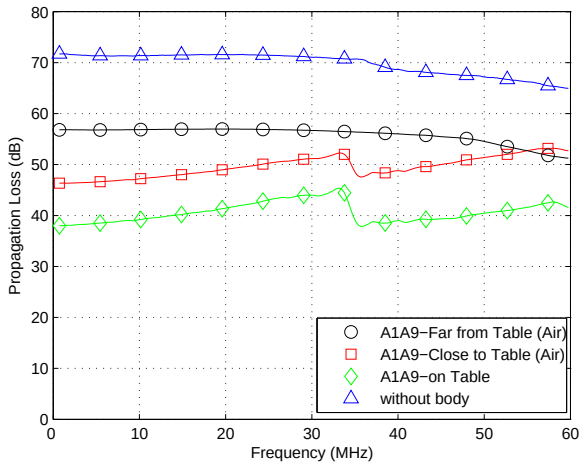

Fig. 4.20: Influence of coupler placing on propagation loss as function of frequency, for $3.5 \times 5.5\ \mathrm{cm}^2$ electrodes and 1 cm electrode spacing and the A1A9 channel.

the table. It is also observed that the level of attenuation is 10-20 dB less for frequencies below 35 MHz and up to 10 dB less for frequencies above 35 MHz. This can be explained by the fact that the formed capacitor not only depends on the permittivity and conductivity of the human body and the dielectric between electrode pair, but also gets influenced by the characteristics of the table which is made of wood with metal base. Thus, different frequency behavior and less propagation loss level are observed for cases near the table. For the case that there are only couplers on the table, still the attenuation is much higher. This occurs because couplers directly interact with each other due to their short distance.

As a conclusion, touching the couplers when they are not on the body results in different channel behavior and different propagation loss. Therefore, this will have a serious impact on the system performance and it should be considered as a key parameter in system design.

4.3.6 Influence of the couplers off the body and on the body

One of the key characteristics of using the human body as a transmission medium is that the communication is limited to on, or to very close vicinity of, the human body. This characteristic is very favorable compared to the RF-based WBANs solutions, since our BAN will experience no interference from other BANs. The system set up in order to find out the communication range of BCC is shown in Fig. 4.21.

To examine the characteristics of body communication off the body, the arm of the subject is placed at different distances from the couplers. Figure 4.22 illustrates propagation loss measurement results for the $4 \times 4\ \mathrm{cm}^2$ electrodes with 1 cm separation, where the two couplers are separated 11 cm from each other on a cardboard box. The bottom and top curves represent the case of the arm touching both couplers and the case of no arm present, respectively. This results in a 25 dB loss difference between the two cases. When the arm is placed 1 or 2 cm from the electrodes, an increase of 7-14 and 14-22 dB, respectively, is observed compared to the touching case. When the arm is 4 cm above the couplers, the attenuation is about equal to the case without an arm touching the couplers. The remaining interaction for these cases is probably mainly due to direct coupling between the TX and RX couplers, caused by the relatively small distance between them.

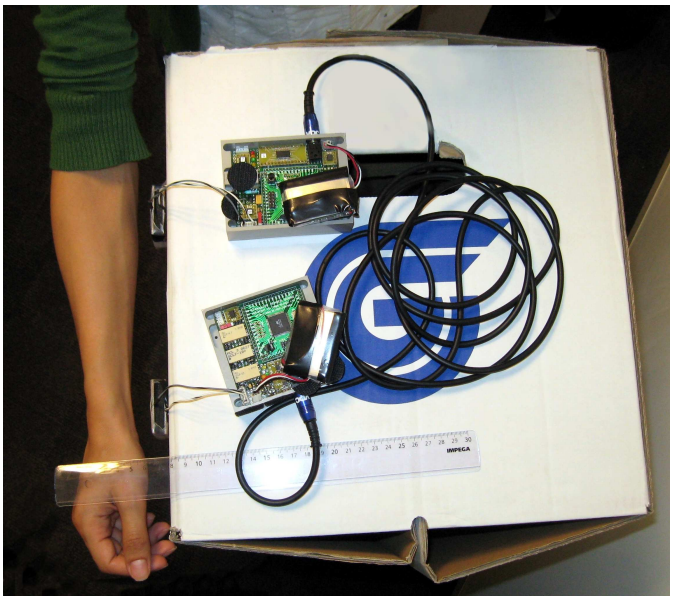

Fig. 4.21: Top view of measurement setup to assess the influence of body separation on propagation loss. The couplers are placed 11 cm apart and the distance of the arm to the couplers is varied.

By comparing the results of on the body and off the body it is shown that by placing the couplers on the body (the majority of) the transmitted signal travels through the body. Furthermore, it is concluded from these results that the propagation loss off the body is much higher than that close to the body. Hence, the communication range is indeed limited to the vicinity of the body. This is in contrast to results found for RF solutions where the communication range is typically governed by free space separation. Consequently, the communication range of these RF systems can be several meters from the body, which will likely result in interference between different WBANs. This property results in a frequency reuse factor of close to 1 for BCC, i.e.

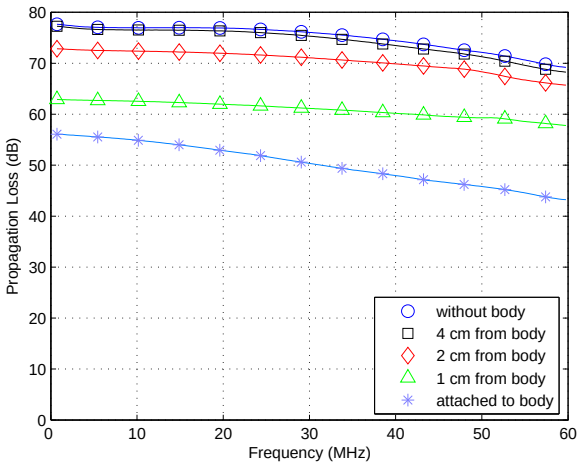

Fig. 4.22: Influence of body-coupler separation on the propagation loss as function of frequency, for $4 \times 4\ \mathrm{cm}^2$ electrodes and 1 cm electrode spacing.

every WBAN can use the same frequency band.

4.3.7 Verification

To verify the results achieved from the experiments, some measurements are repeated to test the results on another subject body and in a shielded (EMC) room.

Different subjects

Figure 4.23 depicts the results performed on a different subject (male, height $= 1.97$ m) for the leg-arm (L2A2) channel with $4 \times 4\ \mathrm{cm}^2$ electrodes, where the electrode separation equals 1 cm. The behavior of the propagation loss is similar to the results achieved for the other test person, female, height 1.54 m. An additional 5 dB is likely due to the difference between the length of the two subjects results in an increased distance between the TX and RX. As we observed in our previous results, the larger the distance between TX and RX, the higher the signal attenuation. Similar differences were observed for other measurements for these two subjects. It can be concluded from this experiment that variation in propagation loss between different subjects is limited. However, more experiments are required to be carried out on more subjects with different body structures to draw firm conclusion here.

EMC room

Calibration and verification tests were performed in an EMC room. Figure 4.24 shows the most important results. The result of the back-to-back calibration experiment, as depicted in Fig. 4.24(a), verifies our result of characteristics of the TX output power. Moreover, as shown in Figs. 4.24(b), 4.24(c) and 4.24(d), the BCC fundamental properties that we drew from the measurements in the conference room are confirmed. However, the propagation loss values achieved from the measurements in the EMC room are not equal to the results achieved in the conference room. As discussed in Section 3.2, this likely is due to our measurement system

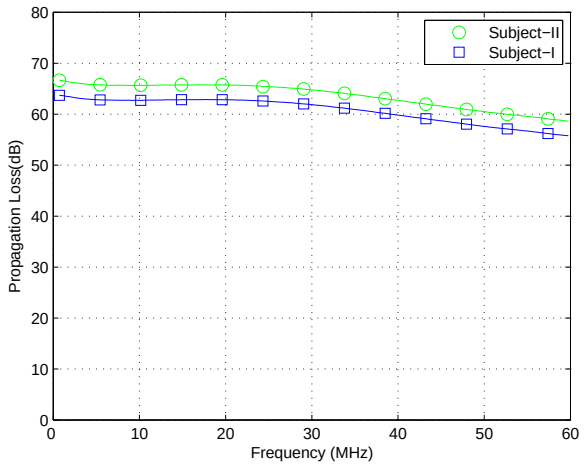

Fig. 4.23: Propagation loss as function of frequency for two different subjects, for the $4 \times 4\ \mathrm{cm}^2$ electrodes and 1 cm electrode spacing on the leg-arm channel (L2A2).

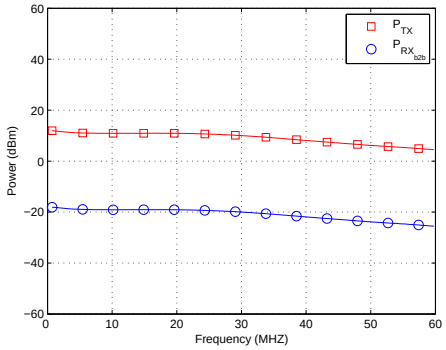

(a) Calibration results: measured received power and calculated transmit power from back-to-back setup.

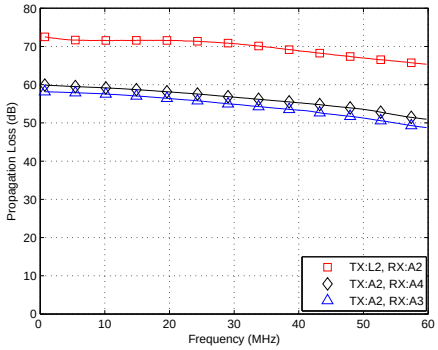

(b) Influence of transceiver locations on the propagation loss as function of frequency for $4 \times 4\ \mathrm{cm}^2$ and 2 cm electrode pair spacing.

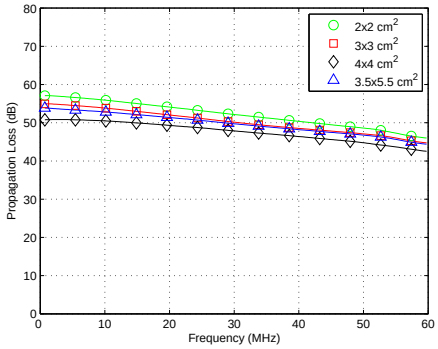

(c) Influence of electrode dimension on the propagation loss as function of frequency, for 2 cm electrode pair spacing and the arm channel (A2A3).

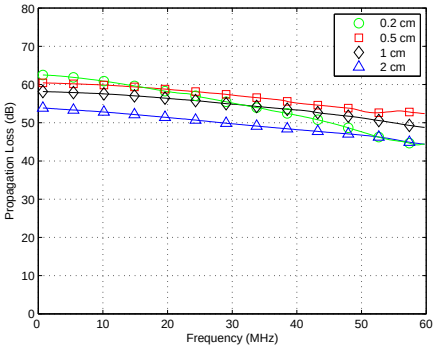

(d) Influence of electrode size on the propagation loss as function of frequency, for $4 \times 4\ \mathrm{cm}^2$ electrode dimension and the arm channel (A2A3).

Fig. 4.24: Verification results for the back-to-back calibration, TX and RX coupler locations, electrode dimensions and electrode pair spacing in the EMC room.

architecture. Since at the RX the power at each frequency is integrated at the whole band of the selected filter, it shows a lower propagation loss.

4.3.8 Interference measurement results

The interference from other RF sources and electronic equipments might affect the performance of BCC systems. Therefore, experiments have been performed to characterize the interference and examine its influence on BCC. Figure 4.25 shows the measurement results for four different test cases, as discussed in Section 4.2, in the lab room, in Hightech Campus 37, floor 5, room 5.024.

The bottom curve depicts the result when the probe is not connected to the spectrum analyzer, showing the lowest possible level that can be measured. It is observed that when the subject is located in the middle of the room, the interference is almost equal to the baseline. However, when the subject is near a monitor or other measurement equipment, or when the subject places the arm above a table with metal base, the interference severely increases. This can be explained by coupling of these devices to the body and to the coupler and the low frequency

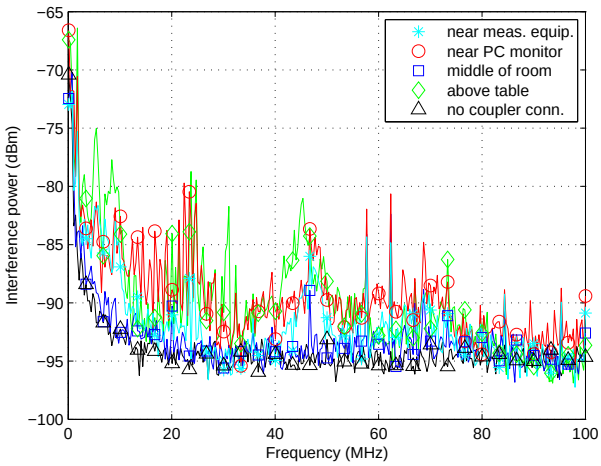

Fig. 4.25: Measured interference power for different measurements locations in the lab room.

interference they induce. The table acts as "antenna" for sources of interference and in turn couples this to the electrode and body. This subsequently results in higher interference. It was found in Section 4.3, however, that the desired signal also increases when the arm is placed above such a table, making the final impact lower.

More measurements have been performed in some other locations. The interference characterization is examined by carrying out test cases similar to the ones in the lab room. Figures 4.26(a) and 4.26(c) illustrate these results. As can be observed, the results are similar to the results of the lab room, although in the case of the pantry more variation in spectral properties of interference power is present. Based on these results and measurements results in other locations, such as the conference room and the corridor (see Appendix B.3), it is concluded that BCC is susceptible to interference. The integrated power of interference is in the order of –60 dBm, which is considerable. Moreover, the spectral characteristics of the interference signal power are very location dependent and its spectral properties vary a lot within each case.

The interference measurements in Fig. 4.26(b) show the results in the office room, but on another subject. From these results and some other experiments on other subjects (see Appendix B.3), it is concluded that the measured interference experienced by different subjects is almost similar.

As discussed in Section 3.6, the low frequency behavior of the measured interference is mainly limited by the phase noise behavior of the spectrum analyzer. Therefore, to characterize the interference in these frequencies, some other experiments have been performed. Figure 4.26(d) depicts the results performed in the lab room for frequencies below 2 MHz. As we can observe, even for the case that the subject is standing in the middle of the lab room, the level of interference is much higher at low frequencies. It is concluded from these results that the BCC channel is specially affected by interference at lower frequencies.

Due to the varying spectral properties of the interference, and since the characteristics of the interference are location dependent, the BCC channel is susceptible to interference. Therefore, the BCC system has to be designed in such a way that the experienced interference is suppressed. Subsequently, it would be beneficial to apply some adaptivity in the BCC data modulation scheme, specifically when a wideband system is applied. In that case, the system can choose the transmission mode that is least impacted by the locally experienced interference.

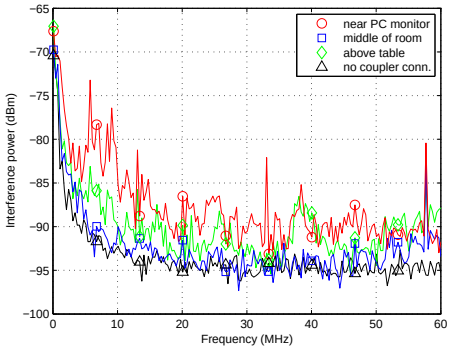

(a) In the office room.

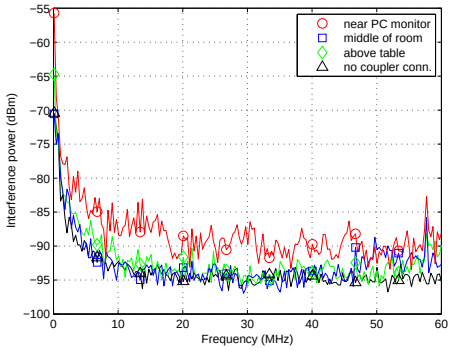

(b) In the office room another subject.

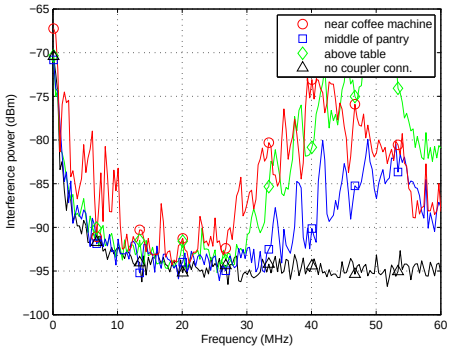

(c) In the pantry.

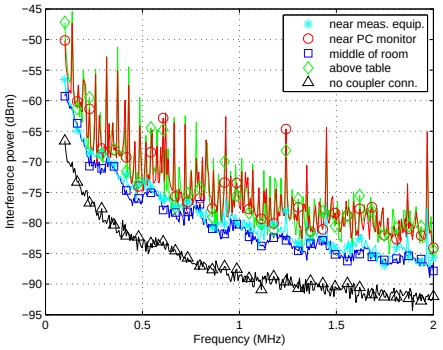

(d) In the lab room for frequencies below 2 MHz.

Fig. 4.26: Measured interference power for different measurements locations.

This is the subject of Chapter 6.

4.4 Summary and discussion

In this chapter, the propagation loss of capacitive BCC channel was investigated as function of frequency, for the band from 100 kHz to 60 MHz. Extensive measurements have been performed to examine the influence of the TX and RX coupler locations on the body, coupler size and structure, body movement and interference on BCC propagation loss.

It was observed that the BCC channel has a high-pass frequency behavior. The frequency dispersion of the channel is very limited compared to the RF-based WBANs. It was also observed that by increasing the distance between the transceivers on the body, the propagation loss increases. For almost all the node locations, however, the level of propagation loss is well below 80 dB.

From the study of the optimal structure and size of the coupler for BCC, it was concluded that the vertical structure performs superior to the horizontal structure. Also, increasing the size of the coupler, i.e. the electrode dimensions and the spacing of the electrode pair, decreases the propagation loss. Moreover, it was concluded that 3×3 cm^2 electrodes with 1 cm spacing achieve a nice tradeoff between propagation loss and the size of the coupler.

Body movement were shown to result in a very small variation in channel attenuation, i.e. the maximum observed standard deviation was less than 3 dB. Consequently, because of the

much lower frequency, the lower channel dispersion and the much lower fading due to the body movement, BCC can result in a much simpler and more robust communication solution with a lower power consumption than the traditional RF-based WBANs.

The BCC communication range was shown to be limited to the very close vicinity of the human body. This means that there is no co-channel interference between different BANs and this allows the whole frequency band to be reused by each WBAN. However, interference measurements showed that capacitive coupling is susceptible to interference from other RF and electronic systems. It was observed that the spectral properties of the interference vary and are time but mostly location dependent. For different subjects standing at the same location, the measured interference was very similar. Therefore, since the spectral properties of the interference is very time and location dependent, it would be favorable to apply some adaptivity in the BCC system design to minimize the influence of the interference, especially when a wideband system would be applied. Most of the results were confirmed by verification experiments reasonably stroke with earlier investigations.

Chapter 5

Channel Modeling

5.1 Introduction

The experimental study of the propagation loss in Chapter 4 provided us with an understanding of the behavior of the capacitive coupled on-body channel and its impact on the system design. In order to improve our understanding of the BCC channel behavior and to better understand the nature of motion-caused signal amplitude variation, it is required to model the on-body channel behavior based on our experimental results. The developed models also allow us to simulate the impact of the channel behavior on the BCC system performance.

In this chapter, experimental results are used to develop models to describe the average propagation loss in static body situations and for the variation due to body movement. In Section 5.2, the model for propagation loss characteristics in static situations is introduced. Section 5.3 discusses how to model attenuation variation due to movement of the body. This chapter ends with the summary and discussions of the results in Section 5.4.

5.2 Mean Propagation Loss Modeling

An empirical approach is used to model the measured attenuation based on the characteristics introduced in Chapter 4. Based on our study, it is observed that the average propagation loss decreases for higher frequencies and the attenuation is highly dependent on the coupler dimensions and the spacing between the electrodes. Moreover, the propagation loss increases as the distance between the TX and RX increases.

Figure 5.1 depicts the mean propagation loss results for the measurements with the coupler of size $4 \times 4\,\mathrm{cm}^2$ and 1 cm electrodes separation for different locations on the body. By having a closer look at the their frequency behavior, it is observed that a constant behavior and a linearly decreasing behavior occur. The frequency at which the constant behavior changes is called corner frequency, f_c. Especially for larger distances (e.g. C3L2) the difference between these two behaviors is apparent. Studying the other results with other couplers and with the other configurations, as depicted in Fig. 5.2, similar frequency behavior for the propagation loss can be observed. These investigations allow us to develop a general model for the mean propagation loss in dB, $L_\mathrm{p}(f)$, having the form

$$L_\mathrm{p}(f) = \begin{cases} A, & f < f_\mathrm{c} \\ A + B(f - f_\mathrm{c}), & f \geq f_\mathrm{c} \end{cases} \tag{5.1}$$

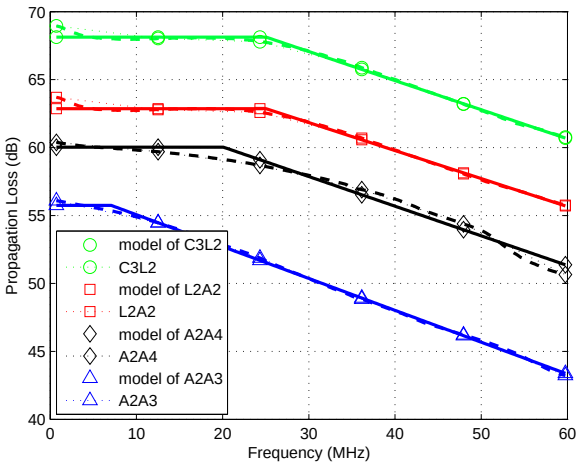

Fig. 5.1: Propagation loss as function of frequency and the empirical model for different locations on the body, for the 4×4 cm^2 electrodes dimension and 1 cm electrode pair spacing.

with f in MHz. The parameter A represents a fixed propagation loss and the parameter B shows the slope of the linear equation.

The parameters A, B and f_c are obtained as follows. First, parameter f_c is extracted from the graph by selecting the frequency at which the propagation loss frequency behavior changes. Next, the measured data for the band of f_c to 60 MHz which shows a linear decreasing is extracted. We use a polynomial interpolation approach to find a polynomial which fits to these sets of data in a least squares sense. This gives us the parameter B. By substituting f_c in the results of polynomial, the parameter A is calculated.

The empirical models for different locations on the body are illustrated in Fig. 5.1. Figures 5.2(a) and 5.2(b) depict the empirical models for the different electrode dimension and different electrode pair spacing, respectively. Tables 5.1, 5.2 and 5.3 present the numerical values achieved for f_c, A and B for all the results depicted in Figs. 5.1, 5.2(a) and 5.2(b), respectively.

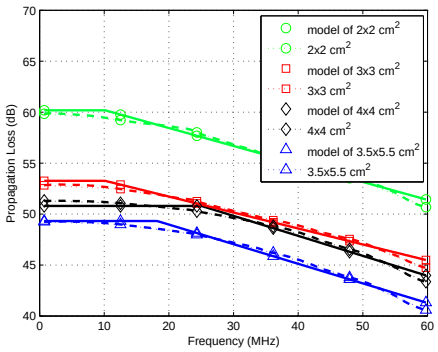

(a) Different electrode dimensions, for 2 cm electrode spacing.

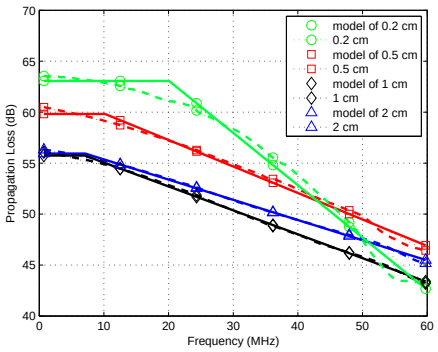

(b) Different electrode spacings, for 4×4 cm^2 electrodes.

Fig. 5.2: Propagation loss as function of frequency and the empirical model for different electrode dimensions and different electrode spacings, for the arm channel (A2A3).

Table 5.1: Best fit f_c, A and B for different location on the body, for $4 \times 4\ \mathrm{cm}^2$ electrodes and 1 cm electrode spacing.

	f_c	A	B
A2A3	7 MHz	55.5719	–0.23458
A2A4	22 MHz	60.0317	–0.21818
L2A2	25 MHz	62.8565	–0.20606
C3L2	25 MHz	68.1285	–0.21408

Table 5.2: Best fit f_c, A and B for different electrodes dimensions, for 2 cm electrode spacing and the arm channel (A2A3).

	f_c	A	B
$\mathbf{3.5} \times \mathbf{5.5}\ \mathrm{cm}^2$	18 MHz	49.3206	–0.1924
$\mathbf{4} \times \mathbf{4}\ \mathrm{cm}^2$	25 MHz	50.8002	–0.1965
$\mathbf{3} \times \mathbf{3}\ \mathrm{cm}^2$	10 MHz	53.28	–0.1565
$\mathbf{2} \times \mathbf{2}\ \mathrm{cm}^2$	10 MHz	60.1825	–0.17634

Table 5.3: Best fit f_c, A and B for different electrodes spacings, for $4 \times 4\ \mathrm{cm}^2$ electrodes and the arm channel (A2A3).

	f_c	A	B
$\mathbf{2}\ \mathrm{cm}$	7 MHz	55.9427	–0.1993
$\mathbf{1}\ \mathrm{cm}$	7 MHz	55.7419	–0.2346
$\mathbf{0.5}\ \mathrm{cm}$	10 MHz	59.8279	–0.2599
$\mathbf{0.2}\ \mathrm{cm}$	20 MHz	63.0598	–0.5135

As shown in the table, the parameter A is between 50 to 70 dB and its value mainly determined by the location of the transceivers on the body, the electrode dimension and the electrode pair spacing. The parameter B has almost the same value, i.e. around –0.2 for all the developed models other than the case of 0.2 cm electrode pair spacing, for which B equals –0.5. As discussed in Section 4.3.3, the construction of this coupler is different from the other couplers since the electrode pair spacing is filled only with PCB material. PCB material has different permittivity and conductivity properties and shows different frequency behavior. The similar value of the parameter B for the other cases can likely be explained by the fact that the dielectric used between the coupler has the same material and all the test cases have been carried out on the same subject. The parameter f_c changes between 7 to 25 MHz and its value depends on the coupler size and its location on the human body. It is also determined by properties of the human tissue and coupler dielectric.

More propagation studies need to be carried out to find the influence of environments and subjects with different body structures on the propagation loss. In addition, the effect of body locations and coupler positions needs to be investigated more, so that the model can be extended to include these variables as well.

5.3 Body Motion Fading Modeling

In this section, the influence of body movement is studied to understand the variation in signal attenuation when a person moves. The propagation loss fluctuations around the median due to the body motion (walking through the room and standing while moving the right hand up and down, as depicted in Fig. 4.14) are compared with the propagation loss fluctuation around the median for a static body (sitting on a chair and standing).

Figure 5.3 depicts the empirical cumulative distribution function (ECDF) of the propagation loss deviation (in dB) from the median per frequency, aggregated over the whole frequency range from 100 kHz to 60 MHz for the measured data shown in Fig. 4.15. For sitting and standing the standard deviation is very small, i.e. below 0.2 dB. For the moving arm and standing scenario, the standard deviations are equal to 0.6 dB and 1.14 dB, respectively.

For the other configurations similar results have been obtained. It can be concluded that the standard deviation of the propagation loss for the static scenarios is much smaller than for the dynamic scenarios. The maximum observed standard deviation was less than 3 dB and occurred for the two following cases.

For the walking scenario for the coupler size $3.5 \times 5.5\ \mathrm{cm}^2$ with 2 cm separation, where both couplers have been placed on the arm, the standard deviation was around 2 dB. This is because during the walking the arm of the test person naturally moves forward and backward, so the couplers experience varying coupling. Moreover, the dimension of the electrodes is larger than the other couplers. Consequently, the coupler experiences larger variations.

It is also observed that the standard deviation is around 2.5 dB for the test scenario in which the TX and RX are moving relatively to each other. In this test case, the subject is holding the couplers such that the TX and RX are on A1 and A9 position, respectively, see Fig. 4.2. In the previous case, the locations of the TX and RX were constant relative to each other. However, in this case, not only the couplers experience different coupling, but also the received signal varies due to the variation in the distance between the TX and RX. Consequently, this results in larger standard deviation for this case study. Still, even for this case the variation is quite limited.

To better understand the nature of the motion fading and to be able to simulate its impact on the system performance, the probability distribution of the amplitude of the propagation loss relative to the median is investigated. To this end, a number of distributions, i.e. the normal, Rayleigh, Rice, Nakagami and log-normal, are considered. These distributions are commonly applied to model fading in RF wireless channels. Note that the Rayleigh distribution is a special case of the Rice (with $\nu = 0$) and Nakagami distributions (with $m = 1$). For the modeling, the data are first split into sets covering 5 MHz of bandwidth, since for larger bandwidths no coherence was observed. Then the least square fits of the different distributions are derived to

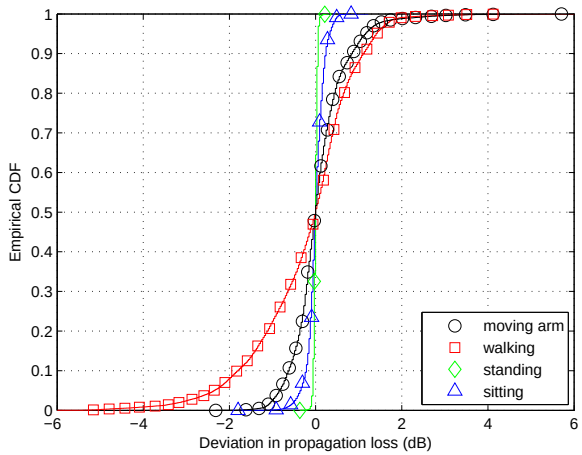

Fig. 5.3: ECDF of the deviation in propagation loss (in dB) due to body movement, for $4 \times 4\ \mathrm{cm}^2$ electrodes and a 1 cm electrode spacing on the arm channel (A2A3).

find the best fit parameters to the experimental data. The Probability-probability (P-P) plots are used to allow for visual inspection of the goodness of the fit distributions.

In the following, first the weighted least squares method is explained. Next, the P-P plot that is used to visualize the fitting results is introduced. Finally, the results obtained by applying this approach are discussed.

Weighted least squares

The weighted least square (WLS) method is applied to estimate the best fit parameters of a given distribution to the experimental data. This approach attempts to find the parameter(s) of a given distribution such that it minimizes δ, i.e. the weighted sum of the squared difference between the empirical CDF and theoretical CDF. The empirical and theoretical CDF are denoted by $f(x)$ and $g(x, \alpha)$, respectively. α denotes the best fit approximated parameter(s), w and x denote the weights and the experimental data, respectively.

$$w = \frac{1}{\sqrt{f(x)(1-f(x))}}, \tag{5.2}$$

$$\delta = \sum_{x} \left(w \left(g\left(x, \alpha\right) - f\left(x\right) \right)^2 \right) \tag{5.3}$$

The weights are defined in terms of empirical probabilities, and are lowest in the center of the plot and highest at the extremes. These weights compensate for the variance of the fitted probabilities, which is highest near the median and lowest in the tails [39]. This approach is often superior to maximum likelihood in some distributions like log-normal and Rayleigh where it sometimes necessary to estimate a threshold parameter. The likelihood for these models is unbounded and so maximum likelihood does not work [40].

In Figs. 5.4 and 5.5, the empirical CDF of the deviation in amplitude about the median (in dB) is compared to the results for the theoretical CDFs for the walking and moving arm scenario, respectively. The coupler size is 4×4 cm^2 with 1 cm electrode separation and the depicted results are for the arm channel when the TX and RX are located at A2 and A3, respectively. The considered frequency band is 40-45 MHz.

It is concluded that the log-normal, Nakagami and Rice distributions give a better fit than the normal and Rayleigh distributions, based on the results of all the sub-bands. This is also observed from Figs. 5.4 and 5.5.

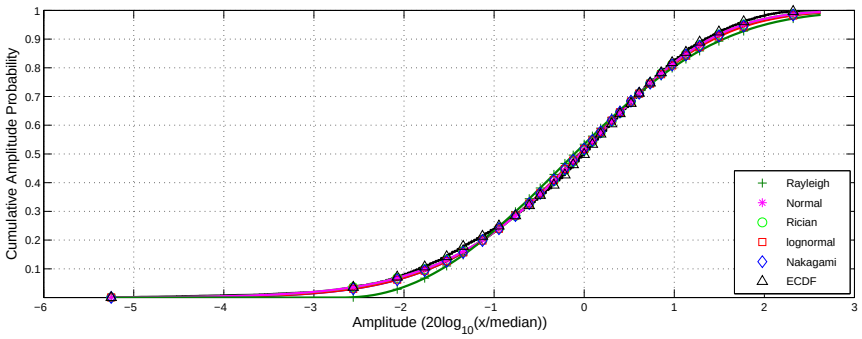

Fig. 5.4: ECDF of the deviation in amplitude (in dB) due to body movement together with the CDFs of the best fit theoretical distributions, for the frequency band of 40-45 MHz and the walking scenario.

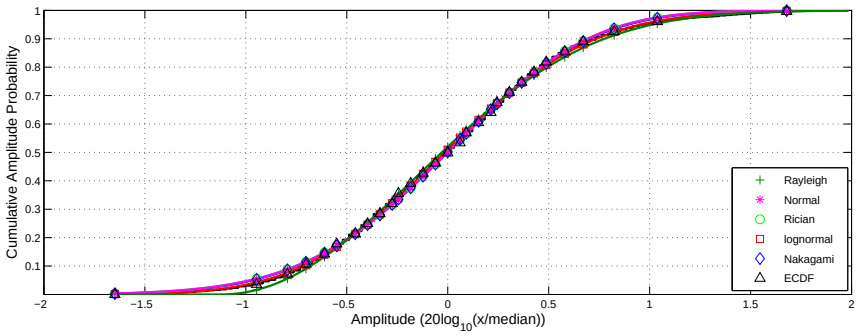

Fig. 5.5: ECDF of the deviation in amplitude (in dB) due to body movement together with the CDFs of the best fit theoretical distributions, for the frequency band of 40-45 MHz and the moving arm scenario.

In order to visually inspect which distribution yields the best fit, it is useful to test whether the measured data deviates from a straight line. This can be done using P-P plot.

Probability-Probability (P-P) plot

In a P-P plot, the empirical CDF is plotted against the theoretical CDF. A tight scatter along a 1:1 line from zero to one indicates that the theoretical CDF approximates the experimental CDF very well. Thus, the estimated parameters and the considered distribution can be used to explain the resulting data. This approach is used in this work to examine the goodness of fit for different distributions that were obtained by the WLS algorithm. Figures 5.6 and 5.7 illustrate the fit distributions for the walking and moving arm scenarios, respectively. The depicted results are for the measured data corresponding to Fig. 4.15 and the sub band 40-45 MHz.

As shown in these figures and based on the other results from the other frequency bands,

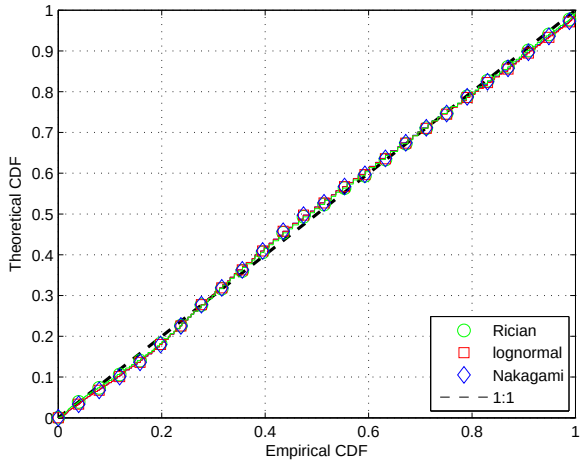

Fig. 5.6: P-P plot:ECDF of the deviation in amplitude (in dB) due to body movement vs. the CDFs of the best fit theoretical distributions, for the frequency band of 40-45 MHz and the walking scenario.

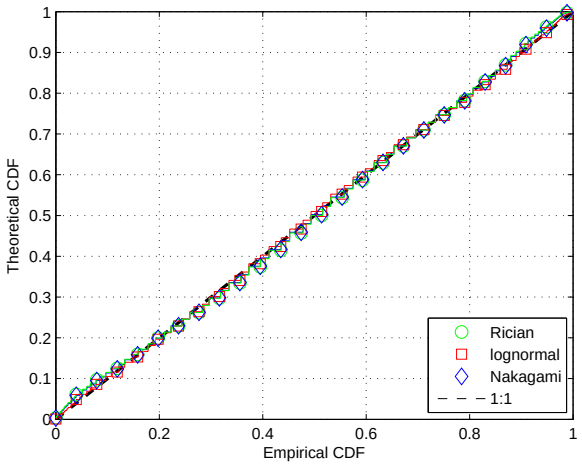

Fig. 5.7: P-P plot: ECDF of the deviation in amplitude (in dB) due to body movement vs. the CDFs of the best fit theoretical distributions, for the frequency band of 40-45 MHz and the moving arm scenario.

the log-normal distribution shows a good fit for most of the sub-bands, but the Nakagami and Rice distributions give a good fit for only some of the sub-bands. Tables 5.4 and 5.5 indicate the best fit parameters that were obtained for walking and moving arm, respectively for different positions on the body. The disadvantage of this method is that it does not show the behavior in the tail clearly. Overall, for most coupler configurations and positions on the body, the center of the distribution, from 0.1 to 0.9, is well modeled by all three distributions. The tails, however, are also of importance, since they often determine the error rate of the system.

To find the best tail-fit distribution, the fitness of the log-normal, Nakagami and Rice distributions has been examined on a logarithmic scale. These results are depicted in Figs. 5.8 and 5.9 for the walking and moving arm scenarios, respectively.

We can observe that the log-normal distribution has the best tail-fit for the moving arm scenario, while for the walking case the Rice distribution seems to achieve a slightly better fit. Therefore, focusing on the tail fit, from these results and results of other coupler locations (see Appendix C) it is found that the log-normal distribution shows the best overall performance. Moreover, it is concluded that high fades do not occur. Consequently, no wide variation in received signal strength due to body motion can be expected.

The log-normal parameter for the results illustrated in Figs. 5.9 and 5.8 are $\mu = 0.94$ and $\sigma = 0.06$ for walking and $\mu = -0.56$ and $\sigma = 0.11$ for the moving arm scenario. For the averaged overall 5 MHz sub-bands, the parameters for the walking and moving arm scenarios and for different coupler positions are indicated in Table 5.6 and 5.7.

These developed models are used in system simulations to analyze the performance of the

Table 5.4: Best fit parameters, walking, 40-45 MHz.

	m-Nakagami	**ω-Nakagami**	**ν-Rice**	**σ-Rice**	**μ-Log normal**	**σ-Log normal**
A2A3	12.92895211	1.013955246	0.985431139	0.140320009	0.942479118	0.054602767
A2A4	11.7647931	1.030163779	0.991118338	0.148230394	0.599979886	0.08081267
L2A2	89.75160186	1.004772249	0.999317939	0.052960909	–0.135270745	0.060175001
C3L2	63.42396655	1.010515103	1.000862191	0.062941308	–1.5255128	0.296532197

Table 5.5: Best fit parameters, moving arm, 40-45 MHz.

	m-Nakagami	ω-Nakagami	ν-Rice	σ-Rice	μ-Log normal	σ-Log normal
A2A3	59.60878241	1.004942801	0.997861022	0.064828862	–0.558821427	0.113943442
A2A4	35.47860057	1.005685118	0.995095421	0.084174439	0.285371453	0.063136608
L2A2	42.74647799	1.013925411	1.000429681	0.076870866	–0.589795238	0.139419831
A1A9	102.1241171	1.002146539	0.998373071	0.049652378	–0.023943223	0.050535347

BCC system. The mean propagation loss model is simulated by an attenuator and a high-pass filter. The filter and the attenuator parameters can be set to simulate different models of coupler

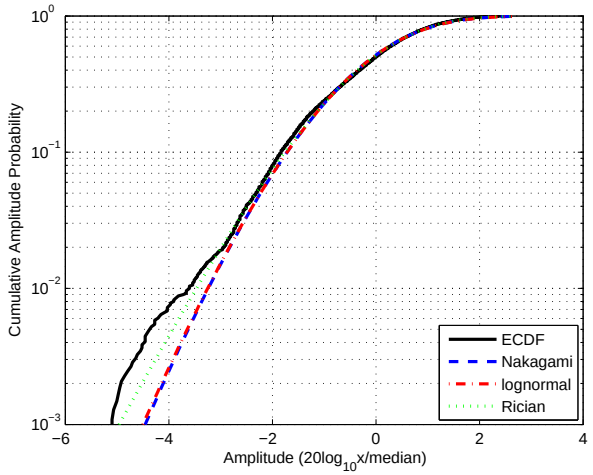

Fig. 5.8: ECDF (logarithmic scale) of the deviation in amplitude (in dB) due to body movement together with the CDFs of the best fit theoretical distributions, for the frequency band of 40-45 MHz and the walking scenario.

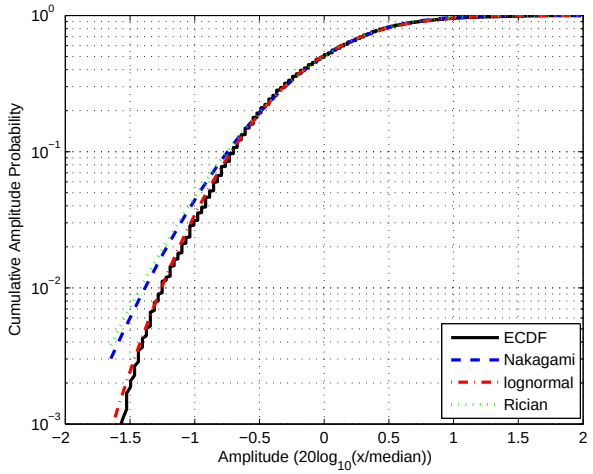

Fig. 5.9: ECDF (logarithmic scale) of the deviation in amplitude (in dB) due to body movement together with the CDFs of the best fit theoretical distributions, for the frequency band of 40-45 MHz and the moving arm scenario.

Table 5.6: Average parameter for the log-normal distribution, walking.

	$\overline{\mu}$	$\overline{\sigma}$
A2A3	0.671841632	0.086280789
A2A4	0.785766098	0.067375971
L2A2	–0.148502542	0.053398933
C3L2	–1.762826688	0.344682641

Table 5.7: Average parameter for the log-normal distribution, moving arm.

	$\overline{\mu}$	$\overline{\sigma}$
A2A3	–1.10706847	0.244301609
A2A4	–0.045311394	0.11453039
L2A2	–0.526608952	0.12481045
A1A9	0.174128407	0.037477556

designs and coupler locations. Also, the channel behavior due to the body movement is simulated by a log-normal fading generator, the parameters of which can be set for different test scenarios.

5.4 Summary and Discussion

In this section, models were presented for the propagation loss in static situation and its variation due to the body movement. To model the mean propagation loss, we defined the corner frequency f_c. The model of mean propagation loss has a different behavior below and above f_c. The level of attenuation is constant for frequencies below f_c and it is linearly decreasing for frequencies above f_c. It is shown that the parameters of the model depends on the locations of the transceivers on the body, the size of the couplers and their construction.

A statistical model was introduced for the propagation loss variation about median due to the body movement. It was shown that this fading is best modeled with a log-normal distribution. The results also showed that the fading due to the body movement is relatively small compared to RF body communication.

As seen in in Chapter 2, BCC was only statistically modeled by the authors of [24–27]. In their study, they statistically modeled the propagation loss in static situation and due to walking. In their results they showed that their data is best modeled by a normal distribution. However, their results are limited due to the "grounded scenario". Moreover, it is not clear how they extracted their data to come to such a model.

It is noted that this study is not exhaustive, since a statically relevant population is not achieved. Therefore, to come up with a quantitative conclusion on body channel modeling, more experiments with different subjects, in different environments and with couplers with different construction have to be carried out. This will allow to refine the understanding of on-body channel and come to an reliable BCC system design.

Chapter 6

Physical Layer Design

6.1 Introduction

Our study in the previous chapters provided us with insight about the on-body channel and its basic properties. This now allows us to design a physical layer, which is specifically suited for this channel. Although the channel characteristics also impact the design of the other open systems interconnection (OSI) layers of the BCC solution, these are outside the scope of this report.

It was found in the channel characterization work that the frequency dispersion of the on-body channel is very limited, consequently, it is not beneficial to apply multi-carrier techniques such as orthogonal frequency-division multiplexing (OFDM). Also, the low channel dispersion and fading due to the movement will allow for a very simple equalizer, the receiver signal processing can thus be relatively simple.

Our study also indicated that in BCC the communication range is limited to the close vicinity of the human body. This means there is no significant co-channel interference between BANs. Consequently, the whole frequency band of approximately 60 MHz can be reused by each BAN. This allows one to use wideband baseband modulation techniques over the whole bandwidth of 60 MHz. However, from the experimental results it is also observed that the interference of other RF and electronic systems using the band of 100 kHz to 60 MHz makes BCC susceptible to interference. The spectral properties of the interference vary and are location dependent. If not taken care of in the physical layer design, it will limit BCC system performance. The understanding of all of these aspects leads us to come to a suitable physical layer design for BCC, with high reliability and robustness against interference.

The outline of this chapter is as follows. In Section 6.2, the requirements for designing a suitable physical layer for BCC are detailed. The adaptive code-spreading scheme, the basis of our proposed physical layer design, is presented in Section 6.3. The numerical performance results for the proposed scheme are presented in Section 6.4. Finally, Section 6.5 presents the conclusions and discussion.

6.2 Requirements and System Design

It is very important that the BCC physical layer is power efficient, provides sufficient data-rate, is reliable and able to suppress the influence of interference as much as possible.

To illustrate the influence of interference, consider Fig. 4.25 which shows the characterization of the experienced interference in the lab room. For the case that the subject was standing

near the PC monitor, the integrated interference power for the whole frequency band of 60 MHz is -56 dBm. In order for the basic BPSK modulation to achieve a bit error rate (BER) of 10^{-4}, with a propagation loss of 80 dB via the human body, a 32 dBm transmit power is required. Since this level of power is higher than the standard value that can be applied to the human body and since it would make the solution very power inefficient, this modulation scheme is not suitable for BCC. Although this is a very simple calculation, it provides us with basic insight on how carefully the physical layer design of BCC has to be selected.

One of the key requirements for the physical layer design of BCC is power efficiency, because the BCC solution needs to be battery fed. Consequently, both TX and RX needs to be power efficient. To this end, a binary modulation is considered since it allows for simple TX and RX implementation. Note that with binary modulation we can still provide a configurable data-rate due to the large bandwidth. Also, no power consuming high frequency front-end is required due to relatively low frequencies used for communications, i.e. $<$ 100 MHz. The solution we propose is therefore based on baseband modulation.

As mentioned above, the frequency band of 100 kHz to 60 MHz is available for every BAN. This allows to choose one of the wideband modulation techniques for the physical design of BCC over the whole frequency band of 60 MHz. In this work, we study the use of direct sequence spread spectrum (DS-SS) to increase the resistance of communication against interference. This is due to the fact that the despreading circuit in the receiver acts as a spreading circuit for any signal to which it is not matched. So, if the received signal includes an interference signal, then the despreading circuit in the receiver spreads this interference over the whole band and the subsequent integrator rejects all but a narrow portion of the interference. This increased interference tolerance is an important motivation for using DS-SS in our physical layer design [41].

In this approach, there is a trade-off between interference robustness of the system and achieved data rate. The length and spectral shape of the code have a strong effect on the performance of the system. It should be noted that this technique is only used for its interference suppression properties not for multiple access (MA). In our foreseen system, MA is taken care of by the medium access controller by e.g. using carrier sense multiple access with collision avoidance (CSMA-CA).

It is important to mention that, the experienced interference will vary since the occupation of frequency bands by wireless systems is location and time dependent. The same holds for EM interference by electrical equipment. Consequently, it is not very beneficial to characterize the interference on average and design countermeasures based on this average, e.g. to choose a specific spreading code and apply it to the system to suppress the interference. Thus, a solution is required which can deal with the locally experienced interference, in order to reduce its impact.

In this study, we propose an approach that allows the BCC system to effectively operate in different interference environments. The proposed approach is based on a cognitive solution, where the RX of BCC is used to sense the medium when the channel is not used for data transmission. Based on the resulting observations about the interference properties, the system decides on the suitable spreading code. This spreading code is, subsequently, applied for transmitting and receiving data. Since in this proposed approach the spreading code is chosen adaptively to minimize the experienced interference, it will referred to as *adaptive code-spreading*.

6.3 Adaptive Code-spreading

Figure 6.1 shows the block diagram of the BCC physical layer design, which applies the adaptive code-spreading technique. At the TX, to transmit the data, every information bit $b[k] \in \{\pm 1\}$ is repeated M times, where k denotes the information bit index and M is known as the spreading factor. Then to randomize the repeated information bits, they are multiplied by spreading code (chips), $c[m] \in \{\pm 1\}$ of length M which results in $d[m]$ in the block diagram, where

$$d[m] = b[\lfloor m/M \rfloor]c[m], \tag{6.1}$$

and where the operator $\lfloor \cdot \rfloor$ denotes the floor function which rounds down to the closest integer. Finally, the spreaded data are modulated and sent to the human body with the coupler capacitively coupled to the body and with the return path through the air and environment, as explained in Section 1.2.2. The transmitted data, $s(t)$, with BPSK modulation is

$$s(t) = \sum_{m=-\infty}^{\infty} d\,[m]\, p(t - mT_{\mathrm{c}}), \tag{6.2}$$

where $1/T_c$ is the chip rate and $p(t)$ is the chip pulse shape, which is assumed to have unit energy.

At the RX, the received signal $r(t)$ is given by

$$r(t) = s_1(t) + n(t) + i(t), \tag{6.3}$$

where $s_1(t)$ denotes the transmitted signal after propagation through the body, $n(t)$ represents the contributed white noise and $i(t)$ denotes the experienced interference. First the received signal is fed into the BPSK demodulator, which consists of a matched filter (MF) that is matched to the $p(t)$ chip pulse shape (chip-matched filter) assuming perfect chip synchronization. The matched filter output samples $y[m]$ are given by

$$\begin{aligned} y[m] &= s_{\mathrm{MF}}[m] + n[m] + i[m] \\ &= A\, c[m]b[\lfloor m/M \rfloor] + n[m] + i[m], \end{aligned} \tag{6.4}$$

where we for simplicity assumed that the channel is linear with gain A. Subsequently, the sampled output of the matched filter is despreaded by the spreading code by a so-called despreading operation, yielding:

$$\begin{aligned} y_{\mathrm{d}}[m] &= y[m]c[m] \\ &= b[\lfloor m/M \rfloor]c^2[m] + n[m]c[m] + i[m]c[m] \\ &= b[\lfloor m/M \rfloor] + n'[m] + i[m]c[m], \end{aligned} \tag{6.5}$$

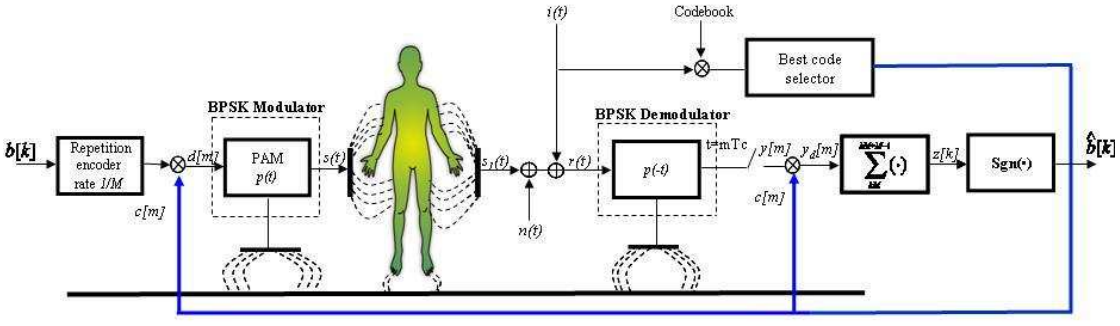

Fig. 6.1: Block diagram of the physical layer communication concepts.

where we used that $c^2[m] = 1$ and due to the properties of the spreading code $n'[m]$ is a noise term statistically equivalent to $n[m]$. After despreading, for bit information detection, the data is integrated over one symbol period, which yields the following output:

$$z[k] = (1/M) \sum_{m=kM}^{kM+M-1} y_d[m] = (1/M) \sum_{m=kM}^{kM+M-1} y[m]c[m \bmod M]. \tag{6.6}$$

When we call (6.4) and (6.5), we obtain

$$z[k] = (1/M) \sum_{m=kM}^{kM+M-1} A\, b[\lfloor m/M \rfloor] + (1/M) \sum_{m=kM}^{kM+M-1} n'[m] + (1/M) \sum_{m=kM}^{kM+M-1} i[m]c[m \bmod M], \tag{6.7}$$

and therefore

$$z[k] = A\, b[k] + v[k] + w[k], \tag{6.8}$$

where the $v[k]$ and $w[k]$ are the noise and interference terms, respectively. Finally, the information bit decisions, $z[k]$, are fed into the detector to find the transmitted information bits.

As we can see from (6.6), the despreading accumulation is equivalent to the operation of cross-correlation between the received signal $y[m]$ and the spreading code $c[m]$ computed on the k^{th} symbol period. By choosing a spreading code that is not correlated to the interference $i[m]$, the power of the interference term $w[k]$ in (6.8) can be minimized. Thus, the performance of the system can be optimized.

The best code selector depicted in Fig. 6.1 uses this property at the RX in order to select the best code to suppress the interference influence. Therefore, when there is no data transmission occurring, first the experienced interference is studied at RX side. During this time, different spreading codes from a codebook are correlated with the interference signal in order to find the code that minimizes the influence of the interference. This code can be considered to be most "orthogonal" to the interference. The way that we measure this orthogonality is by computing:

$$P_{I,j} = \left| \frac{1}{M} \sum_{m=1}^{M} i[m]c_j[m \bmod M] \right|^2, \tag{6.9}$$

where j refers to j^{th} code. After applying all the codes out of the codebook, the one yielding the smallest P_I is chosen. It is noted that in this algorithm we assume two way communications. Therefore, after RX does the sensing and finds the proper code, it reports to the TX which code is chosen. Basically, the sensing of the medium can be on the regular basis. Since humans are generally quite stationary, the frequency of this sensing needs not to be too high. So, regular code updates in the order of 10s of seconds (or even minutes) is enough. This, however, would require a relatively long considerable sensing time and draw lots of power. Hence, another approach is to only do the sensing and adaptation when the system performance is degraded, e.g. when bit or packet errors occur. In this way, the sensing time would be much shorter, which considerably saves power.

In this work, Walsh-Hadamard (WH) sequences are considered. The motivation for using the Walsh-Hadamard is that the sequences in the Walsh-Hadamard codebook have sufficiently different non-white spectra. So, these codes can be applied to the interferences with different spectral properties to evaluate the performance of employing the adaptive code-spreading, which is the goal of this study. Also, all but one of the Walsh-Hadamard sequences are DC free, hence the signals are shaped such to keep them away from the frequencies below 100 kHz. A

Walsh-Hadamard matrix of order N is defined as an $N \times N$ matrix H, with the property that $HH^T = NI$, where I is the $N \times N$ identity matrix. Hadamard matrices whose dimensions are a power of two can be constructed in the following manner:

$$H_{2N} = \begin{bmatrix} H_N & H_N \\ H_N & -H_N \end{bmatrix}, \tag{6.10}$$

with $H_1 = [1]$. The spreading code is selected as a row of this matrix. Figure 6.2 illustrates the power spectrum of the two Walsh-Hadamard codes for length 32 and 128. We can observe from Figs. 6.2(a)– 6.2(d) that different codes with the same code length have different spectral shapes. By utilizing the code selection algorithm the code, which is most "orthogonal" to the locally experienced interference is selected. Also, by comparing the different graphs in Fig. 6.2, it can be observed that by increasing the code length the spectral density of the codes gets sharper. Consequently, longer codes can potentially minimize the interference more effectively. After the best code is selected, this code is used for spreading of the data at the TX and despreading the received signals at the RX.

It is noted that the data rate is scaled using codes with different spreading code lengths, i.e. when the level of interference is low, a short code is used and when it is high, a larger code length is used. The advantage of longer codes is that they achieve better spectral shaping and thus yield a better interference suppression at the receiver, however, at the cost of sending more

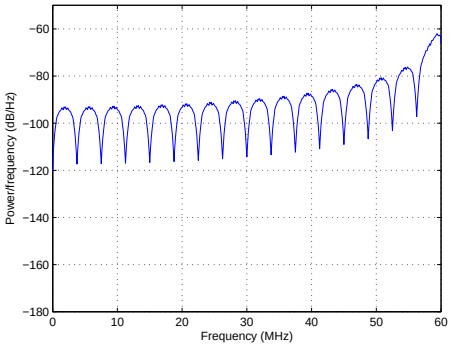

(a) PSD of the code 2 of the Walsh-Hadamard codebook of length of 32.

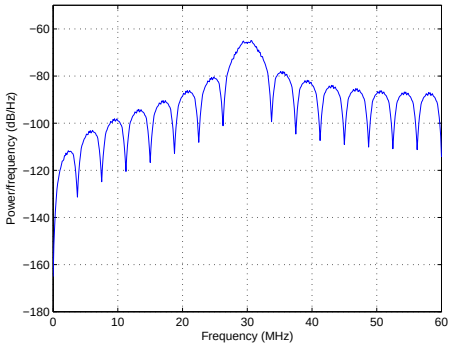

(b) PSD of the code 4 of the Walsh-Hadamard codebook of length of 32.

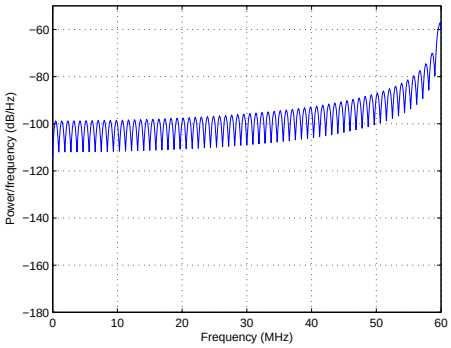

(c) PSD of the code 2 of the Walsh-Hadamard codebook of length of 128.

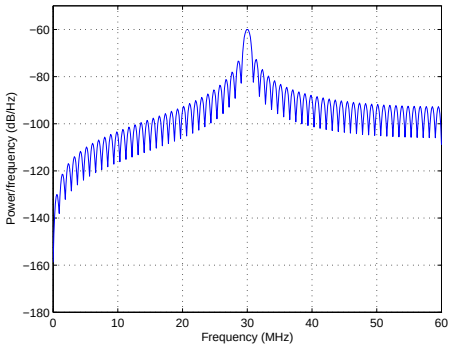

(d) PSD of the code 4 of the Walsh-Hadamard codebook of length of 128.

Fig. 6.2: Power spectral density of two of the Walsh-Hadamard sequences for codelengths of 32 and 128.

energy per information bit and a reduced data rate. The same is true for the time spend in the cognition part. The longer the cognition period, the better the optimal code can be selected, but it also reduces the time that can be spend on data transmission and consequently reduces the data rate.

In some schemes it might be beneficial to select the optimal code at the TX side. Again the power of the correlation of the code with the the interference is measured. This is iterated for the whole codebook until the optimal code is found, which minimizes the absolute value of this correlation output. The disadvantage of the solution is that the TX and RX might not experience the same interference, therefore the suppression of the interference at the RX might be lower.

6.4 Numerical Results

In order to understand and assess the performance of the proposed physical layer for the BCC channel, Monte Carlo simulations were performed. To this end, the human body channel behavior is simulated. Also, the influence of the spreading code spectral shape and length are investigated. Moreover, the performance of the code selection algorithm is studied. Finally, the performance of the whole system is studied under white noise and colored interference.

It is noted that in all our assessments the energy per chip E_{c} is considered in SIR and SNIR, so not the energy per information bit E_{b}. This is due to the fact that we want the final system to adaptively change spreading code to achieve better performance. In order to see this reflected in our system simulation results $\mathrm{SIR} = \frac{E_{\mathrm{c}}}{I_0}$ and $\mathrm{SNIR} = \frac{E_{\mathrm{c}}}{N_0+I_0}$ are calculated, where N_0 and I_0 denote noise and interference power spectral density, respectively.

6.4.1 BCC physical layer simulation

Figure 6.3 depicts the block diagram of the considered BCC physical layer simulator. In this simulator, the attenuator simulates the impact of the level of the propagation loss ("path loss") through the body. In this simulation the path loss was set to 55 dB. The frequency behavior of the BCC is simulated by a high-pass filter with a corner frequency of 25 MHz. The motion fading due to the body movement is simulated by a lognormal fading generator. The mean and standard deviation of the log-normal distribution were set to 0.67 and 0.1, respectively. The values for the simulation of the body channel are selected based on the values of the models in Section 5.3.

The block diagram to simulate the behavior of the interference is shown in Fig. 6.4 By

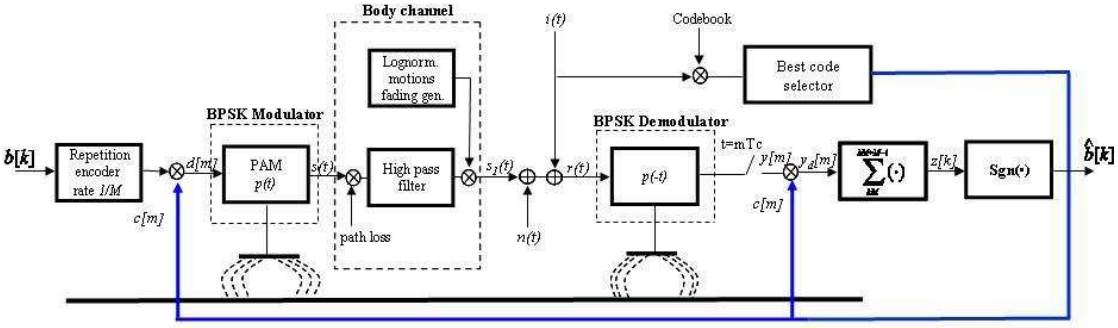

Fig. 6.3: Block diagram of BCC physical layer simulator.

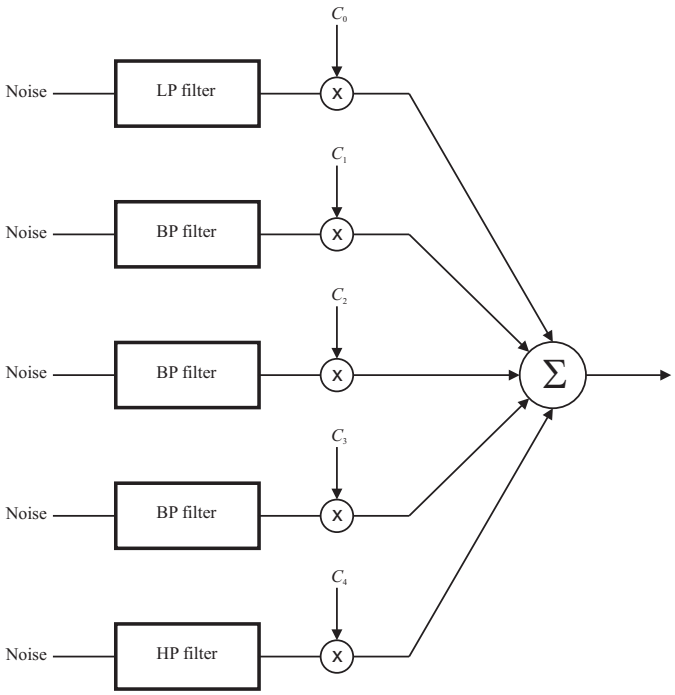

Fig. 6.4: Block diagram for the interference simulator.

changing the filter parameters different spectral profiles can be generated. This simulates the spectral properties of the interference and the time and location dependence of the interference. Figure 6.5 depicts five different profiles that have been used for the simulation of interference in this study.

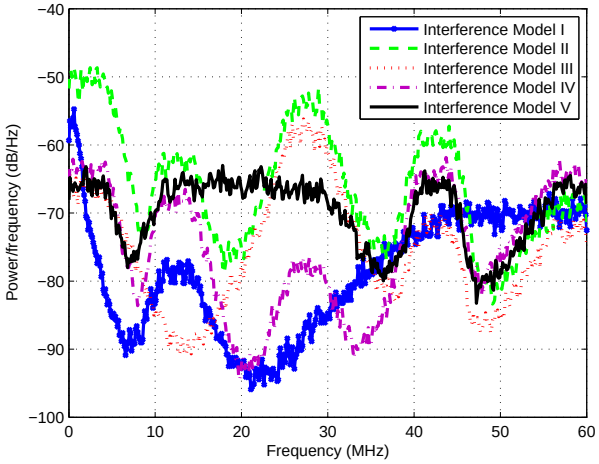

Fig. 6.5: Power spectral density of the different interference profiles used to simulate interference.

6.4.2 Influence of different spreading-codes

To assess the influence of the different codes, all the Walsh-Hadamard sequences of code length 32 are applied at the TX for spreading and at the RX for despreading of the data. In this case, no feedback from the experienced interference is considered and it was assumed that there was no white noise in the system. Consequently, the transmitted data is only affected by the on-body channel and the interference.

Figure 6.6(a) illustrate the BER performance for all the spreading codes of the codebook. The signal to interference ratio (SIR) is defined as the average received modulated signal power to the average received interference power,

$$\mathrm{SIR(dB)} = 10\log_{10}\frac{\sigma_{s1}^2}{\sigma_i^2}, \tag{6.11}$$

where σ_{s1}^2 denotes the average received modulated signal power and σ_i^2 denote the average received interference power. It is noted that the power spectral density (PSD) of the simulated interference is the same as that of interference model I in Fig. 6.5. Figure 6.6(a) shows that there is a remarkable difference in performance of the system for the different codes. A 24 dB SIR improvement in the system can be achieved by choosing between the worst and best code for interference with this spectral property. This shows that spreading code3 is most orthogonal to the interference, therefore the interference at the receiver is best suppressed with this code.

For the other interference models with different spectral properties, similar results were achieved. The codes achieving the best and worst results are different for the different interference profiles and the gain between best and worst code varies from 8 dB to 24 dB for the considered interference models (see Appendix D). Less gain is achieved for more flat spectral interference profiles. Figure 6.6(b) shows the results for interference model V that was shown in Fig. 6.5. For a BER of 10^{-4}, 8 dB SIR gain is achieved between choosing the worst code or the best code for this case. This result verifies that for the interference with the spectral properties close to that of white noise, the performance of this method is lower.

It is also interesting to compare the performance of the system for these specific codes with the average performance for the case of applying a random spreading code. Figure 6.7 shows that for interference model I the random code is better than the worst case. However, still 21 dB gain is achieved by applying the optimal code to the system for a BER of 10^{-4}, compared to applying a random code.

6.4.3 Spreading-code length

In order to examine the influence of the code length on the system performance, two different cases are compared. In both cases, only interference is effecting the received signal and no feedback for sensing the medium is considered. In the first case study, the performance of the system applying random code spreading with code lengths of 16, 32, 64 and 128 and interference model I is examined. The results in Fig. 6.8 show 6 dB SIR improvement for a BER of 10^{-4} by increasing the code length from 16 to 128. Therefore, using a longer code while applying a random code will improve the performance of the system.

In the other case study, two specific code numbers are selected from the Walsh-Hadamard codebook and the selected codes with different code length of 16, 32, 64 and 128 are applied in the system. The selected codes are the codes which gave the worst and the best performance for code length of 32 and using the interference model I, as shown in Fig. 6.6(a). The worst and best codes are code1 and code3, respectively. Figure 6.9 depicts the results for these two codes. It can

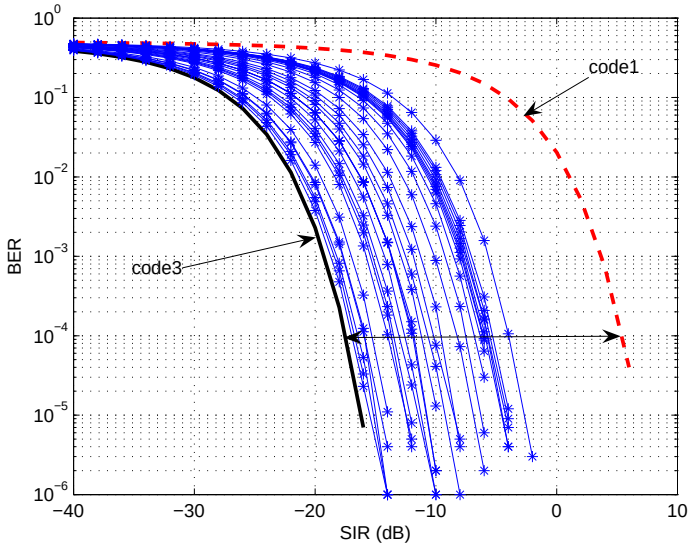

(a) Results for interference model I.

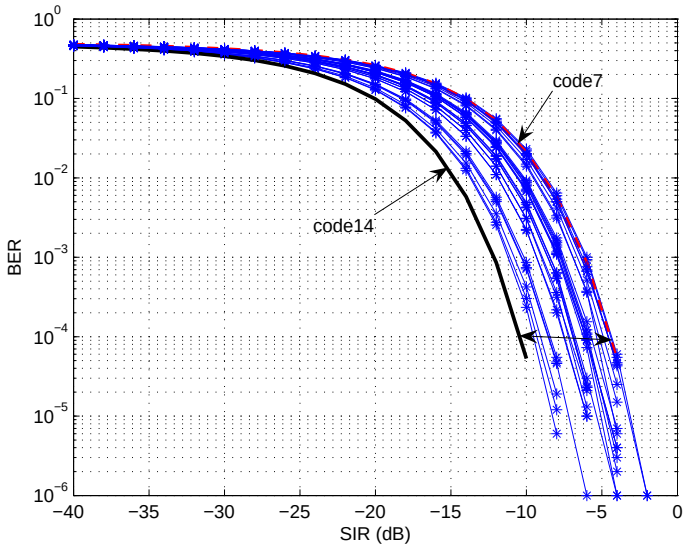

(b) Results for interference model V.

Fig. 6.6: BER performance for code spreading for all codes in the WH codebook of length 32.

be concluded from these graphs that using a longer code yields more performance improvement for the code which is more orthogonal to the interference signal. In this case study, for a BER of 10^{-4}, 4 dB SIR performance improvement is achieved for code1 going form codelength 16 to 128. In contrast, applying the code3 yields 12 dB SIR improvement. These results are lower and higher than the result of the average code, respectively. Similar results for the other interference models are obtained. This verifies that due to the sharper spectral properties of the longer code, the performance of the system can be more improved. This is, however, at the cost of sending more energy per information bit and a lower data rate.

It is also interesting to examine the performance of the system by applying the whole code-

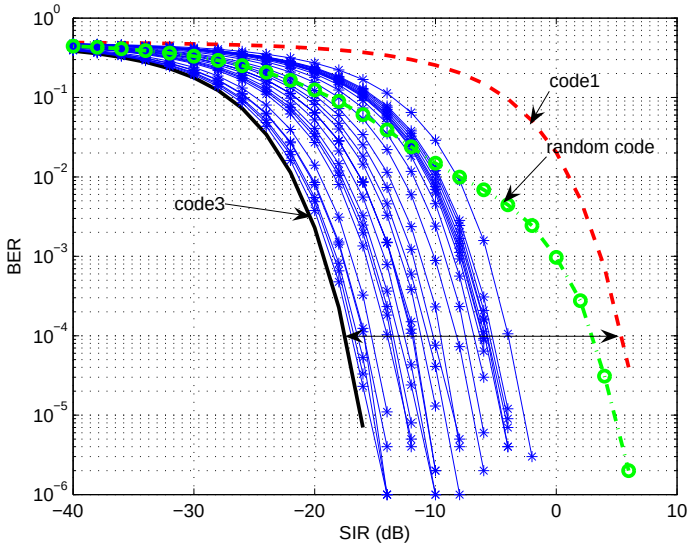

Fig. 6.7: BER performance for code spreading for all codes in the WH codebook of length 32 and a random spreading code, for interference model I.

book of 128 code length. Figure 6.10 shows that there is a 28 dB SIR difference between the worst code shape and the best code shape for a BER of 10^{-4} and interference model I, compared to 24 dB SIR of codelength 32. This shows that due to the better spectral shaping for the longer code, better performance is achieved. Consequently, the longer code with the best code shape should be selected to minimize the influence of high interference.

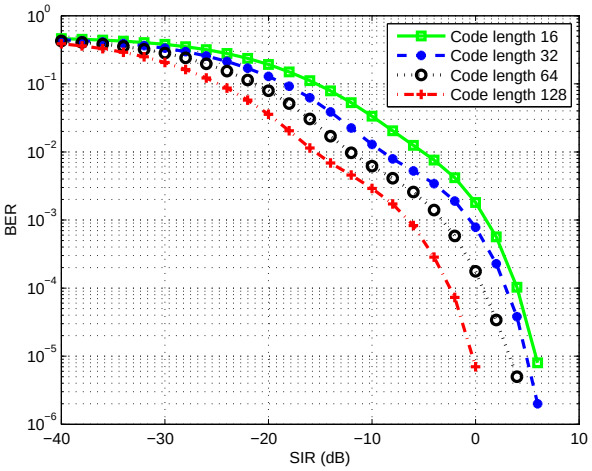

Fig. 6.8: BER performance for code spreading, random code of length 16, 32, 64 and 128 in the WH and for interference model I.

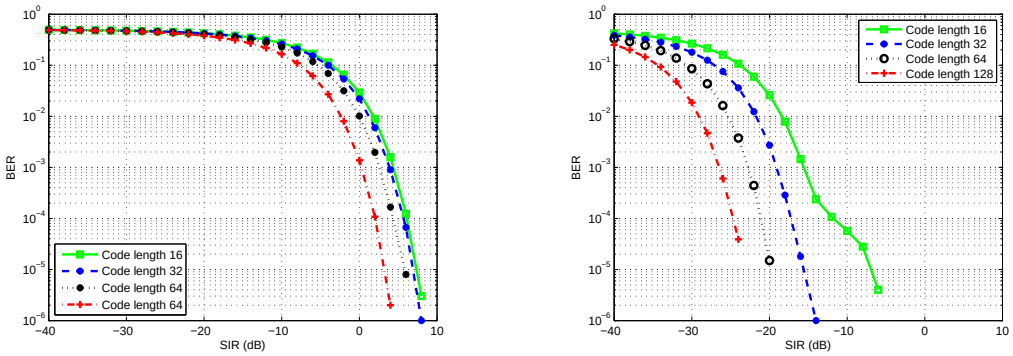

(a) Code 1 of the Walsh-Hadamard codebook. (b) Code 3 of the Walsh-Hadamard codebook.

Fig. 6.9: BER performance for code spreading for code 1 and 3 code of length 16, 32, 64 and 128 in the WH and for interference model I.

6.4.4 Best code selection algorithm

By studying the numerical results on different code shapes and lengths, it is observed that there can be a remarkable improvement in system performance when the best code is selected, compared to a random code. In this subsection, the performance results for the proposed best code selection algorithm are presented.

In this algorithm, first the interference in the medium is sensed at the RX when there is no data transmission. Then the spreading code that is least affected by interference is selected, by finding the code with the minimal correlation with the interference. This spreading code is applied to the system. Figure 6.11 illustrates the performance of the system for different code selection times, where the interference is simulated by interference model I. In this figure, the selection time, which is the observation time used to estimate the optimal code, is normalized by the length of the spreading code. As can be observed, the selection is improved by increasing interference sensing time and an improved performance is achieved. It also can be observed that

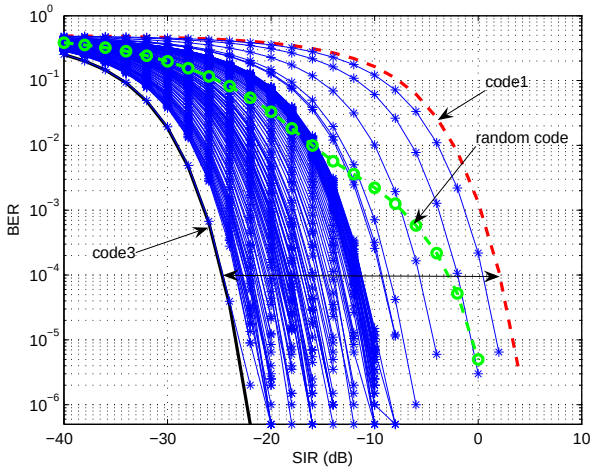

Fig. 6.10: BER performance for code spreading for all codes in the WH codebook of length 128 and for interference model I.

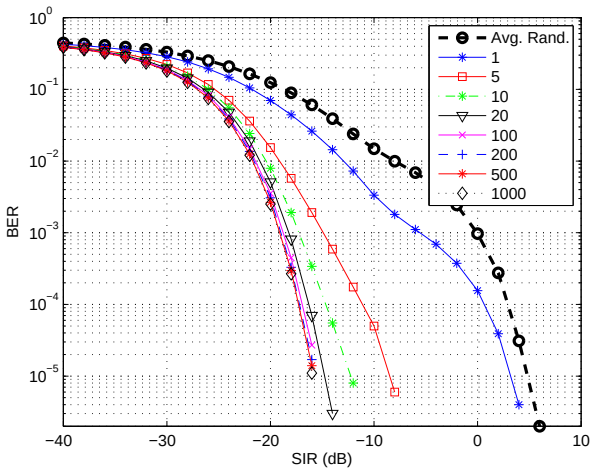

Fig. 6.11: BER performance in code selection algorithm for different code selection times together with BER performance of code spreading for the random code, for interference model I.

there is 12 dB SIR improvement from code selection time 1 to code selection time 5. However, by increasing the time selection to 10, it yields 3 dB SIR more improvement. After 20 code selection time the optimal code is already selected. This is also illustrated by Fig. 6.12, which shows the histograms of the selected best code for different periods of interference study. As we can observe, the number of times that code3 is selected as the optimal code increases by increasing the period of the sensing time. However, even for the code selection time 5, which is not a long period, code3 is selected more often as the optimal code. From these results, it can be concluded that the sensing period in order to find the optimal code is limited and even in a very short period of time this solution yields a good performance improvement (see also Appendix D).

In Fig. 6.11, the performance of the system is also compared to that of a system applying a random code. The results shows that even for the very short selection time (equal to the code-length), 3 dB gain is achieved at a BER of 10^{-4}. Similar results are observed for interference profiles with different spectral properties. These results show the effectiveness of applying this algorithm to minimize the impact of the locally experienced interference.

6.4.5 Noise and interference

In this section, in order to have a complete system simulation, white noise is also added to the received signal. Its level is made proportional to the experienced interference. The motivation for this investigation is to examine the performance of the proposed physical layer system when the received signal is affected by different levels of noise and interference. The signal to noise and interference ratio (SNIR) is defined by

$$\mathrm{SNIR(dB)} = 10\log_{10}\frac{\sigma_{s1}^2}{\sigma_i^2+\sigma_n^2}, \tag{6.12}$$

where σ_{s1}^2 denotes the average received modulated signal power and σ_n^2 and σ_i^2 denote the average received noise power and the average received interference power, respectively. The gain at

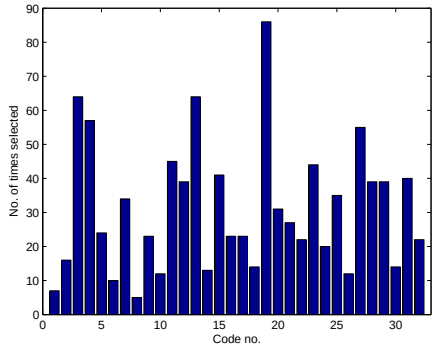

(a) Histogram of the best code of 1 selection time.

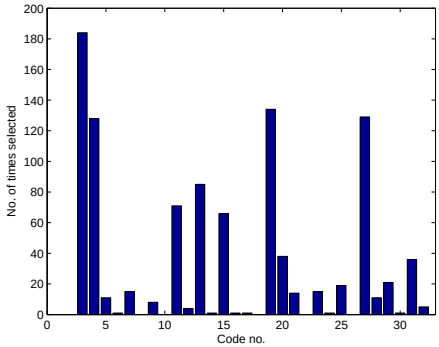

(b) Histogram of the best code of 5 selection time.

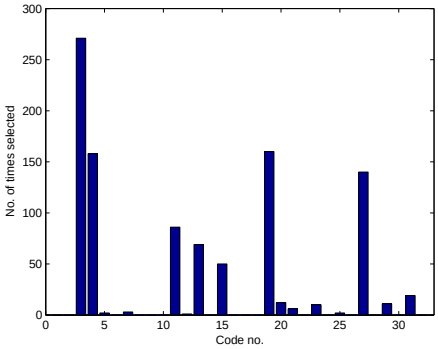

(c) Histogram of the best code of 10 selection time.

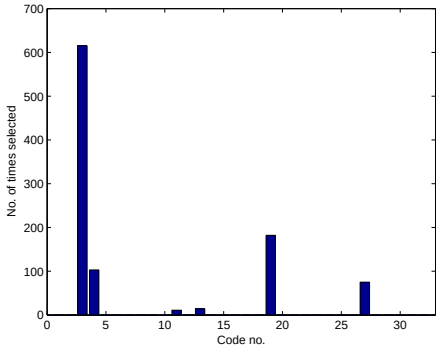

(d) Histogram of the best code of 100 selection time.

Fig. 6.12: Histograms of the selected best code for different period of interference study, for interference model I.

the code spreading and selection is defined as follow:

$$\mathrm{Gain}(\alpha) = \mathrm{SNIR}_{\mathrm{Rand.code}}(\alpha) - \mathrm{SNIR}_{\mathrm{Code\ est.}}(\alpha), \tag{6.13}$$

where α denotes the power level of interference to noise in the system, which is between zero and one. When α equals zero, the received signal is only affected by the white noise and when α equals 1 only interference affects the received signal. $\mathrm{SNIR}_{\mathrm{Rand.code}}$ and $\mathrm{SNIR}_{\mathrm{Code\ est.}}$ denote the signal to noise and interference ratio (SNIR) for applying a random code and the code selection algorithm, respectively. They are calculated for a specific BER value as a function of α. The power spectral density of the noise and interference for $\alpha = 0.1$ and $\alpha = 0.9$ is illustrated in Fig. 6.13. As we can observe by comparing the two figures, when $\alpha = 0.1$ the power spectral density more resembles the white noise, whereas for $\alpha = 0.9$ it is more like interference model I profile. Figure 6.14 depicts the gain of (6.13) versus α for a BER of 10^{-4} and codelength 32 and for three different time selections (10,20,100) of the code selection algorithm. When the system is experiencing only white noise, i.e. $\alpha = 0$, no gain is achieved. However, when the noise plus interference signal is non-white, up to 20 dB gain is achieved by selecting the optimal codes. The conclusion to be drawn from this figure is that when the system is experiencing white noise there is no gain, but neither loss in employing the proposed adaptive code-spreading scheme. However, there is a remarkable gain utilizing this approach when there is variation in the spectral properties of the interference. Similar results are achieved for the other interference models. Less improvement was achieved for the interference model V, as was expected, since its spectral properties are close to white.

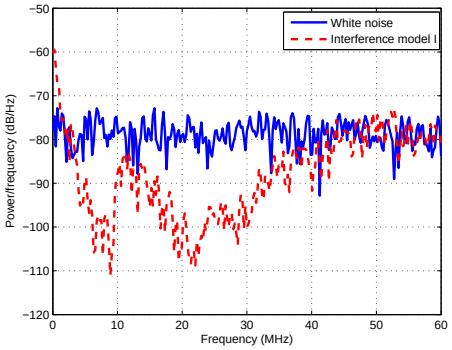

(a) Power spectral density of white noise and interference model I.

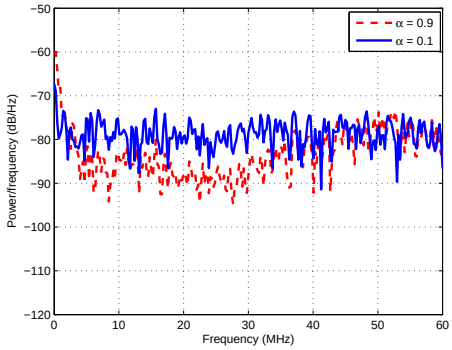

(b) Power spectral density of noise and interference for $\alpha = 0.1$ and $\alpha = 0.9$.

Fig. 6.13: Experimental power spectral density of white noise and interference signals.

6.5 Conclusion and Discussion

This chapter reviewed the requirements for designing a suitable physical layer for BCC using the BCC channel characterization and on-body channel model. Based on these requirements, adaptive code-spreading was proposed as basis for the BCC physical layer design. This is an adaptive solution which minimizes the influence of the locally experienced interference, which might effect the BCC system performance. In this solution, the medium is sensed at the RX or TX and a spreading code is chosen and applied on the TX and RX for spreading and despreading of the data, respectively. The selected spreading code has minimal correlation with the experienced interference. It was proposed to use the Walsh-Hadamard sequences as the spreading codes. The best code from the whole codebook was selected by the proposed code selection algorithm, to reduce the impact of the interference.

The performance of the proposed solution has been assessed using Monte Carlo simulations. It was concluded from the results that choosing a code with a minimal correlation with

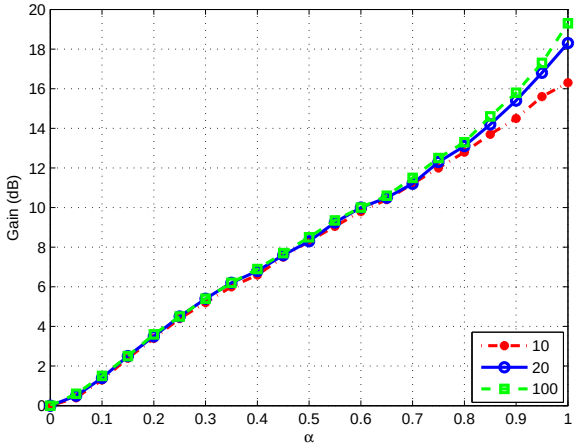

Fig. 6.14: Performance gain of code selection algorithm versus ratio between noise and interference for different time sensing periods where the system is sensing noise + interference, for a BER of 10^{-4} and codelength of 32.

interference yields a remarkable performance improvement in the communication system. Also, increasing codelength could improve the performance of the system. However, there is a clear trade-off between the performance and the data-rate of the system when considering different code lengths. Moreover, by increasing a longer code more energy per information bit is sent which consumes more power. The results also showed that the sensing time in order to find the optimal code is relatively short. It was concluded from the numerical results that this solution will provide a performance gain when the communication system only experiences non-white noise and interference.

In this study, to evaluate the performance of the algorithm, only 5 different profiles were developed to model interference and for the spreading code only the Walsh-hadamard sequences were examined. It should be remarked that more works needs to be done on the proposed approach, both regarding evaluation and code-spreading scheme. For the evaluation, measured interference signal could be used to test the performance of the code selection algorithm. For the code-spreading scheme, codes other than Walsh-Hadamard codes and other selection algorithms need to be studied.

Other methods to create different transmission modes applicable in this context can be investigated. One of the possible solutions is frequency hopping, where the hopping sequence is adjusted based on the experienced interference. Frequencies with considerable interference could for instance be used less often in the sequence or omitted from the hopping sequence. This solution, in some sense, is similar to the proposed scheme. For some low data rate application, however, it might be beneficial to design a narrow band solution, e.g. based on frequency shift keying (FSK). This enables the use of narrow band electronics and can potentially reduce the power consumption and the interference susceptibility.

In Chapter 2, different modulation schemes for BCC developed by other groups were presented. In most of these works, narrow band modulation was proposed for the BCC modulation scheme. However, none of these investigations other than the ones by authors of [28–35] considered the influence of the interference on the BCC channel and in their system design. The authors of [34] proposed adaptive frequency hopping (AFH) as a solution in order to combat interference. In their solution they claimed that AFH can improve the signal to interference ratio (SIR) performance of BCC by more than 10 dB.

Chapter 7

Conclusions and Recommendations

7.1 Conclusions

Capacitive body-coupled communications (BCC) is a new approach for WBANs to interconnect the devices which are on, or in the close vicinity of, the human body. The applications considered are in the domains of consumer lifestyle and healthcare. In order to obtain a better understanding of the basic principles and properties of BCC, the characteristics of the on-body channel communication have been experimentally investigated in this work. For this purpose, a dedicated measurement system has been developed which is isolated from the earth ground. This way, it is ensured that the studied channel is only the body channel as experienced in actual WBANs.

In the first part of this work, measurement results are presented that characterize the influence of coupler design, coupler position and body movement on the signal propagation loss for the frequency band of 100 kHz to 60 MHz. Furthermore, various experimental results are presented that to some extent characterize the influence of interference.

The results show that the on-body channel signal transfer follows a high-pass like behavior, which depends on the dielectric properties of the human tissue, dielectric properties of the material between the electrode pair, the coupler size and the distance between TX and RX. Moreover, it was found that the channel dispersion is very low compared to the results of wireless RF solutions. Measurements have also shown that the propagation loss increases by increasing the distance between the couplers interacting with each other, although for almost all node locations, the propagation loss is well below 80 dB. The communication range of BCC has been shown to be limited to the close proximity of the human body. Therefore, there is no significant interference between different WBANs and the whole frequency band can be reused by all WBANs.

From the study on the coupler form factor, it is concluded that increasing the size of the coupler, i.e. electrode dimensions and electrode spacing, reduces the propagation loss. This can likely be explained by the fact that by increasing the dimensions, the formed capacitor between the body and the electrode gets larger and thus induces more electric field to the body. Additionally, by increasing the electrode spacing the formed capacitor between two electrodes gets smaller, which results in lower impedance between them. Consequently, more electric field can be induced to the body. Therefore, regarding the coupler form factor, there is a tradeoff between the receiver sensitivity and the node size. In this study, it has been concluded that the coupler of $3 \times 3\ \mathrm{cm}^2$ and 1 cm spacing achieves a nice tradeoff between propagation loss and

size of the BCC node.

Body movements result in a higher variation in attenuation compared to the static situation. A possible explanation might be the capacitive coupling of the electrodes to the other parts of the body while moving, resulting in decreased loss for a certain period of time. However, from the results of body movement, it has been concluded that the variation in channel attenuation of BCC is very small and the maximum observed standard deviation is less than 3 dB.

Finally, results from interference experiments showed that capacitive coupling is susceptible to interference from other electronic equipment. The characteristics of interference largely depend on the location. However, similar results were obtained for the measured interference performing the same experiment on different subjects. The results also showed that the spectral properties of interference vary within each case.

In the second step, models have been developed based on the experimental data to describe the behavior of mean propagation loss for static body situations and also to describe the propagation loss variation due to the body movement. These models provide us with information for the system design for reliable data transmission and receiver techniques to compensate for these impairments. The mean propagation loss for the static model has been shown to have a linear behavior with frequency. Moreover, it is shown that the channel attenuation reduces at higher frequencies due to the dielectric properties of the human tissues and the materials between the electrode pair. Regarding the body movement, log-normal, Nakagami and Rice distributions gave a good fit to the propagation loss variation in the center of the distribution from 0.1 to 0.9. But since the log-normal distribution showed the best tail-fit to the measured data, the propagation loss fading due to the body motion was modeled by the log-normal distribution.

Finally, based on the knowledge of the channel characteristics and interference properties, we developed a solution for an energy efficient physical layer. The proposed adaptive code-spreading scheme allows to effectively reduce the impact of the experienced location dependent interference. It is based on varying the spreading code after sensing the channel and interference. A code which was less correlated with the interference was chosen as the spreading code. The performance of this solution was assessed by Monte Carlo simulations. The Walsh-Hadamard sequences were proposed as spreading codes. It is concluded from the results that the code which was selected by the code selection algorithm as the optimal code could improve the performance of the system compared to applying a random code. Moreover, it was shown that the sensing time of the channel in order to find the optimal code is very limited. The numerical results also showed that applying a longer code yields a better interference suppression due to its better spectral shape. However, this reduced the data rate. Finally, it was concluded that the adaptive code-spreading provides performance gain when the system is experiencing non-white noise and interference.

In this work, the propagation loss values are similar to those observed for RF-based WBANs in previous literature [6]. However, due to the much lower carrier frequency, the lower channel dispersion and the much lower fading due to body movement, BCC can result in a much simpler and more robust communication solution with a low power consumption, compared to traditional RF-based WBANs. Hence, this leads us to the conclusion that BCC is a promising basis for future WBANs.

7.2 Recommendations for Future Research

There are several issues that still are to be addressed in order to enhance the understanding of the experimentally observed behavior of the on-body channel. In this section, some suggestions are made for future experimental investigations to characterize the BCC channel. Also, recommendation will be made about the future work on BCC systems and physical layer design.

Although the presented results allow us to draw qualitative conclusions about the capacitive BCC channel, this work is not exhaustive, as a statistically relevant population is not yet achieved. Therefore, more tests need to be performed to draw solid quantitative conclusions.

In the current investigation, experiments have been performed in a conference room and EMC room. The influence of other environments like outdoors on BCC needs to be investigated. Moreover, in this study the locations of coupler are limited to seven locations. More measurements on other locations of the body need to be studied. Furthermore, only two types of movement have been considered to understand the influence of body motions on BCC. It would be interesting to perform more experiments on the body movement. The case could be investigated in which not only the body, or one part of the body, is moving but in which also the TX and RX are moving relatively to each other.

For further experimental study, more measurements needs to be done on different subjects with different body structure. Also, different dielectric materials between the electrode pair need to be examined. These investigations provide us with a more clear understanding of the influence of permittivity and conductivity of the body and coupler dielectrics on the signal transfer behavior.

Consequently, such further refined understanding will allow one to come to a more reliable channel model, e.g. the introduced parameters in our proposed model can be function of the coupler size, the coupler locations, the environment and structure of the body. This also allows for a more reliable physical layer design based on these properties.

Moreover, it is expected that one of the applications of BCC would be for two persons exchanging data by touching. From the application point of view, e.g. healthcare application, a nurse can touch the patient and read all the vital signs or ECG measurements, blood pressure on a mobile device. Thus, further research is needed to investigate the interaction between BCC transceivers on two different bodies.

Regarding the physical layer design, more study needs to be performed on the proposed adaptive code-spreading solution. Some other selection algorithms and codes other than Walsh-Hadamard codes are to be investigated in order to improve the proposed scheme. Also, more tests needs to be done to assess the scheme, e.g. measured interference can be used for the system performance evaluation. Moreover, alternative approaches for physical layer design are to be studied. One of the applicable solutions for BCC is frequency hopping, where the hopping sequence is adjusted based on the experienced interference. It is also beneficial to design a narrow band solution, e.g. based on FSK, to reduce the interference susceptibility. Furthermore, an investigation needs to be performed to come to a low cost and low power solution implementation for the proposed physical layer scheme.

In this work, we proposed a solution for the BCC physical layer based on the BCC channel characteristics. Also, studies need to be performed in order to design the other layers such as MAC layer or network layer with optimized solutions based on the fundamental properties of the BCC channel.

References

[1] T. Schenk, N. S. Mazloum, L. Tan, and P. Rutten, "Experimental characterization of the body-coupled communications channel," in *ISWCS 2008*, October 2008.

[2] T. Falck, H. Balddus, J. Espina, , and K. Klabunde, "Plug'n Play simplicity for wireless medical body sensors," *MONET*, vol. 12, 2007.

[3] T.-Y. Lin and Y.-C. Tseng, "Collision analysis for a multi-bluetooth picocells environment," *IEEE Commun. Lett.*, vol. 7, no. 10, October 2003.

[4] P. Popovski, H. Yomo, and R. Prasad, "Dynamic adaptive frequency hopping for mutually interfereing wireless personal area networks," *IEEE Trans. on Mobile Computing*, vol. 5, no. 8, Auguest 2006.

[5] D. Neirynck, C. Williams, A. Nix, and M. Beach, "Wideband channel characterization for body and personal area networks," *Proc. BSN Workshop*, pp. 41–43, 2004.

[6] Y. Nechayev, P. Hall, C. Constantinou, Y. Hao, A. Alomainy, R. Dubrovka, and C. Parini, "On-body path gain variations with changing body posture and antenna position," *Proc. IEEE AP-S International Symposium*, vol. 1B, pp. 731–734, 2005.

[7] T. Zimmerman, "Personal area networks (PAN): Near-field intra-body communication," Master's thesis, MIT, 1995.

[8] T. Zimmerman, "Personal area networks (PAN): Near-field intra-body communication," *IBM Systems Journal*, vol. 35, no. 3-4, pp. 609–617, April 1996.

[9] K. Partridge, B. Dahlquist, A. Veiseh, A. Cain, A. Foreman, J. Goldberg, and G. Borriello, "Empirical measurements of intrabody communication performance under varied physical configurations," in *Proc. User Interface Softw. Technol. Symp.*, November 2001, pp. 183–190.

[10] K. Fuji, K. Ito, and S. Tajima, "A study on the receiving signal level in relation with the location of electrodes for wearable devices using human body as a transmission channel," in *IEEE Antennas and Propagation Society International Symposium 2003.*, vol. 3, June 2003, pp. 1071–1074.

[11] K. Fuji and K. Ito, "Evaluation of the received signal level in relation to the size and carrier frequencies of the wearable device using human body as a transmission channel," in *IEEE Antennas and Propagation Society International Symposium 2004.*, vol. 1, June 2004, pp. 105–108.

[12] K. Fuji, M. Takahashi, and K. Ito, "Study on the electromagnetic field distributions of realistic japanese adult male and female models with a wearable device using the human body as a transmission channel," in *IEEE Antennas and Propagation Society International Symposium 2006.*, July 2006, pp. 2121–2124.

[13] K. Ito and K. Fuji, "Development and investigation of the transmission mechanism of the wearable devices using the human body as a transmission channel," in *IEEE International Workshop on Antenna Technology Small Antennas and Novel Metamaterials 2006.*, March 2006, pp. 140–143.

[14] A. Nakata, K. Hachisuka, T. Takeda, Y. Terauchi, K. Shiba, K. Sasaki, H. Hosaka, and K. Itao, "Development and performance analysis of an intra-body communication device," in *12th International Conference on TRANSDUCERS, Solid-State Sensors, Actuators and Microsystems 2003.*, vol. 2, June 2003, pp. 1722–1725.

[15] K. Hachisuka, Y. Terauchi, Y. Kishi, T. Hirota, K. Sasaki, H. Hosaka, and K. Itao, "Simplified circuit modeling and fabrication of intrabody communication devices," in *The 13th International Conference on Solid-State Sensors, Actuators and Microsystems 2005.*, vol. 1, June 2005, pp. 461–464.

[16] M. Shinagawa, M. Fukumoto, K. Ochiai, and H. Kyuragi, "A near-field-sensing transceiver for intra-body communication based on the electro-optic effect," in *Proceedings of the 20th IEEE Instrumentation and Measurement Technology Conference 2003.*, vol. 1, May 2003, pp. 296–301.

[17] M. Fukumoto, M. Shinagawa, K. Ochiai, and H. Kyuragi, "A near-field-sensing transceiver for intrabody communication based on the electrooptic effect," in *IEEE Transactions on Instrumentation and Measurement*, vol. 53, December 2004, pp. 1533–1538.

[18] T. Yanagida, "Human body communication syatem and communication device," United States Patent Application Publication, March 2006.

[19] J. Hwang, C. Hyoung, J. Sung, J. Kim, D. Park, and S. Kang, "EM simulation and analysis on the ground electrode of human body communication," in *36th European Microwave Conference 2006.*, September 2006, pp. 1122–1123.

[20] J. Hwang, J. Sung, C. Hyoung, J. Kim, D. Park, and S. Kang, "Analysis of signal interference in human body communication using human body as transmission medium," in *IEEE Antennas and Propagation Society International Symposium 2006.*, July 2006, pp. 495–498.

[21] M. Wegmueller, A. Lehnert, J. F. R. Reutemann, M. Oberle, N. Felber, N. Kuster, O. Hess, and W. Fichtner, "Measurement system for the characterization of the human body as a communication channel at low frequency," in *27th Annual International Conference Engineering in Medicine and Biology Society 2005.*, September 2005, pp. 3502–3505.

[22] M. Wegmueller, A. Kuhn, J. Froehlich, M. Oberle, N. Felber, N. Kuster, and W. Fichtner, "An attempt to model the human body as a communication channel," ETH Zurich, Tech. Rep., 2006.

[23] M. Wegmueller, M. Oberle, N. Felber, N. Kuster, and W. Fichtner, "Galvanical coupling for data transmission through the human body," in *Proceedings of the IEEE Instrumentation and Measurement Technology Conference 2006.*, April 2006, pp. 1686–1689.

[24] J. Ruiz and S. Shimamoto, “Experimental evaluation of body channel response and digital modulation schemes for intra-body communications,” in *IEEE International Conference on Communications 2006.*, vol. 1, June 2006, pp. 349–354.

[25] J. Ruiz and S. Shimamoto, “Novel communication services based on human body and environment interaction: applications inside trains and applications for handicapped people,” in *IEEE Wireless Communications and Networking Conference 2006.*, vol. 4, 2006, pp. 2240–2245.

[26] J. Ruiz, J. Xu, and S. Shimamoto, “Propagation characteristics of intra-body communications for body area networks,” in *Proceedings 3rd IEEE Consumer Communications and Networking Conference*, vol. 1, January 2006, pp. 509–513.

[27] J. Ruiz and S. Shimamoto, “Statistical modeling of intra-body propagation channel,” in *Proceedings IEEE Wireless Communications and Networking Conference*, March 2007, pp. 2063–2068.

[28] S. Choi, S. Song, K. Sohn, H. Kim, J. Kim, N. Cho, J. Woo, J. Yoo, and H. Yoo, “A 24.2 μW dual-mode human body communication controller for body sensor network,” in *Proceedings of the 32nd European Solid-State Circuits Conference 2006.*, September 2006, pp. 227–230.

[29] S. Choi, S. Song, K. Sohn, H. Kim, J. Kim, J. Yoo, and H. Yoo, “A low-power star-topology body area network controller for periodic data monitoring around and inside the human body,” in *10th IEEE International Symposium on Wearable Computers 2006.*, October 2006, pp. 139–140.

[30] S. Song, N. Cho, S. Kim, J. Yoo, and H. Yoo, “A 2 Mb/s wideband pulse transceiver with direct-coupled interface for human body communications,” in *IEEE International Conference Digest of Technical Papers Solid-State Circuits 2006.*, February 2006, pp. 2278–2287.

[31] S. Song, N. Cho, S. Kim, J. Yoo, and H. Yoo, “A 4.8 mW 10 Mb/s wideband signaling receiver analog front-end for human body communications,” in *Proceedings of the 32nd European Solid-State Circuits Conference 2006.*, September 2006, pp. 488–491.

[32] S. Song, N. Cho, S. Lee, and H. Yoo, “Low power wearable audio player using human body communications,” in *10th IEEE International Symposium on Wearable Computers 2006.*, October 2006, pp. 125–126.

[33] S. Song, N. Cho, S. Kim, J. Yoo, S. Choi, and H. Yoo, “A 0.9 V 2.6 mW body-coupled scalable PHY transceiver for body sensor applications,” in *Digest of Technical Papers. IEEE International Solid-State Circuits Conference 2007.*, February 2007, pp. 366–609.

[34] N. Cho, J. Lee, L. Yan, J. bae, S. Kim, and H. Yoo, “A 60 kb/s to 10 Mb/s 0.37 nJ/b adaptive-frequency-hopping transceiver for body-area network,” in *IEEE International Solid-State Circuits Conference 2007.*, February 2008, pp. 132–602.

[35] N. Cho, J. Yoo, S.-J. Song, J. Lee, S. Jeon, and H.-J. Yoo, “The human body characteristics as a signal transmission medium for intrabody communication,” *IEEE Transactions on Microwave Theory and Techniques.*, vol. 55, pp. 1080–1086, May 2007.

[36] “RS FSH4/8 Handheld Spectrum Analyzer, http://www2.rohde-schwarz.com/en/products/test_and_measurement/product_categories/spectrum_analysis/FSH3_6_18.html.”

[37] “United States Frequency Allocation Chart, http://www.ntia.doc.gov/osmhome/ allochrt.pdf.”

[38] S. Gabriel, R. W. Lau, and C. Gabriel, “The dielectric properties of biological tissues: Ii. measurements in the frequency range 10 Hz to 20 GHz,” *Phys. Med. Biol.*, vol. 41, 1996.

[39] “Fitting a univariate distribution using cumulative probabilities, http://www.mathworks.com/products/statistics/demos.html?file=products/demos/shipping/stats/cdffitdemo.html.”

[40] S. M. Kay, *Fundamentals of statistical processing: estimation theory*. Prentice Hall, 1993.

[41] S. Haykin and M. Moher, *Modern Wireless Communication*. PEARSON, Prentice Hall, 2003.

Acknowledgments

This Master thesis project would not have been possible without the support of many people.

I would like to acknowledge Dr. Ir. Tim Schenk, for giving me the opportunity to perform my research at Philips Research, for his inspiration and helpful discussions. Furthermore, I am grateful to the people of the ADA group, Alberto Fazzi, Steven Correy, Karin Klabunde, Heribert Baldus, for their help. I am also grateful to Peter Rutten and Luc Tan and the people of the EMC room for their contribution to my project and to Brenda Domingo and Lieneke Berning for taking care of the administrative part.

I would like to specially thank prof. Eric Ström for the guidance during my graduate career and the completion of this thesis. Also, I would like to thank Mats Rydström for his input in this project.

Thanks to my friends in Göteborg and Eindhoven, for making the years of my study such a pleasant and dynamic period of my life. Last but not least, thanks to my family for their unconditional support during all these years.

Nafiseh Seyed Mazloum,
Göteborg, December 2008

Appendix A

Coupler Locations and Test Methods Tables

As discussed in Chapter 4, different parameters need to be studied in order to characterize the BCC channel experimentally. One of the parameter is the distance between the TX and RX on the body considering different usage scenarios. To examine the influence of the couplers locations on the on-body channel behavior, different TX and RX location combinations have been considered. Table A.1 lists the possible combinations of the TX and RX on the body. Table A.2 indicates the combination of the test parameters that have been applied in this work.

Table A.1: Combinations of the TX and RX coupler location on the body.

TX Coupler Locations	RX Coupler Locations
A1	A2 A3 A4 A5 A6 A7 A8 A9 H C1 P L5 W
A2	A3 A4 A5 A6 A7 A8 A9 H C1 P L5 W
A3	A4 A5 A6 A7 A8 A9 H C1 P L5 W
A4	A5 A6 A7 A8 A9 H C1 P L5 W
A5	A6 A7 A8 A9 H C1 P L5 W
C1	H A1 A2 A4
C2	A1 A2 A4 C1 L5 P C3 W
C3	H A1 A2 A4 C1 L5 P W
C4	A1 A2 A4 C1 C3 L5 P W
W1	A1 A2 A4 C1 C3 L5 P W
W2	A1 A2 A4 C1 C3 L5 P W
W3	A1 A2 A4 C1 C3 L5 P W
W4	A1 A2 A4 C1 C3 L5 P W
L1	H L2 L3 L4 L5 A1 A2 A4
L2	H L3 L4 L5 A1 A2 A4
L3	L4 L5 A1 A2 A4
L4	L5 A1 A2 A4
L5	H A1 A2 A4

Table A.2: Overview combinations of test parameters.

TX Location	**A1**	**A2**		**A2**		**C3**		**L2**	
RX Location	**A9**	**A3**		**A4**		**L2**		**A2**	
Coupler size Vertical Orientation	TX: 2×2 cm^2 RX: 2×2 cm^2 Sep.: 2 cm	TX: 2×2 cm^2 RX: 2×2 cm^2 Sep.: 2 cm		TX: 2×2 cm^2 RX: 2×2 cm^2 Sep.: 2 cm		TX: 2×2 cm^2 RX: 2×2 cm^2 Sep.: 2 cm		TX: 2×2 cm^2 RX: 2×2 cm^2 Sep.: 2 cm	
		TX: 3×3 cm^2 RX: 3×3 cm^2 Sep.: 2 cm		TX: 3×3 cm^2 RX: 3×3 cm^2 Sep.: 2 cm		TX: 3×3 cm^2 RX: 3×3 cm^2 Sep.: 2 cm		TX: 3×3 cm^2 RX: 3×3 cm^2 Sep.: 2 cm	
		TX: 4×4 cm^2 RX: 4×4 cm^2	Sep.: 0.2 cm Sep.: 0.5 cm Sep.: 1 cm Sep.: 2 cm	TX: 4×4 cm^2 RX: 4×4 cm^2	Sep.: 0.2 cm Sep.: 0.5 cm Sep.: 1 cm Sep.: 2 cm	TX: 4×4 cm^2 RX: 4×4 cm^2	Sep.: 0.2 cm Sep.: 0.5 cm Sep.: 1 cm Sep.: 2 cm	TX: 4×4 cm^2 RX: 4×4 cm^2	Sep.: 0.2 cm Sep.: 0.5 cm Sep.: 1cm Sep.: 2 cm
		TX: 3.5×5.5 cm^2 RX: 3.5×5.5 cm^2 Sep.: 2 cm		TX: 3.5×5.5 cm^2 RX: 3.5×5.5 cm^2 Sep.: 2 cm		TX: 3.5×5.5 cm^2 RX: 3.5×5.5 cm^2 Sep.: 2 cm		TX: 3.5×5.5 cm^2 RX: 3.5×5.5 cm^2 Sep.: 2 cm	
Coupler Size Horizontal Orientation	TX: 2×2 cm^2 RX: 2×2 cm^2 Sep.: 1 cm	TX: 2×2 cm^2 RX: 2×2 cm^2	Sep.: 1 cm Sep.: 2 cm Sep.: 4 cm	TX: 2×2 cm^2 RX: 2×2 cm^2	Sep.: 1 cm Sep.: 2 cm Sep.: 4 cm	TX: 2×2 cm^2 RX: 2×2 cm^2	Sep.: 1 cm Sep.: 2 cm Sep.: 4 cm	TX: 2×2 cm^2 RX: 2×2 cm^2	Sep.: 1 cm Sep.: 2 cm Sep.: 4 cm
		TX: 3×3 cm^2 RX: 3×3 cm^2	Sep.: 1 cm Sep.: 3 cm	TX: 3×3 cm^2 RX: 3×3 cm^2	Sep.: 1 cm Sep.: 3 cm	TX: 3×3 cm^2 RX: 3×3 cm^2	Sep.: 1 cm Sep.: 3 cm	TX: 3×3 cm^2 RX: 3×3 cm^2	Sep.: 1 cm Sep.: 3cm
Dynamic	Moving arm	Moving arm		Moving arm		Moving arm		Moving arm	
		Walking		Walking		Walking		Walking	
Static	Sitting	Sitting		Sitting		Sitting		Sitting	
	Standing	Standing		Standing		Standing		Standing	
Skin Contact	Direct Contact	Direct Contact		Direct Contact		Direct Contact		Direct Contact	
		Clothes in Between		Clothes in Between		Clothes in Between		Clothes in Between	
Environment	Lab	Lab		Lab		Lab		Lab	
	Conference Room	Conference Room		Conference Room		Conference Room		Conference Room	
	EMC Room	EMC Room		EMC Room		EMC Room		EMC Room	
	Outdoor	Outdoor		Outdoor		Outdoor		Outdoor	

Appendix B

Measurement Results

This appendix reports additional results from the experimental study of the BCC channel characteristics. First the results of the measurement that have been performed in the conference room are depicted. Next, the results for the EMC room are shown. Finally, the results of interference experiments are depicted.

B.1 Conference room results

This section shows the results of the measured data for the different coupler locations, coupler dimension, coupler spacing and body movements in the conference room. Figures B.1 and B.2 show the coupler size influence on the propagation loss. Figure B.3 show different coupler locations results for four couplers sizes. Finally, Figures B.4, B.6 and B.8 show the influence of the body movements on propagation loss.

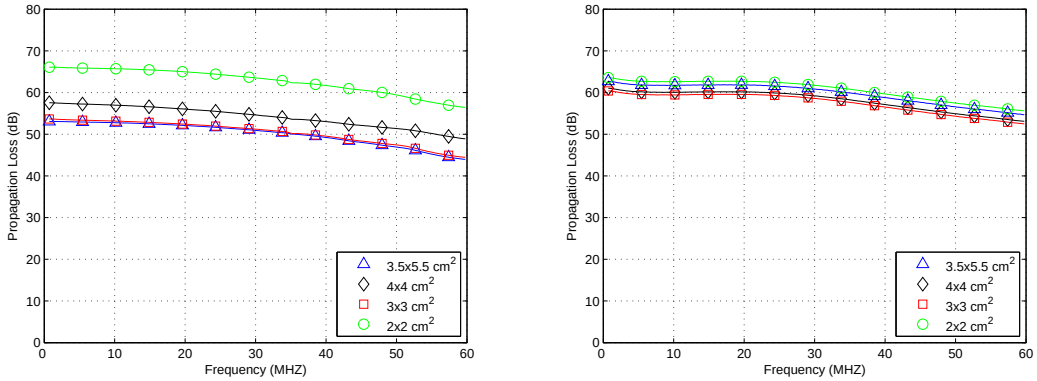

(a) arm channel (A2A4). (b) leg-arm channel (L2A2).

Fig. B.1: Influence of electrode dimension on the propagation loss as function of frequency, for 2 cm electrode pair spacing.

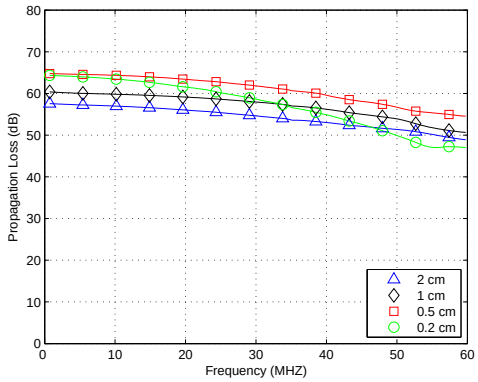

(a) arm channel (A2A4).

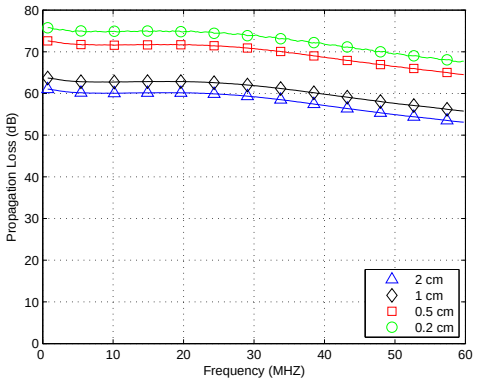

(b) leg-arm channel (L2A2).

Fig. B.2: Influence of electrode pair spacing on the propagation loss as function of frequency, for $4 \times 4\ \mathrm{cm}^2$ electrode dimension.

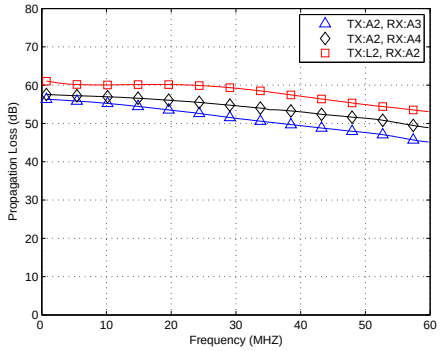

(a) $4 \times 4\ \mathrm{cm}^2$ and 2 cm electrode pair spacing.

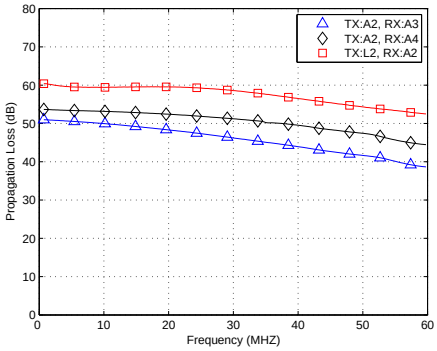

(b) $3 \times 3\ \mathrm{cm}^2$ and 2 cm electrode pair spacing.

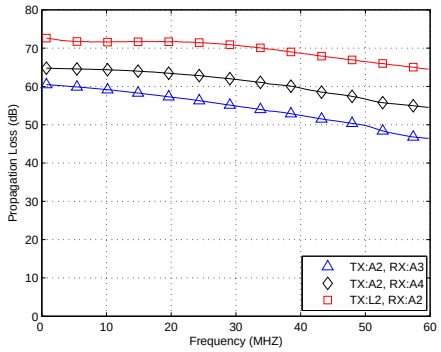

(c) $4 \times 4\ \mathrm{cm}^4$ and 0.5 cm electrode pair spacing.

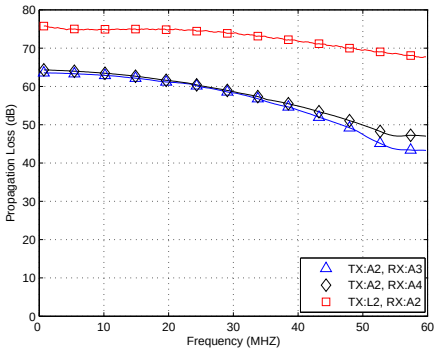

(d) $4 \times 4\ \mathrm{cm}^2$ and 0.2 cm electrode pair spacing.

Fig. B.3: Influence of transceiver locations on the propagation loss as function of frequency.

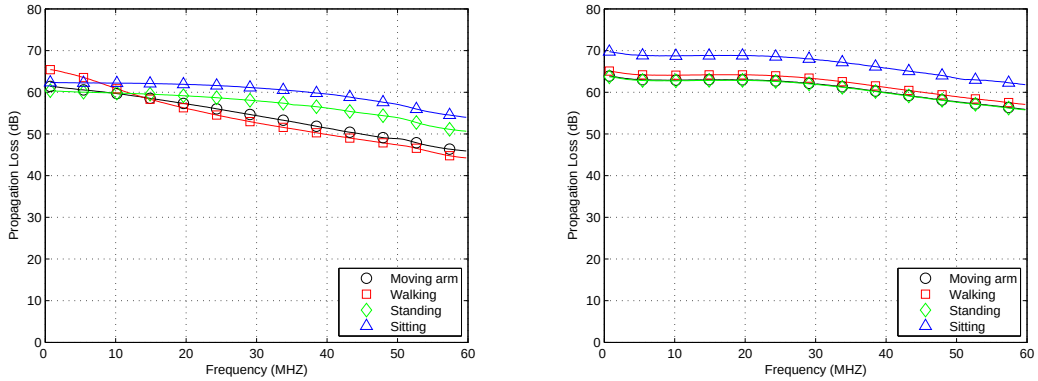

(a) arm channel (A2A4). (b) leg-arm channel (L2A2).

Fig. B.4: Influence of body movements on the propagation loss as function of frequency, for sitting on a chair, standing, walking, moving arm, for 4×4 cm^2 electrode dimension and 2 cm electrode pair spacing.

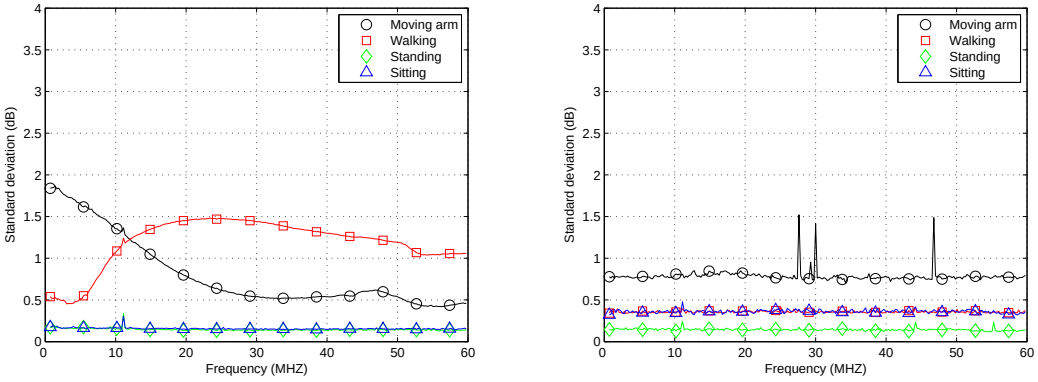

(a) arm channel (A2A4). (b) leg-arm channel (L2A2).

Fig. B.5: Influence of body movements on the standard deviation as function of frequency, for sitting on a chair, standing, walking, moving arm, for 4×4 cm^2 electrode dimension and 2 cm electrode pair spacing.

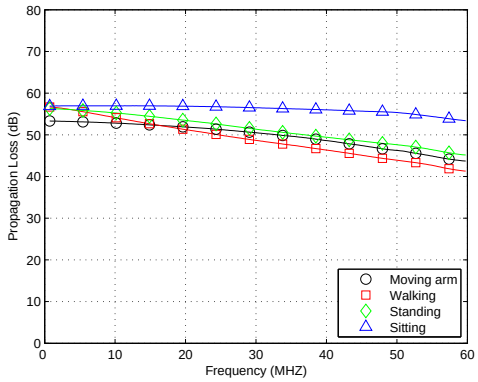

(a) 2 cm electrode pair spacing.

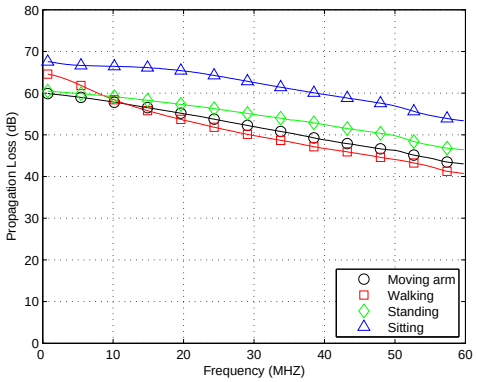

(b) 0.5 cm electrode pair spacing.

Fig. B.6: Influence of body movements on the propagation loss as function of frequency, for sitting on a chair, standing, walking, moving arm, for arm channel (A2A3) and 4×4 cm^2 electrode dimension.

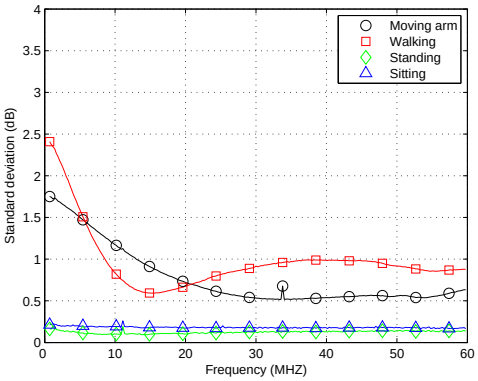

(a) 2 cm electrode pair spacing.

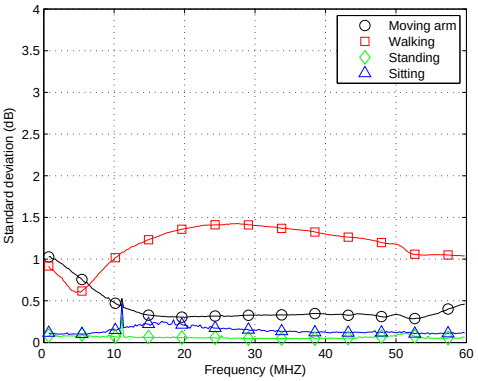

(b) 0.5 cm electrode pair spacing.

Fig. B.7: Influence of body movements on the standard deviation as function of frequency, for sitting on a chair, standing, walking, moving arm, for arm channel (A2A3) and 4×4 cm^2 electrode dimension.

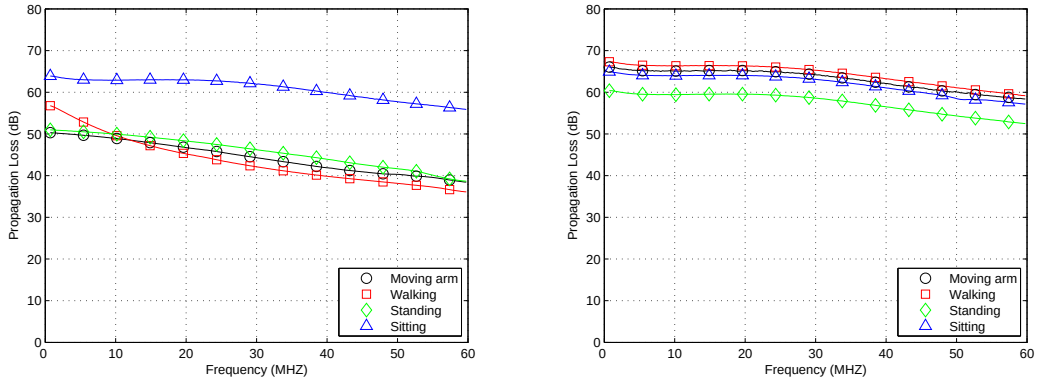

(a) arm channel (A2A3). (b) leg-arm channel (L2A2).

Fig. B.8: Influence of body movements on the propagation loss as function of frequency, for sitting on a chair, standing, walking, moving arm, for 3×3 cm^2 electrode dimension and 2 cm electrode pair spacing.

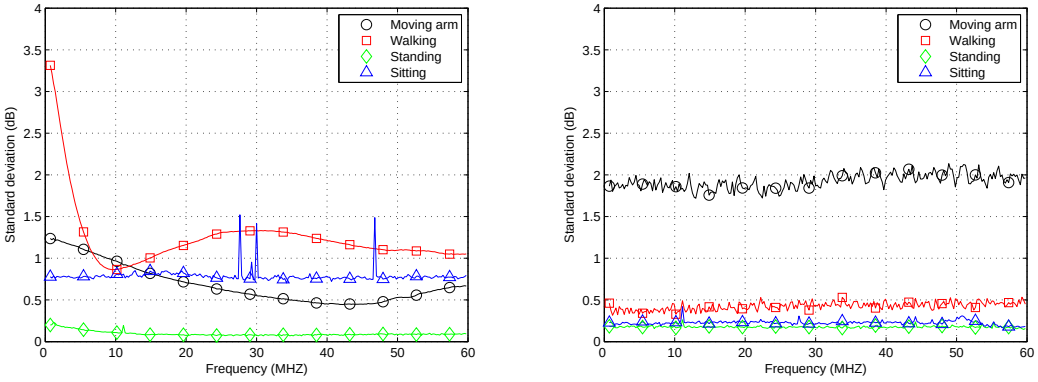

(a) arm channel (A2A3). (b) leg-arm channel (L2A2).

Fig. B.9: Influence of body movements on the standard deviation as function of frequency, for sitting on a chair, standing, walking, moving arm, for 3×3 cm^2 electrode dimension and 2 cm electrode pair spacing.

B.2 EMC room results

This section shows the results of the measured data for the different coupler locations, coupler dimension, coupler spacing that have been carried out in the EMC room.

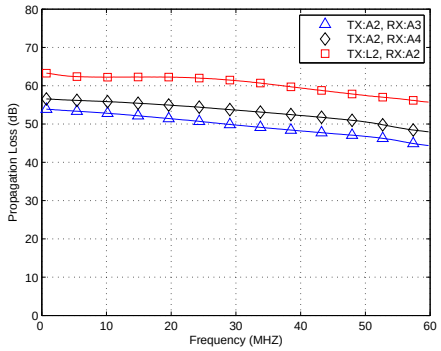

(a) $4 \times 4\ \mathrm{cm}^2$ and 2 cm electrode pair spacing.

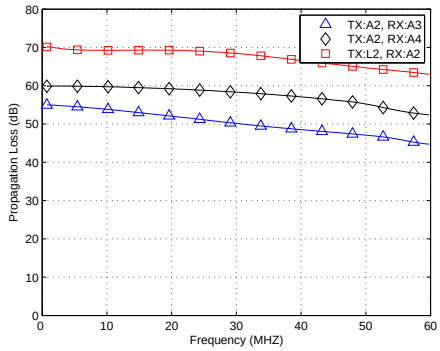

(b) $3 \times 3\ \mathrm{cm}^2$ and 2 cm electrode pair spacing.

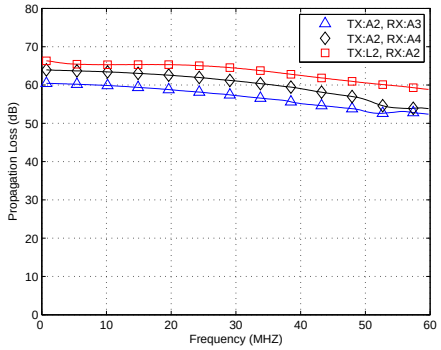

(c) $4 \times 4\ \mathrm{cm}^4$ and 0.5 cm electrode pair spacing.

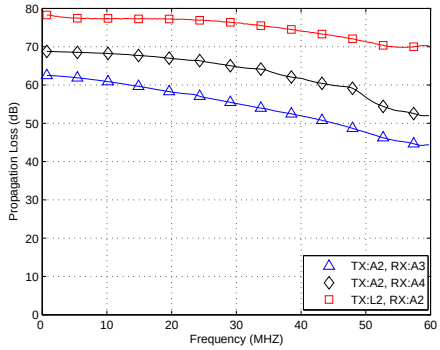

(d) $4 \times 4\ \mathrm{cm}^2$ and 0.2 cm electrode pair spacing.

Fig. B.10: Influence of transceiver locations on the propagation loss as function of frequency.

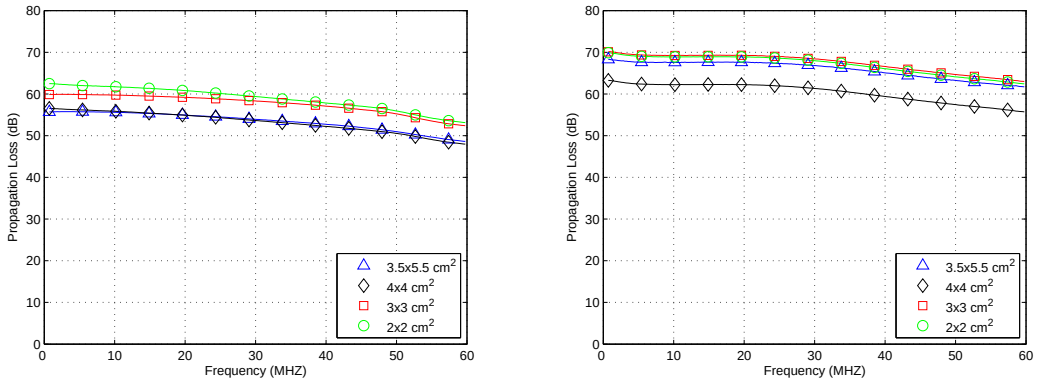

(a) arm channel (A2A4) and 2 cm electrode pair spacing. (b) leg-arm channel (L2A2) and 2 cm electrode pair spacing.

Fig. B.11: Influence of electrode dimension on the propagation loss as function of frequency.

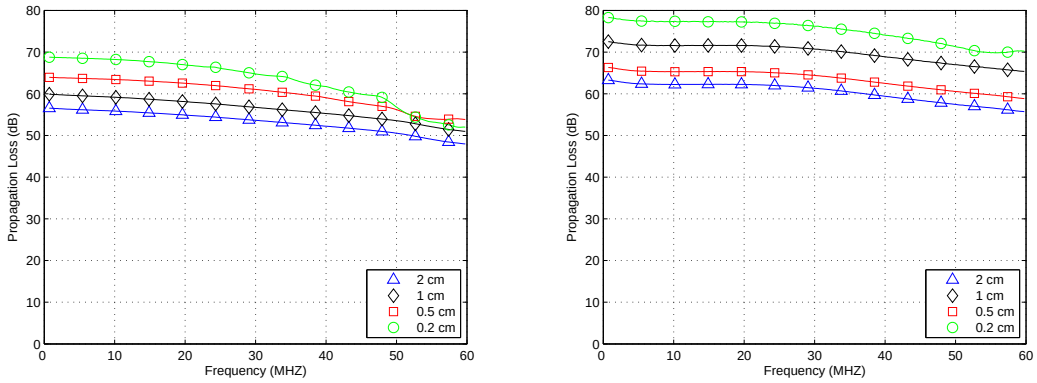

(a) arm channel (A2A4) and $4 \times 4\ \mathrm{cm}^2$ electrode dimension. (b) leg-arm channel (L2A2) and $4 \times 4\ \mathrm{cm}^2$ electrode dimension.

Fig. B.12: Influence of electrode pair spacing on the propagation loss as function of frequency.

B.3 Interference results

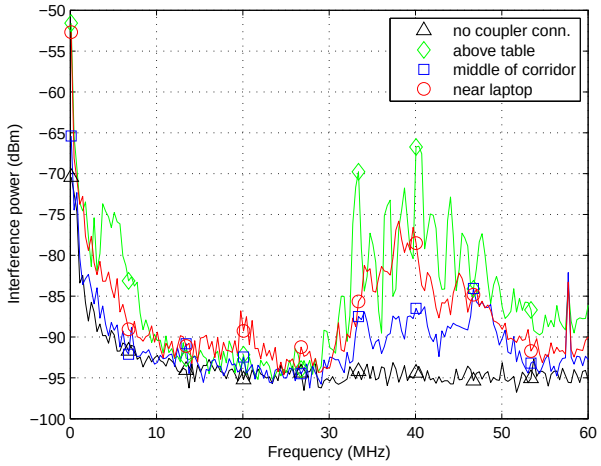

Fig. B.13: Measured interference power for different measurements locations in the corridor.

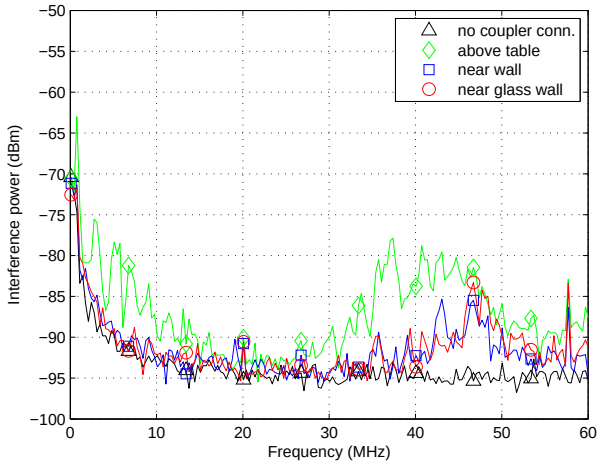

Fig. B.14: Measured interference power for different measurements locations in the conference room.

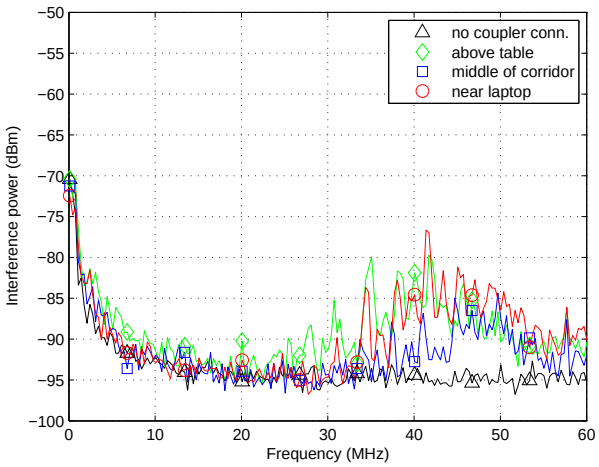

Fig. B.15: Measured interference power for different measurements locations in the conference room another subject.

Appendix C

Results of channel modeling

This section shows additional results of the modeling of the BCC channel due to the body movement, i.e walking and moving arm. In Chapter 5 the ECDF of the amplitude variation was compared to the best fit theoretical distributions for 40-45 MHz sub-band and the arm channel (A2A3). Figures C.1 and C.2 depict the ECDF of the measured data and the best fit theoretical distributions for the moving arm and walking, respectively. These results are for the subbands 5-10 MHz and 35-40 MHz and for the arm channel (A2A3). Figures C.3 and C.4 show the ECDF of the measured data and the best fit theoretical distributions for the arm channel and leg-arm channel, respectively. These results are for the subbands 40-45 MHz.

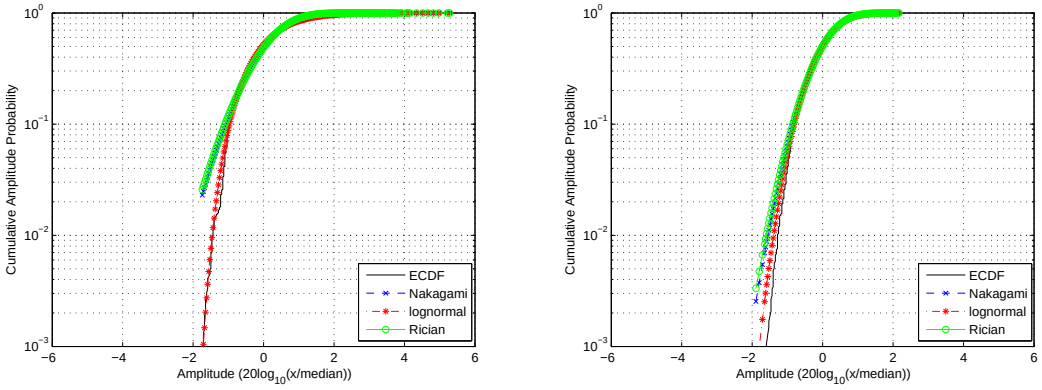

(a) for frequency band of 5-10 MHz.

(b) for frequency band of 35-40 MHz.

Fig. C.1: ECDF (logarithmic scale) of the deviation in amplitude of propagation loss (in dB) due to body movement together with the CDFs of the best fit theoretical distributions, for moving arm scenario and arm channel (A2A3).

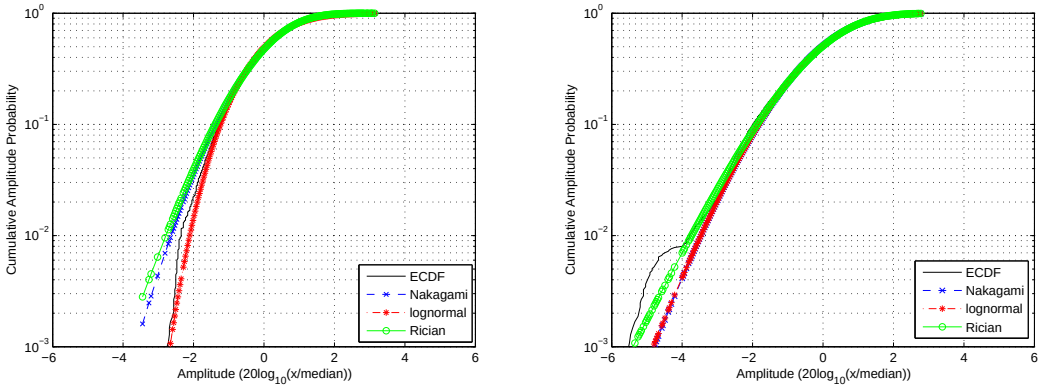

(a) for frequency band of 5-10 MHz. (b) for frequency band of 35-40 MHz.

Fig. C.2: ECDF (logarithmic scale) of the deviation in amplitude of propagation loss (in dB) due to body movement together with the CDFs of the best fit theoretical distributions, for walking scenario and arm channel (A2A3).

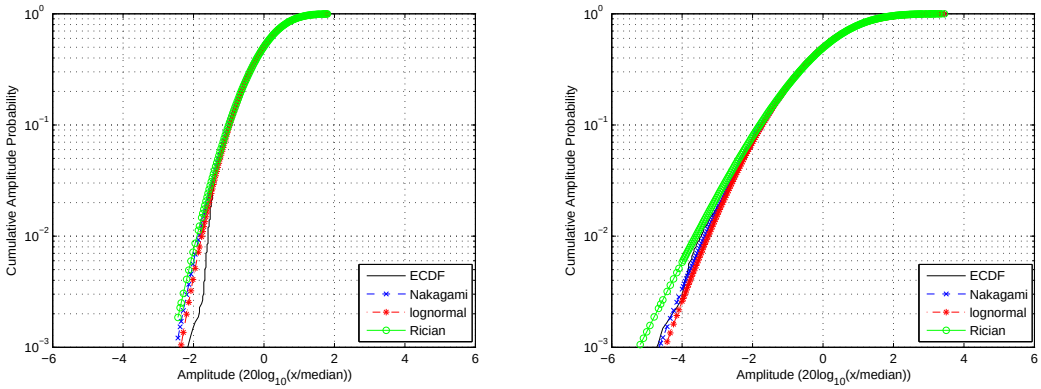

(a) for moving arm scenario. (b) for walking scenario.

Fig. C.3: ECDF (logarithmic scale) of the deviation in amplitude of propagation loss (in dB) due to body movement together with the CDFs of the best fit theoretical distributions, for frequency band of 40-45 MHz and arm channel (A2A4).

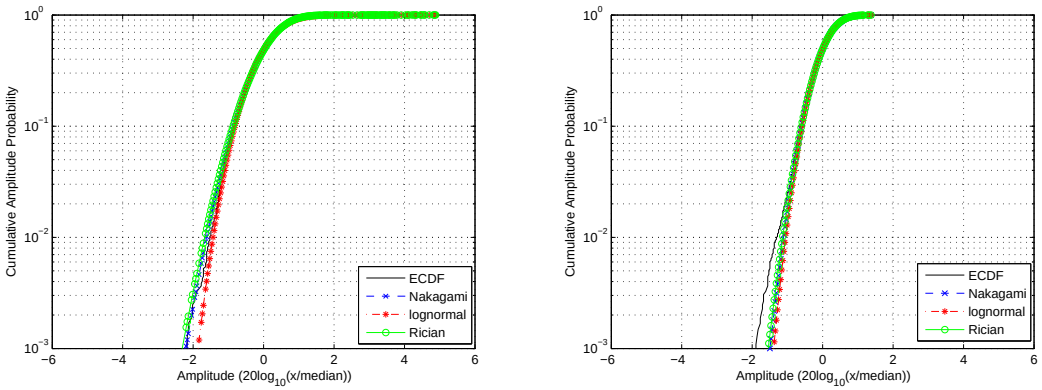

(a) for moving arm scenario.

(b) for walking scenario.

Fig. C.4: ECDF (logarithmic scale) of the deviation in amplitude of propagation loss (in dB) due to body movement together with the CDFs of the best fit theoretical distributions, for frequency band of 40-45 MHz and leg-arm channel (L2A2).

Appendix D

Numerical results of physical layer

This appendix presents more numerical results for the adaptive-code spreading scheme. Figs. D.1, D.2 and D.3 depict the performance of the BCC system for all the Walsh-Hadamard sequences and a random code for interference model II, III and IV, respectively. Figs. D.4, D.5, D.6 and D.7 show the performance of the code selection algorithm for different time sensing period for interference model II, III, IV and V, respectively. Finally, the histograms of the selected best code for different periods of interference study are shown for interference model II, III, IV and V in Figs. D.8, D.9, D.10 and D.11 , respectively.

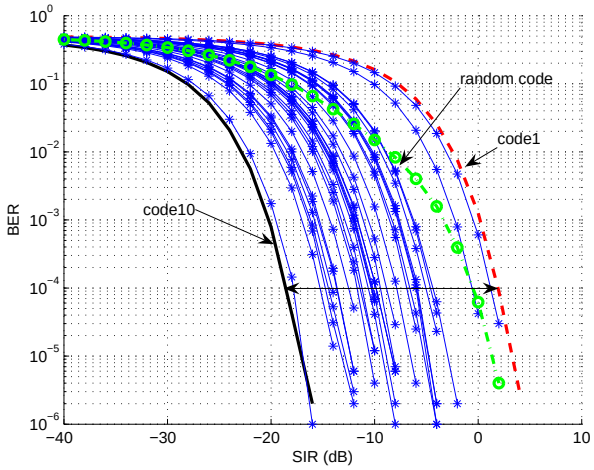

Fig. D.1: BER performance for code spreading for all codes in the WH codebook of length 32 and a random spreading code, for interference model II.

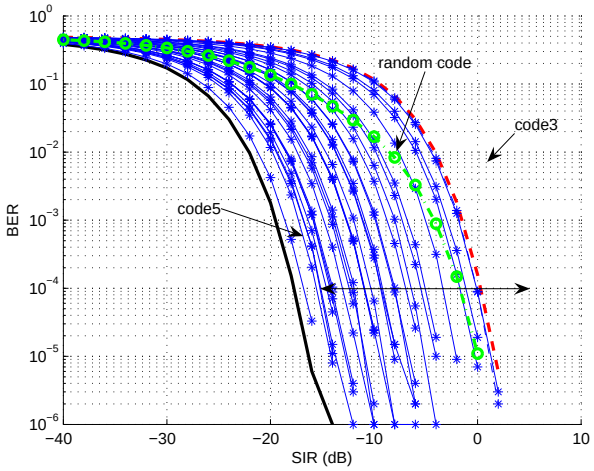

Fig. D.2: BER performance for code spreading for all codes in the WH codebook of length 32 and a random spreading code, for interference model III.

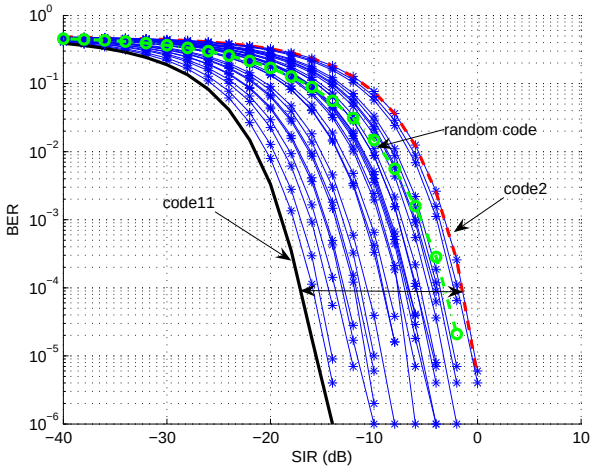

Fig. D.3: BER performance for code spreading for all codes in the WH codebook of length 32 and a random spreading code, for interference model IV.

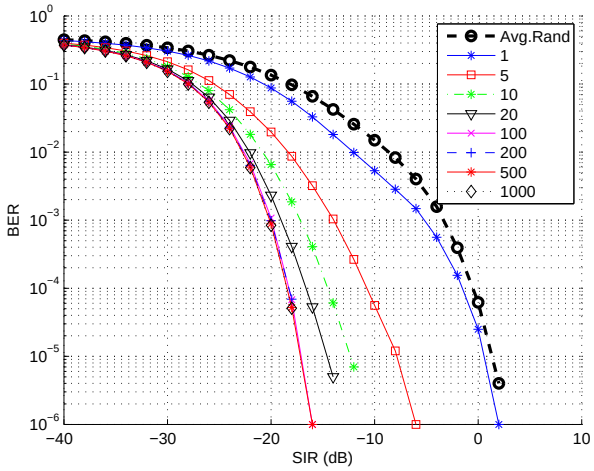

Fig. D.4: BER performance in code selection algorithm for different code selection time together with BER performance of code spreading for random code in WH, for interference model II.

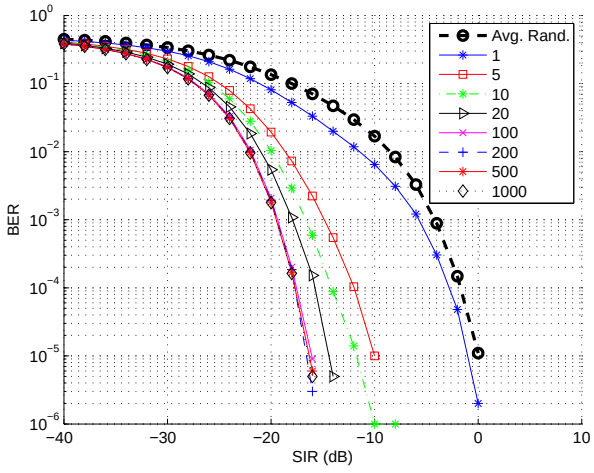

Fig. D.5: BER performance in code selection algorithm for different code selection time together with BER performance of code spreading for random code in WH, for interference model III.

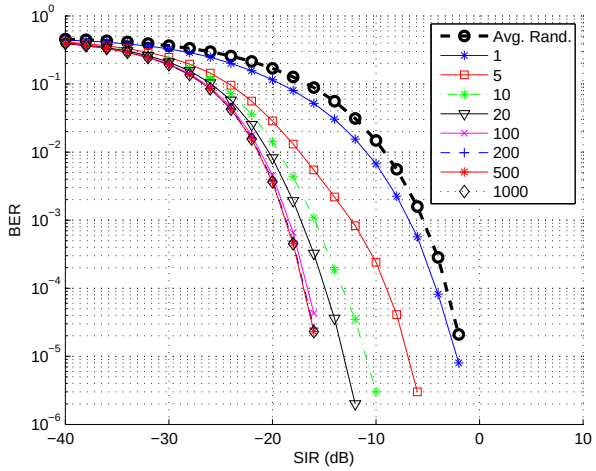

Fig. D.6: BER performance in code selection algorithm for different code selection time together with BER performance of code spreading for random code in WH, for interference model IV.

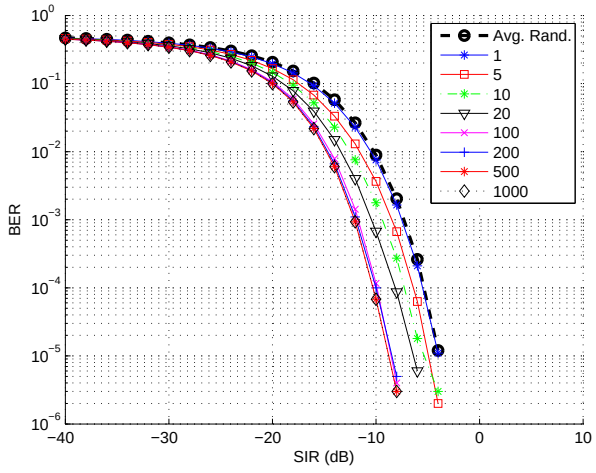

Fig. D.7: BER performance in code selection algorithm for different code selection time together with BER performance of code spreading for random code in WH, for interference model V.

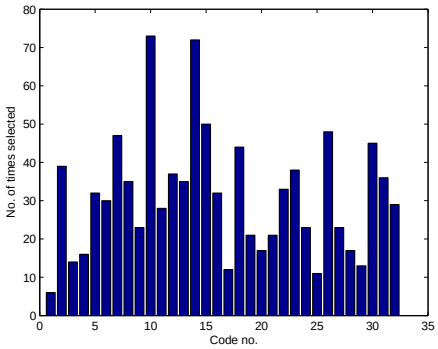

(a) Histogram of the best code of 1 selection time.

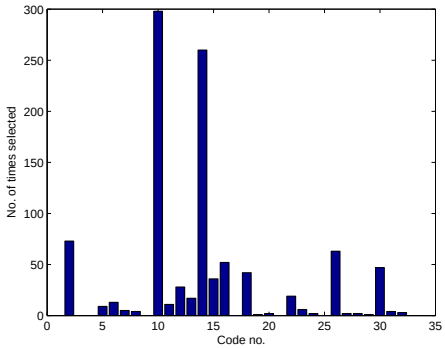

(b) Histogram of the best code of 5 selection time.

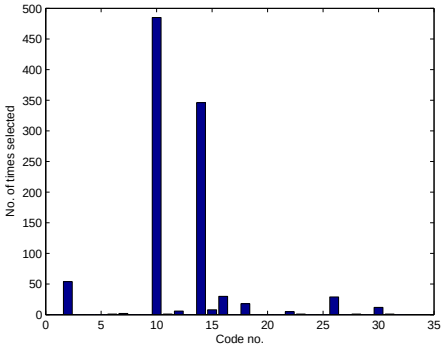

(c) Histogram of the best code of 10 selection time.

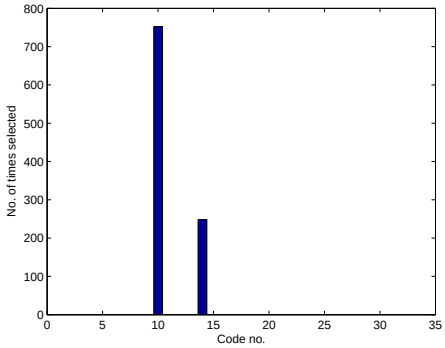

(d) Histogram of the best code of 100 selection time.

Fig. D.8: Histograms of the selected best code for different period of interference study, for interference model II.

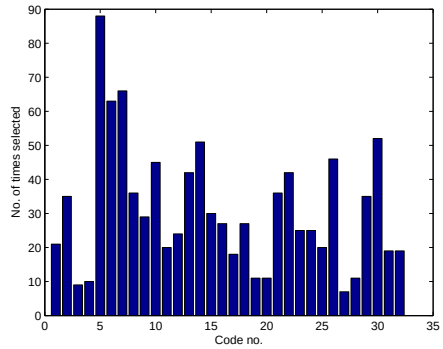

(a) Histogram of the best code of 1 selection time.

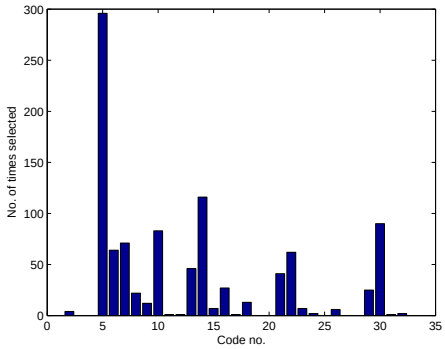

(b) Histogram of the best code of 5 selection time.

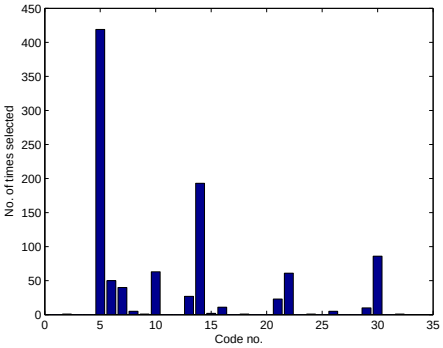

(c) Histogram of the best code of 10 selection time.

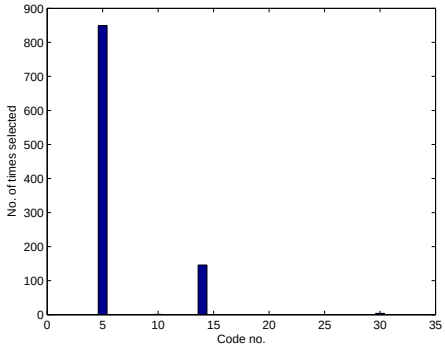

(d) Histogram of the best code of 100 selection time.

Fig. D.9: Histograms of the selected best code for different period of interference study, for interference model III.

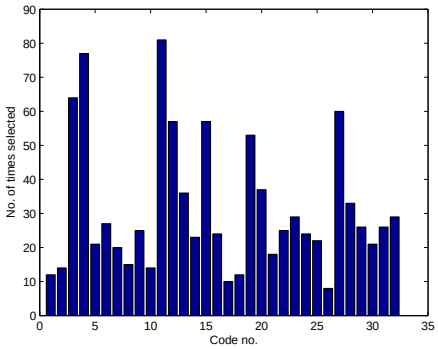

(a) Histogram of the best code of 1 selection time.

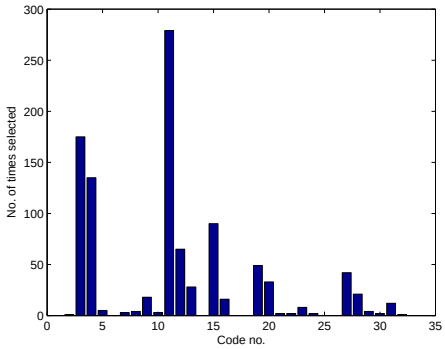

(b) Histogram of the best code of 5 selection time.

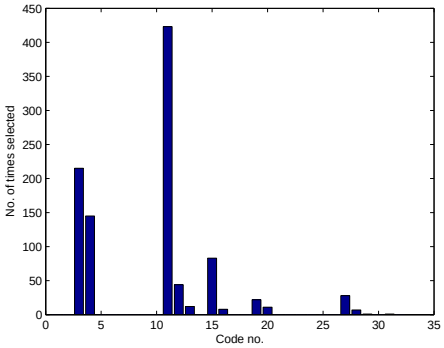

(c) Histogram of the best code of 10 selection time.

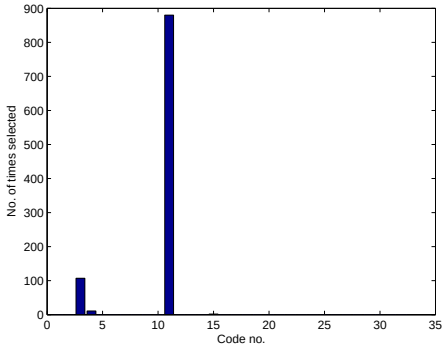

(d) Histogram of the best code of 100 selection time.

Fig. D.10: Histograms of the selected best code for different period of interference study, for interference model IV.

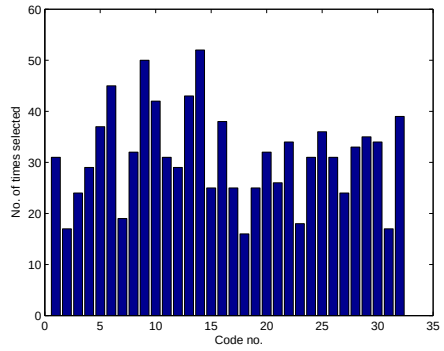

(a) Histogram of the best code of 1 selection time.

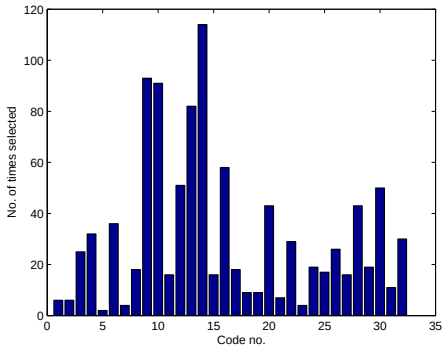

(b) Histogram of the best code of 5 selection time.

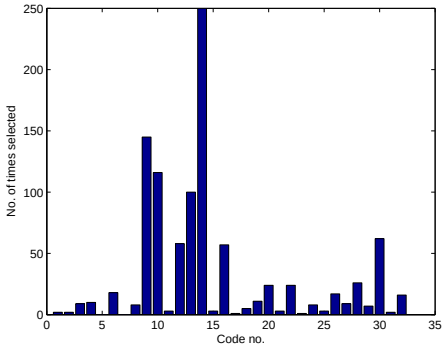

(c) Histogram of the best code of 10 selection time.

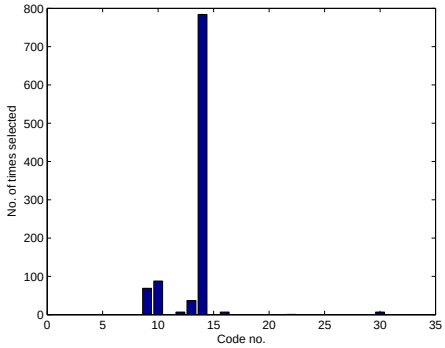

(d) Histogram of the best code of 100 selection time.

Fig. D.11: Histograms of the selected best code for different period of interference study, for interference model V.